Propagation and Scattering of Elastic Waves in Laminated Circular Cylinders

by

Nipon Rattanawangcharoen

A Thesis

Submitted to the Faculty of Graduate Studies

in Partial Fulfillment of the Requirements

of the Degree of

Doctor of Philosophy

Department of Civil Engineering

University of Manitoba

Winnipeg, Manitoba, Canada

ISBN 0-315-85957-1

PROPAGATION AND SCATTERING OF ELASTIC WAVES IN LAMINATED CIRCULAR CYLINDERS

BY

NIPON RATTANAWANGCHAROEN

A Thesis submitted to the Faculty of Graduate Studies of the University of Manitoba in partial fulfillment of the requirements for the degree of

DOCTOR OF PHILOSOPHY

Abstract

Propagation and scattering of guided elastic waves in circular cylinders are investigated. An analytical method is formulated to study wave propagation in laminated isotropic cylinders while Rayleigh-Ritz type approximations are developed for laminated composite cylinders where the analytical solutions are unattainable. The effects of circumferential wavenumber, thickness to radius ratio, ply lay-up configuration, and layering on dispersion characteristics of free guided waves are investigated through these techniques.

The problem of reflection of waves normally incident upon the free end of cylinders is studied as a special case of wave scattering problems. A wave functions expansion procedure is employed in developing least square and variational methods for the investigation. Numerical results demonstrate the successful application of the Rayleigh-Ritz type approximation and the variational technique for the free end reflection problem in laminated composite cylinders.

A hybrid method is presented to analyse the scattering of plane strain waves by load or flaw in cylindrical cross-section. The domain of the cross-section is divided into two regions, an interior region and an exterior region. The interior region which contains the load or flaw is modelled by finite elements while a wave functions expansion is employed for the exterior region. The numerical results for the scattered amplitudes from the load and from flaw are presented for Zr-Nb pressure tube.

Acknowledgements

The author's appreciation of solid mechanics and wave propagation was enhanced through years of association with Professors A.H. Shah, P. Karasudhi, and C. Kasemset. The author would like to express his heartfelt gratitude to them especially to his advisor, Professor A.H. Shah, for his supervision and suggestion during the course of this research. A couple of sentences cannot adequately express the measure of gratitude which is due to his encouragement and support throughout this work.

The author would also like to express his grateful thanks to Professors R.K.N.D. Rajapakse, R. Han, and A.C. Trupp for serving in the examination committee.

The author deeply appreciates the support and encouragement of his friends, Dr. W.M. Karunasena, Dr. Y. Wang, Dr. Y.M. Desai, Dr. R. Paskaramoorthy, Mr. J. Wright, Mr. J. West, Mr. M. Sujumnong, Mr. T. Senjuntichai, and Mr. J. Zhu, during graduate work at the University of Manitoba. Valuable informations and suggestions from Mr. S. Rajpal, Boeing Canada, and Dr. H.D. Mair, Ontario Hydro, are appreciated. Grateful acknowledgements are also due to the staff of the Computer Services of the University of Manitoba, Mr. D. Wyatt, Mr. D. Milton, and Mr. N. Donaldson, for their help in solving computer related problems.

Financial supports in the form of research assistantship from the NSERC, the Office

of Naval Research, and the Ontario Hydro research grant of Professor A.H. Shah and a teaching assistantship from the Department of Civil Engineering, the ENGAP enabled the author to complete this doctoral study. They are kindly acknowledged.

Finally, the author wishes to dedicate this dissertation to his beloved parents, brother and sisters, his relatives, the Grover family, the Callander family and Mr. J. Dickinson whose unfailing love and inspiring encouragement helped him to achieve his success.

Nipon Rattanawangcharoen

Winnipeg, Canada

August 27, 1993

Table of Contents

List of Figures

List of Tables

Chapter 1

Introduction

1.1 Introduction to Composite Materials

Demand on materials imposed by today's advanced technologies have become so diverse and severe that they often cannot be met by simple single-component materials acting alone. It is frequently necessary to combine several materials into a composite to which each constituent not only contributes its share, but also the combination provides new performances unacheivable by the individual constituents. Commonly, composite materials are categorized into three types (Jones 1975):

- Fibrous composites
- Particulate composites
- Laminated composites.

1.1.1 Fibrous Composites

Fibrous composites are composed of fibres in a matrix. The fibres are characterized geometrically by their near crystal-sized diameter. Naturally, fibres are of little use unless they are bound together. The binder material is usually called a matrix. Typically, the matrix has considerably lower density, stiffness and strength than the fibres. However, the combination of fibres and a matrix can provide very high stiffness and strength, yet low density. Some examples of a few selected fibre materials are shown in Table 1.1.

Fibre or wire	Density (kg/m^3)	Tensile strength (GN/m^2)	Tensile stiffness (GN/m^2)
Aluminum	26.3	.62	73
Titanium	46.1	1.9	115
Steel	76.6	4.1	207
E-glass	25.0	3.4	72
S-glass	24.4	4.8	86
Carbon	13.8	1.7	190
Beryllium	18.2	1.7	300
Boron	25.5	3.4	400
Graphite	13.8	1.7	250

Table 1.1: Examples of fibre materials (source : adapted from Dietz 1965)

1.1.2 Particulated Composites

Particulated composites consist of particles of one or more materials suspended in a matrix. Both the particles and the matrices can either be metallic or nonmetallic. Exam-

ples of these composites are concrete (nonmetallic in nonmetallic composites), aluminum paint (metallic in nonmetallic composites), Tungsten carbide (nonmetallic in metallic composites), etc.

1.1.3 Laminated Composites

Laminated composites are composed of layers or laminae of two or more materials bonded together. The properties that can be emphasized by lamination are strength, stiffness, low weight, corrosion resistance, attractiveness, thermal insulation, acoustical insulation, etc. Examples of laminated composites are bimetals, clad metals, laminated glass, plastic based laminates and laminated fibrous composites or laminated fibre-reinforced composites.

The classification scheme can be arbitrary and imperfect. Nevertheless, this introductory remark serves only to acquaint the reader with the broad possibilities of composite materials. It should be noted that numerous multiphase composites exhibit more than one characteristic class. For instance, laminated fibre-reinforced composites are laminated and fibrous composites. In this study, the emphasis will be placed mostly on laminated and fibrous composites.

1.2 Fibrous and Laminated Composites

Basic terminologies of fibrous and laminated composites in the remainder of this thesis will be introduced in this section.

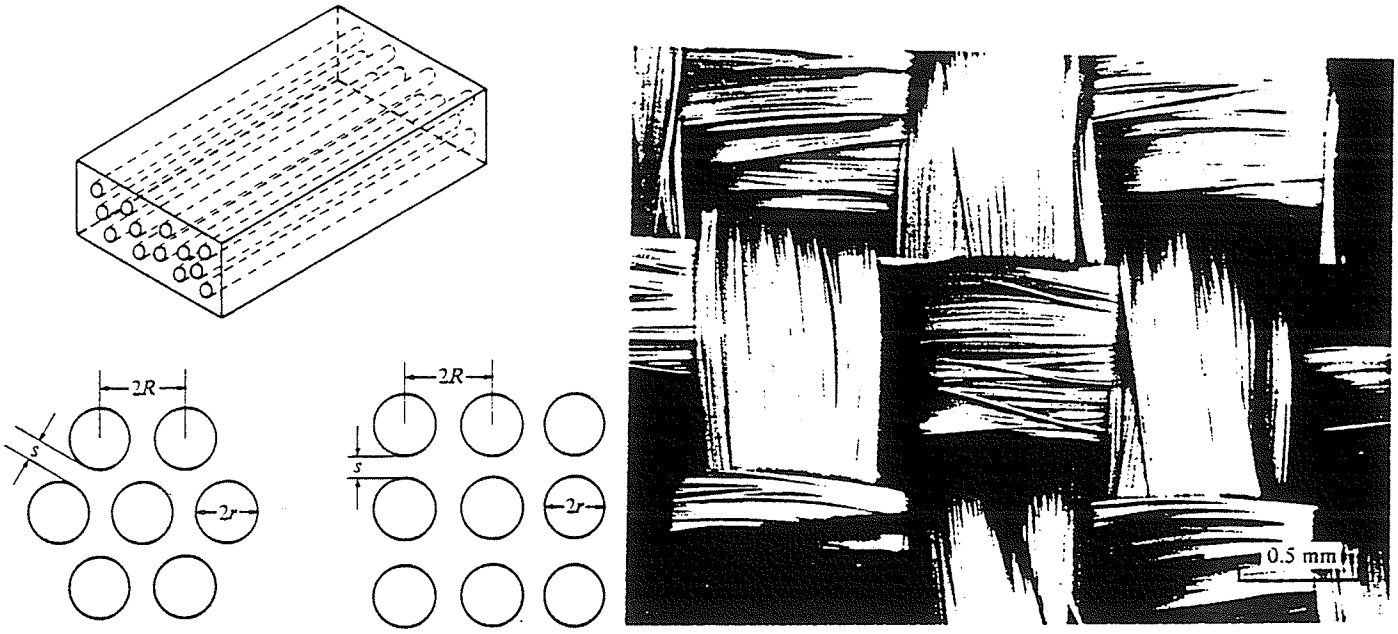

Lamina with unidirectional fibres

Lamina with woven fibres

Figure 1.1: Two principal types of laminae (source : Hull, D. 1981)

1.2.1 Fibrous Laminae

A *fibrous lamina* is a layer of unidirectional fibres or woven fibres in a matrix. Two typical lamina are shown in Figure 1.1 . The fibres are typically strong and stiff. They are the pricipal reinforcing or load-carrying parts. The role of the matrix is to maintain alignments of the fibres, to protect the fibres and to perform as a load distribution medium.

1.2.2 Laminates

A *laminate* is a stack of layers with different homogeneous elastic materials. Or it can also be composed of fibrous laminae with various orientations of principal material directions in the laminae. A major purpose of lamination is to construct the new material with strength and stiffness matching the loading environment of the structural element.

1.2.3 Laminated Circular Cylinders

A *laminated isotropic circular cylinder* is a circular cylinder which is composed of perfectly bonded isotropic elastic layers. The layers may have different mechanical properties, as well as different thicknesses. A *laminated composite circular cylinder*, unless otherwise stated, is define as a circular cylinder which is constructed from laminae with various orientations of principal material axes in the laminae perfectly bonded together. Manufacturing of laminated composite circular cylinders can be continuous pultrusion, centrifugal casting, or filament winding as shown in Figure 1.2. It should be mentioned herein that the contents of this thesis is directed to *circular cylinders.* For convenient purpose, therefore, *cylinders* will refer restrictly only to *circular cylinders.*

1.3 Ultrasonic Testing

Cylinders are used in many applications such as pressure tubes in nuclear reactor, platform struts, magnetometre boom and antenna-feed support struts in space structures (Broutman and Krock 1974), etc. The presence and growth of flaws in the cylinders are the major obstacles in their utilization and can have serious consequences during operation. In order to detect these flaws without impairing the usefulness of the cylinders, nondestructive testing has been exploited. The essential parts of any nondestructive test are (1) *application* of a testing or inspection medium, (2) *modification* of the testing or inspection medium by defects or variations in the structures or properties of the material, (3) *detection* of this change by a suitable detector, (4) *conversion* of this change into a form suitable for interpretation, and (5) *interpretation* of the information obtained. The testing technique itself may involve visual inspection, dye penetrant, magnetic particle, radiography, eddy current or ultrasonics. Such nondestructive tests are costly due to the high cost of the project's downtime. To reduce this downtime, more precise tests and

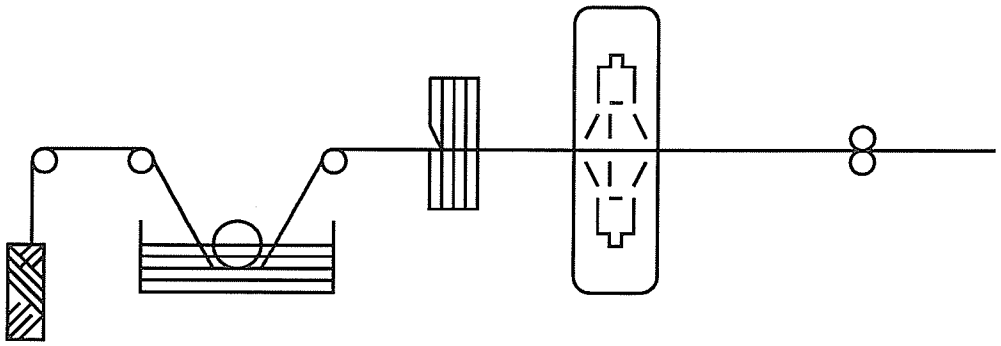

continuous pultrusion

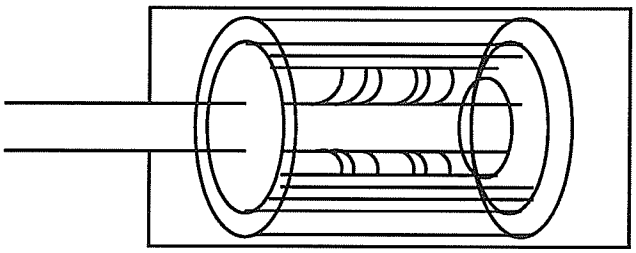

centrifugal casting

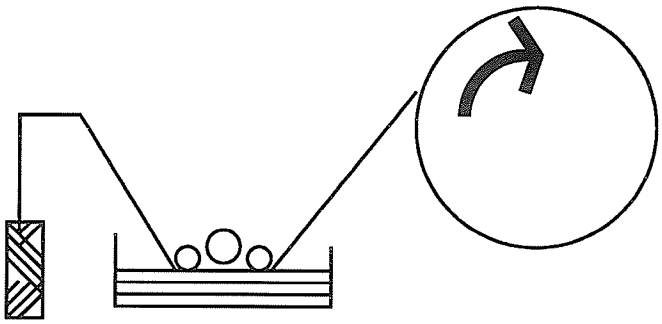

filament winding

Figure 1.2: Manufacturing of laminated composite circular cylinder
(source : Broutman, L.J. and Krock, R.H. 1974)

better data handling and processing are required. For ultrasonic testing, this includes better understanding of propagation of waves and their interaction with flaws.

The unique possibility that the use of ultrasonic waves has for detecting inhomogeneities in metals appears to have been first suggested in 1929 (Frederick 1965). The main idea of using ultrasonic in flaw detection is the reflection of waves by a crack or other abrupt change in the elastic properties of the material in which the waves are travelling. Figure 1.3 illustrates a block diagram of a typical ultrasonic flaw detector. A pulsed continuous or modulated ultrasonic beam is sent through the specimen and the amplitude of the transmitted waves measured. Inhomogeneity in the sample causes the waves to scatter. The amplitudes of transmitted and reflected waves are measured by receivers located on the surface of the specimen. The signals carry a substantial amount of information of the size, shape, and location of the flaw. Ultrasonic flaw detection techniques rely on the theoretical predictions of the amplitudes of transmitted and reflected signals. It is, however, very crucial to have a theoretical model which can accurately predict the scattering by flaws.

1.3.1 Guided Waves in Ultrasonic Testing for Laminated Cylinders

Several techniques have been used in ultrasonic testing such as: pulse echo, transmission, resonance, frequency modulation, and acoustic image. It should be noted herein that early techniques used body waves in ultrasonic test. New techniques employing guided waves are under development. There are several advantages in using guided waves in ultrasonic tests. First, their multimodal and dispersive behaviors can provide a large number of data points in a given range of frequency. Second, the velocity of guided waves is very sensitive to material properties of the cylinders. Finally, the velocity of guided waves can be very accurately measured as a function of frequency.

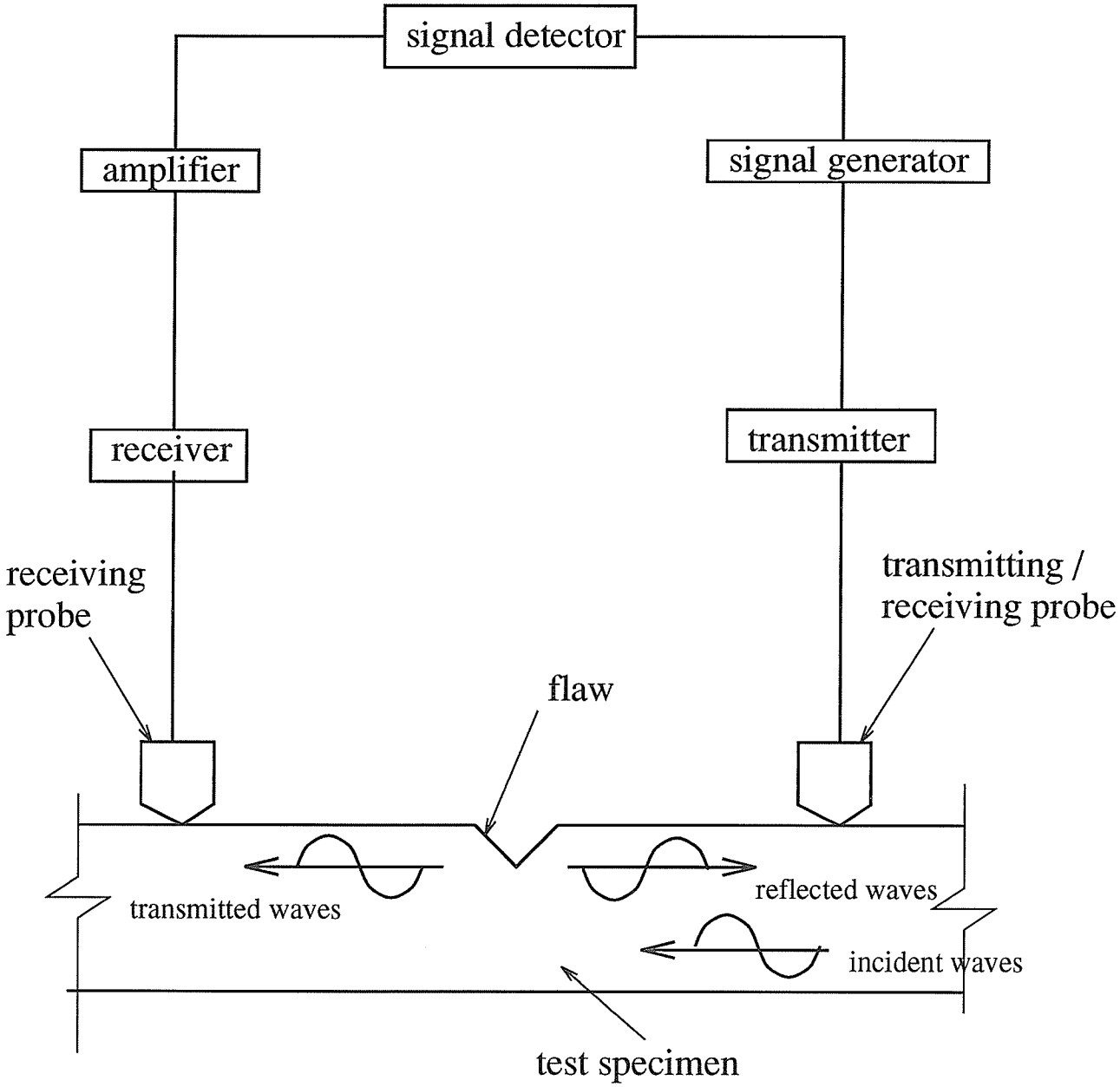

Figure 1.3: Schematic diagram of ultrasonic flaw detector.

In order to exploit guided waves in ultrasonic testing for laminated cylinders, dispersion characteristics of these waves need to be understood. The axially symmetric vibration of harmonic waves in an infinitely long homogeneous isotropic elastic cylindrical rod has been analytically investigated for over a century (Pochhammer 1876). The vibration is governed by frequency or dispersion equation which implicitly relates the frequency to the wavenumber. This requires the solution to satisfy the differential equations of linear elasticity throughout the cylinder and the traction free boundary conditions on the lateral surfaces. Although the equations were introduced as early as 1876, only in the past three decades have numerical results over a wide range of frequencies with complex wavenumbers been reported (Onoe *et al.* 1962). These complex wavenumbers, corresponding to non-propagating and evanescent modes, are essential in wave scattering and end reflection problems. In an infinite cylinder, however, only real wavenumbers or propagating modes are physically realisable.

Wave propagation in infinitely long homogeneous isotropic elastic hollow cylinders was investigated using the linear theory of elasticity by Gazis (1959), Armenàkas *et al.* (1969), etc. With this theory, they were able to generate the solutions without stipulation of axisymmetry. Various difficulties arise when the structure consists of a series of annular isotropic cylinders bonded together. However, within the framework of this elastic theory, many researchers successfully investigated the dispersion characteristics of harmonic waves in infinite laminated isotropic rods (McNiven *et al.*, 1963, Jai-Lue Lai, 1971, Armenàkas, 1965). Harmonic wave propagation in two layered isotropic cylinders was studied by Armenàkas (1967, 1971). The displacements and the stresses at the interface of each layer were analytically formulated. The dispersion relation was obtained from the boundary and the continuity conditions. Analogous to the work of Armenàkas, Moore (1990) applied the stiffness method to study the wave propagation in laminated isotropic rods and cylinders. The stiffness matrix which relates the stresses and the displacements at the interface of each layer was analytically established. The assembling process was then carried out in a subsequent layer.

Since the analytical formulation for laminated cylinders is intractible, several approximate techniques have been proposed to circumvent the problem. The most common ones are shell theories in which the contitutive relation of radially inhomogeneous cylinders is replaced by an integral form to reduce the problem to that of equivalent homogeneous cylinders (Tsai and Roy 1971, Sun and Whitney 1974). A list of references on various approximate cylindrical shell theories can be found in the paper by Barbero *et al.* (1990). The Ritz techniques, the numerical approximations using discretization in the radial direction to model radial inhomogeneity, have also been widely employed (Nelson *et al.* 1971, Huang and Dong 1984, Kohl *et al.* 1992). Nevertheless, efficient theoretical techniques in studying wave propagation and more informations on dispersion characteristics of waves in laminated cylinders are still required to fully utilize ultrasonic guided waves in flaw detection.

1.3.2 Free Edge Reflection in Cylinders

The free edge of a cylinder can be considered as a through-thickness crack which is an idealzed model of a normal edge crack. Hence, the reflection of waves at the free end can also be considered as a special case of wave scattering problem. The free end reflection of axisymmetric wave in an elastic rod was first investigated experimentally by Oliver (1957). McNiven (1961) employed the approximate three-mode theory to predict the existence of an end resonant frequency. His predicted value differed from Oliver's experimental results by 13 percent. Analogous to the work of McNiven, the problem was reconsidered using the 5, 7, and 9-mode approximations by Zemanek (1972). It was found that his result of the end resonant frequency with the 9-mode approximation differed by 0.5 percent as compared to that obtained by Oliver. However, the Poisson's ratio employed in his study was 0.3317 against 0.29 which was used by McNiven. Recently, Kim and Steele (1989) proposed a solution procedure which exploits the asymptotic behavior for higher harmonics in the radial direction to solve the problem. During the

same period, Gregory and Gladwell (1989) employed a least square technique to minimize the difference between the energy of the incident wave and that of the reflected waves. The end resonance phenomenon was also investigated and was found to depend strongly upon the Poisson's ratio. In their work, they predicted the end resonant frequency at the Poisson's ratio of 0.29 which differed from Oliver's result by 2.5 percent.

The free end reflection of the extensional waves in homogeneous isotropic elastic hollow cylinder was considered by McNiven and Shah (1967). The approximate three-mode theory was employed in the study to predict the resonant frequency. They found that the frequency of the end resonance for hollow cylinder was lower than that for solid rod. To the best of the author's knowledge, the free end reflection of waves in laminated cylinders has not yet been reported.

1.3.3 Tubing Inspection

Tubing inspection, Figure 1.4 (McGonnagle 1961), is one of the techniques used to test the longitudinal flaws in the cylinders. In such testings, waves are generated in the tangent direction of the tubes and will travel along circumferential direction. If a defect is encountered at the weld or crack, these waves will scatter and reflect back. Since waves are travelling in the circumferential direction and not in other directions, the problem can be considered as plane strain case. While there are numbers of theoretical investigation on wave scattering by cracks in plates (Abduljabbar *et al.* 1983, Koshiba *et al.* 1984, Karunasena *et al.* 1991), to the author's knowledge, the work in the cylindrical case has not yet been reported.

Not only can ultrasonics be utilized in flaw detection, it can also provide an effective means of characterizing elastic properties of composite or heterogeneous materials (Karunasena 1992). In order to interpret ultrasonic test results, it is necessary to have

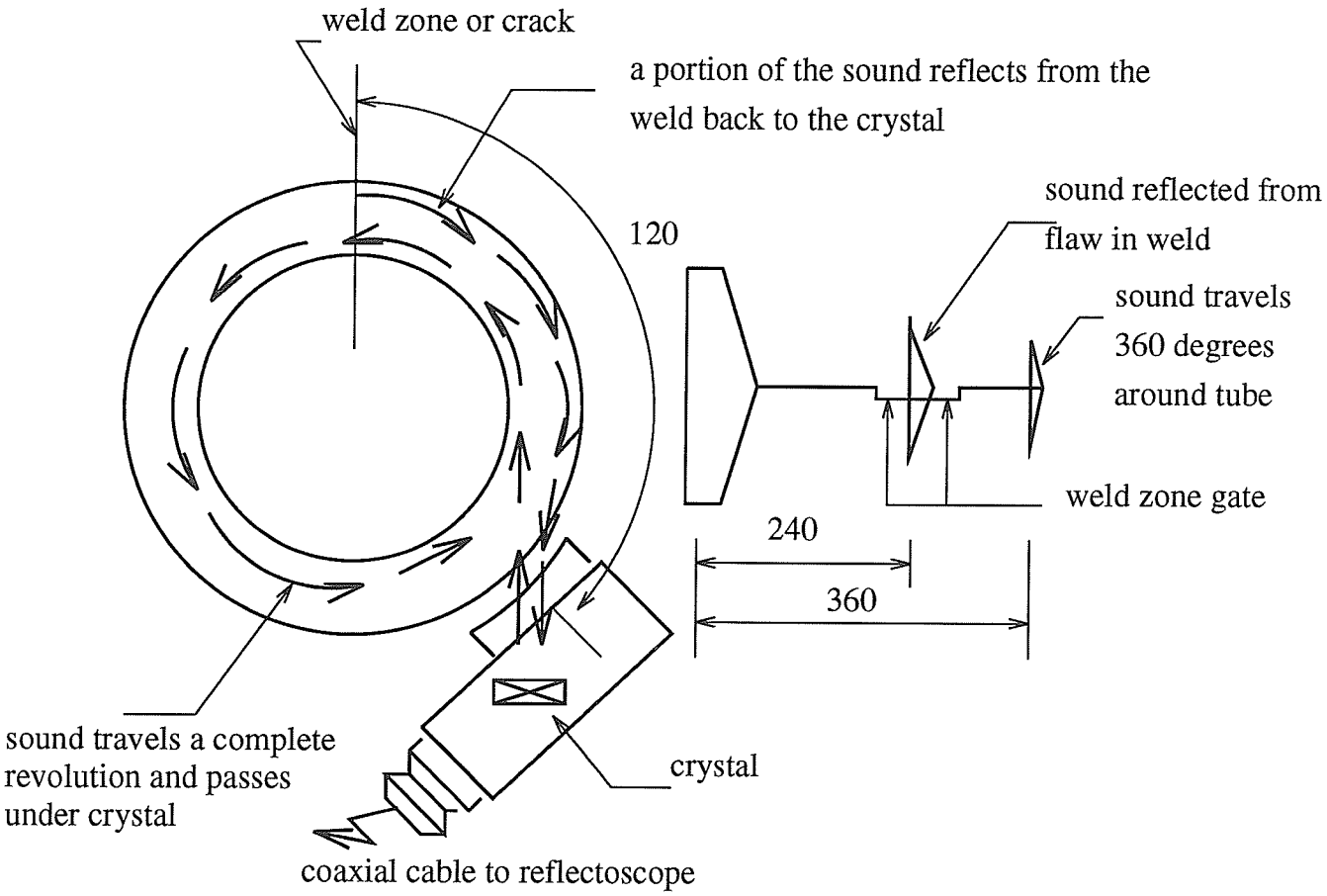

Figure 1.4: Testing of weld in tubing (source : McGonnagle, W.J. 1961)

theoretical predictions for dispersion characteristics of guided waves as functions of the properties to be characterized. Comparisons of test results with theoretical predictions help in determining unknown properties. Karunasena demonstrated that dispersive behavior of laminated plates could be studied by using effective elastic properties. Kohl *et al.* (1992) attempted to apply equivalent homogeneous properties to study the dispersion characteristic of laminated tubes. The results, however, illustrated that dispersive and modal behaviors of laminated cylinders were not the same as those of equivalent homogeneous ones at high frequencies.

1.4 An Overview of the Present Study

The main purpose of the present study is to investigate propagation and scattering of guided waves in laminated cylinders. An analytical method and Rayleigh-Ritz type approximations are employed to study the dispersion characteristics of free guided waves as well as the free end reflection problem. The investigation of this special case of scattering problem, the free end reflection, is carried out in detail using least-square and variational techniques. Plane strain wave scattering by cracks is studied by the hybrid method.

1.4.1 Elastic Wave Propagation

Three models of wave propagation are presented in the study. The analytical formulation, the propagator matrix method, is employed for laminated isotropic cylinders. This method is proposed to circumvent the difficulties in obtaining the exact dispersion relations of cylinders with arbitary number of isotropic layers. The results from this analytical technique are used as a benchmark for the approximate methods.

Two Rayleigh-Ritz type of approximations are presented to apply where the analytical solutions are unattainable. In these methods, the laminae are divided into several sublayers and the displacement distribution through the thickness of the sublayer is approximated by interpolation polynomials. These polynomial functions involve a number of discrete generalized coordinates, which may be only displacements or displacements and tractions at the interfaces between the adjoining sublayers. When the generalized coordinates are only displacements, the method ensures only the continuity of the displacements at the interfaces (nodal points). On the other hand, when the generalized coordinates are displacements and tractions, the method ensures the continuity of both the displacements and the stresses at the nodal points. The latter case of Rayleigh-Ritz

type of approximation is presented to ascertain the accuracy and the applicability of the former case of approximation.

The objective of this part of study is to obtain the appropriate and reliable model in order to apply to the wave scattering problems. Also the dispersion characteristics and the factors effecting the wave propagation are investigated in order to establish the basic knowledge for the wave scattering problems.

Numerical experimentations illustrate that the Rayleigh-Ritz type of approximation with only displacement continuity yields sufficient accuracy in applying to the study of wave scattering in the laminated cylinders. In addition, many factors, like circumferential wavenumber, ply-lay up configurations, and the thickness to radius ratio which alter the dispersion characteristics are very important in the scattering problems.

1.4.2 Reflection of Wave at Free Edge

A wave function expansion is employed to solve the reflection problem when time harmonic elastic waves impinge upon the free end of semi-infinite laminated cylinders. The reflected field is represented by the superposition of a finite number of wave functions. The propagator matrix approach is applied to obtain the wave functions for laminated isotropic cylinders while Rayleigh-Ritz type of approximation with displacement continuity is used for laminated composite cylinders. The least square technique as well as the variational method are employed to evaluate the complex amplitudes and the energy fluxes associated with the reflected field. The accuracy and the effectiveness of the method is illustrated by comparing the results with existing analytical results and the satisfaction of the principle of energy conservation.

1.4.3 Plane Strain Wave Scattering by Cracks

A hybrid method is employed to solve the scattering problem of time harmonic elastic plane strain wave in the laminated cylinders. The method incorporates finite element formulation in a bounded interior region with a wave function expansion representation in the exterior region. The bounded interior region is composed of flaws and/or loads and a finite region of the cylinder surrounding these flaws and/or loads. The wave functions are obtained by the Rayleigh-Ritz type of approximation with only displacement as generalized coordinates. Continuity conditions for the displacements and the interaction forces are imposed at the nodes lying along the boundaries between the two regions. This results in a system of linear algebraic equations which is solved for the unknown wave function amplitudes. This investigation is motivated from the application of ultrasonic in tubing inspection. The numerical results for the scattered amplitudes from load and from flaw are presented for Zr-Nb pressure tube used in CANDU Pressurized Heavy Water reactors to illustrate the applicabilty and the accuracy of the method.

1.5 Organization of the Thesis

This thesis is mainly concerned with the investigation of propagation and scattering of guided waves in laminated cylinders. An analytical model and approximate models are proposed in Chapter 2 to study the dispersion characteristics of waves in laminated cylinders and to obtain the appropriate method to apply in the scattering problems. The effects of thickness to radius ratio, circumferential wavenumber, ply lay-up configuration and anisotropy on the dispersion characteristics are elaborated in detail. The wave scattering problems are presented in Chapters 3 and 4. Free end reflection problem, a special case of wave scattering problem, is considered in Chapter 3. The formulation of the hybrid method for plane strain wave scattering by flaws in cylindrical cross section

is presented in Chapter 4. Conclusions and some recommendations for future study are outlined in Chapter 5.

Chapter 2

Elastic Wave Propagation in Laminated Cylinders

2.1 General

In this chapter, elastic wave propagation in laminated cylinders is investigated in detail. As mentioned in Chapter 1, three wave propagation models are presented: analytical formulation and two Rayleigh-Ritz type approximations. In the analytical formulation, a propagator matrix approach, the three-dimensional theory of isotropic elasticity is exploited to formulate the relation of the stresses and displacements of one interface of a layer to those of another interface. The propagator matrix, established from this relation, generates the frequency equation of the cylinder. In the Rayleigh-Ritz type approximations, the displacements are approximated by the interpolation of discrete nodal (interface) generalized coordinates. These nodal coordinates may be displacements only or displacements and stresses at nodal points. The frequency equation of the cylinder in the form of an eigenvalue problem is formulated by applying Hamilton's principle. The main objective of presenting these models is to obtain the dispersion relations and thereby

to study guided wave propagation in laminated cylinders. The effects on dispersion characteristics from circumferential wavenumber, thickness to radius ratio of the cylinder, number of layers in the cylinder, and degree of anisotropy are also investigated. The numerical results from the two approximate models are compared to select the suitable and reliable method to study some of the wave scattering problems which will be discussed in Chapters 3 and 4.

2.2 Description of the Problem

Time harmonic elastic wave propagation in an infinite laminated cylinder is considered. The layers may have distinct mechanical properties as well as different thicknesses. The cylinder is in (r, θ, z) coordinate system as shown in Figure 2.1. The direction of wave propagation is z. The two lateral surfaces of the cylinder (i.e. the inner and outer surfaces) are free of traction. In the techniques adopted here, each layer is divided into several sublayers although it is not necessary for the analytical method. The total number of sublayers through the thickness, H, is N. The mean radius of the cylinder is R.

2.3 Analytical Method

In this section, analytical formulation model which in the remainder of this thesis will be referred to as *the propagator matrix method* is presented.

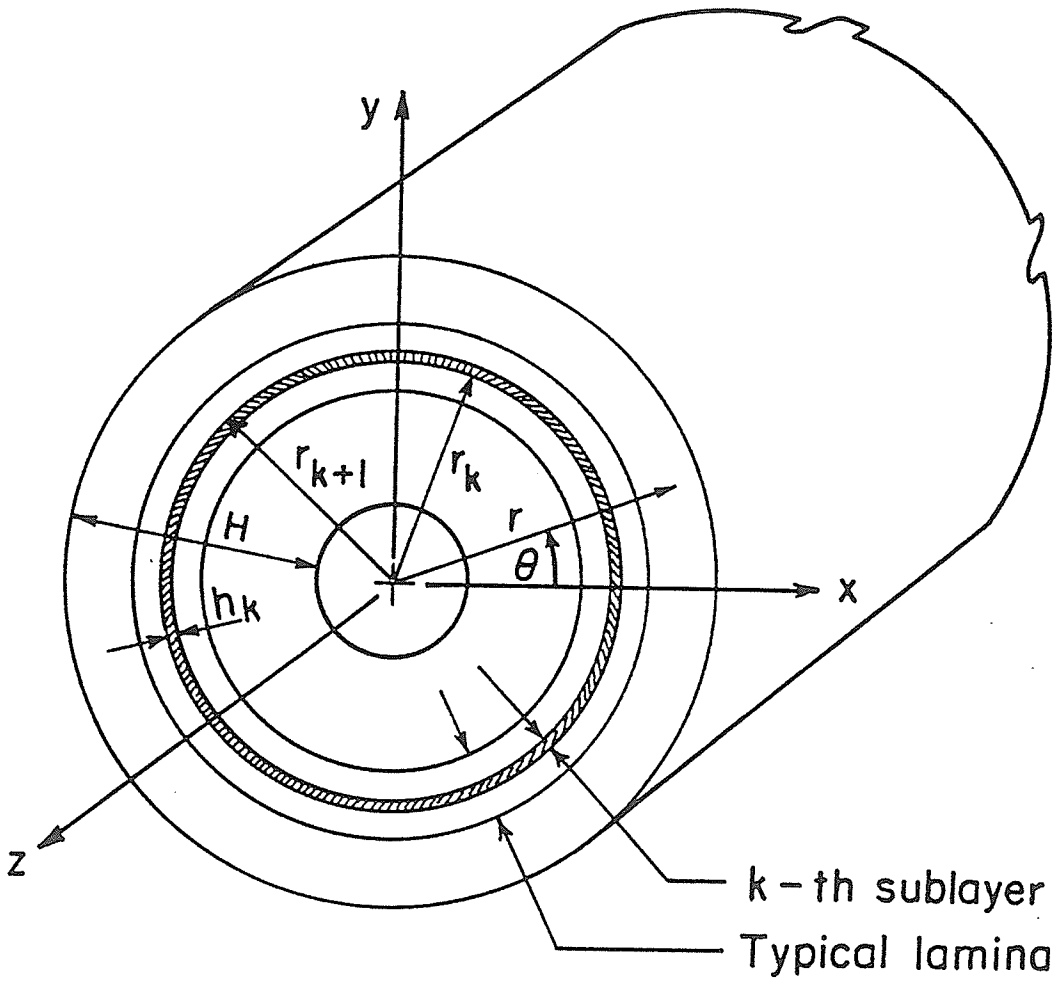

Figure 2.1: Geometry of laminated cylinder

2.3.1 Governing Equations

Since the main concern of this thesis is with cylinders having varying number of layers, the analytical formulation will be constructed in such a way that the number and the properties of layers can be arbitrarilly varied without any change in the solution procedure. Consider the k^{th} isotropic sublayer bounded by $r = r_{\text{k}}$ and $r = r_{\text{k+1}}$ surfaces. With reference to the cylindrical coordinates, r, θ, and z, and the respective displacement components u, v, and w, the displacement equations of motion are:

$$\begin{aligned}
(\lambda+2\mu)\frac{\partial \tilde{u}}{\partial r} - \frac{2\mu}{r}\frac{\partial w_z}{\partial \theta} + 2\mu\frac{\partial w_\theta}{\partial z} &= \rho\frac{\partial^2 u}{\partial t^2}, \\
(\lambda+2\mu)\frac{1}{r}\frac{\partial \tilde{u}}{\partial \theta} - 2\mu\frac{\partial w_r}{\partial z} + 2\mu\frac{\partial w_z}{\partial r} &= \rho\frac{\partial^2 v}{\partial t^2}, \\
(\lambda+2\mu)\frac{\partial \tilde{u}}{\partial z} + \frac{2\mu}{r}\frac{\partial w_r}{\partial \theta} - \frac{2\mu}{r}\frac{\partial (w_\theta r)}{\partial r} &= \rho\frac{\partial^2 w}{\partial t^2},
\end{aligned} \tag{2.1}$$

where λ and μ are Lamé's constants, ρ is the mass density and t denotes the time. $\tilde{u}$, w_r, w_θ, and w_z are defined as:

$$\begin{aligned}
\tilde{u} &= \frac{\partial u}{\partial r} + \frac{u}{r} + \frac{1}{r}\frac{\partial v}{\partial \theta} + \frac{\partial w}{\partial z}, \\
2w_r &= \frac{1}{r}\frac{\partial w}{\partial \theta} - \frac{\partial v}{\partial z}, \\
2w_\theta &= \frac{\partial u}{\partial z} - \frac{\partial w}{\partial r}, \\
2w_z &= \frac{v}{r} + \frac{\partial v}{\partial r} - \frac{1}{r}\frac{\partial u}{\partial \theta}.
\end{aligned} \tag{2.2}$$

The displacement components u, v, and w can be written in terms of the potentials ϕ, H_r, H_θ, and H_z as (Armenàkas *et al.* 1969):

$$\begin{aligned}
u &= \frac{\partial \phi}{\partial r} + \frac{1}{r}\frac{\partial H_z}{\partial \theta} - \frac{\partial H_\theta}{\partial z}, \\
v &= \frac{1}{r}\frac{\partial \phi}{\partial \theta} + \frac{\partial H_r}{\partial z} - \frac{\partial H_z}{\partial r}, \\
w &= \frac{\partial \phi}{\partial z} + \frac{1}{r}\frac{\partial}{\partial r}\big(rH_\theta\big) - \frac{1}{r}\frac{\partial H_r}{\partial \theta},
\end{aligned} \tag{2.3}$$

where

$$\phi = f(r)e^{im\theta}e^{-i(\xi z-\omega t)},$$

$$
\begin{aligned}
H_r &= g_r(r)e^{im\theta}e^{-i(\xi z-\omega t)}, \\
H_\theta &= g_\theta(r)e^{im\theta}e^{-i(\xi z-\omega t)}, \\
H_z &= g_z(r)e^{im\theta}e^{-i(\xi z-\omega t)}.
\end{aligned} \tag{2.4}
$$

m is the circumferential wave number, ω is the circular frequency, ξ is the wave number in the $z-$direction and $i = \sqrt{-1}$.

The displacement equations of motion, equations (2.1), are satisfied if:

$$
\begin{aligned}
f'' + \frac{1}{r}f' - \Big(\frac{m^2}{r^2} - \alpha^2\Big)f &= 0, \\
g_r'' + \frac{1}{r}g_r' - \Big(\frac{(m+1)^2}{r^2} - \beta^2\Big)g_r &= 0, \\
g_z'' + \frac{1}{r}g_z' - \Big(\frac{m^2}{r^2} - \beta^2\Big)g_z &= 0,
\end{aligned} \tag{2.5}
$$

where

$$
\alpha^2 = \frac{\omega^2}{v_p^2} - \xi^2 \quad ; \quad \beta^2 = \frac{\omega^2}{v_s^2} - \xi^2, \tag{2.6}
$$

and $g_\theta(r) = -ig_r(r)$. Prime denotes the differentiation with respect to r. v_p and v_s are the velocity of dilatational and torsional waves, respectively, and are defined as follows:

$$
v_p^2 = \Big(\frac{\lambda + 2\mu}{\rho}\Big) \quad ; \quad v_s^2 = \frac{\mu}{\rho}. \tag{2.7}
$$

The general solutions to equations (2.5) in terms of Hankel functions are:

$$
\begin{aligned}
f(r) &= A_1 H_m^{(1)}(\alpha r) + B_1 H_m^{(2)}(\alpha r), \\
g_r(r) &= A_2 H_{m+1}^{(1)}(\beta r) + B_2 H_{m+1}^{(2)}(\beta r), \\
g_z(r) &= A_3 H_m^{(1)}(\beta r) + B_3 H_m^{(2)}(\beta r).
\end{aligned} \tag{2.8}
$$

A_1, A_2, A_3, B_1, B_2, and B_3 are arbitrary constants for the layer. By substituting equations (2.8) into equations (2.4) and (2.3), together with the conventional stress-strain and strain-displacement relations, the displacement and stress components at the interface $r = r_k$ can be presented as:

$$
\begin{Bmatrix} \{U_k\} \\ \{S_k\} \end{Bmatrix} = \begin{bmatrix} D_k \end{bmatrix} \begin{Bmatrix} \{A\} \\ \{B\} \end{Bmatrix}, \tag{2.9}
$$

where

$$\{U_k\}^{\mathrm{T}} = \langle u_k \quad v_k \quad w_k \rangle \qquad ; \qquad \{S_k\}^{\mathrm{T}} = \langle \sigma_k \quad \tau_k \quad \chi_k \rangle,$$
$$\{A\}^{\mathrm{T}} = \langle A_1 \quad A_2 \quad A_3 \rangle \qquad ; \qquad \{B\}^{\mathrm{T}} = \langle B_1 \quad B_2 \quad B_3 \rangle. \tag{2.10}$$

Superscript T represents the transpose. σ, τ, and χ denote the stress components σ_{rr}, $\sigma_{r\theta}$, and σ_{rz}, respectively. Subscript k designates the nodal values at the k^{th} interface. The six by six matrix, $[D_k]$, containing Hankel functions $H_m^{(1)}$ and $H_m^{(2)}$, is given in Appendix A.

By evaluating the displacement and the stress components at the surface $r = r_{k+1}$ of the k^{th} layer using the aforementioned procedure and incorporating equation (2.9), the following relation can be obtained:

$$\begin{Bmatrix} \{U_{k+1}\} \\ \{S_{k+1}\} \end{Bmatrix} = \begin{bmatrix} P_k \end{bmatrix} \begin{Bmatrix} \{U_k\} \\ \{S_k\} \end{Bmatrix}, \tag{2.11}$$

where

$$[P_k] = [D_{k+1}][D_k]^{-1}. \tag{2.12}$$

The six by six matrix $[P_k]$ is the propagator matrix for the k^{th} layer. Superscript -1 denotes the inverse of the matrix. Repeated application of equation (2.11) for every layer in a cylinder consisted of N layers results in:

$$\begin{Bmatrix} \{U_{N+1}\} \\ \{S_{N+1}\} \end{Bmatrix} = \begin{bmatrix} P \end{bmatrix} \begin{Bmatrix} \{U_1\} \\ \{S_1\} \end{Bmatrix}, \tag{2.13}$$

where

$$\begin{bmatrix} P \end{bmatrix} = \begin{bmatrix} P_N \end{bmatrix} \begin{bmatrix} P_{N-1} \end{bmatrix} \cdots \begin{bmatrix} P_1 \end{bmatrix}. \tag{2.14}$$

The matrix $[P]$ can be partitioned as:

$$[P] = \begin{bmatrix} [P]_{11} & [P]_{12} \\ [P]_{21} & [P]_{22} \end{bmatrix}. \tag{2.15}$$

Invoking the zero traction conditions at the inner and the outer radii of the cylinder simplifies equation (2.13) to:

$$[P]_{21}\{U_1\} = \{0\}. \tag{2.16}$$

The exact dispersion relation can then be obtained by equating the determinant of the coefficient matrix to zero. i.e.;

$$|[P]_{21}| = 0. \tag{2.17}$$

This relation can be used to evaluate ω for a given ξ, or alternately, for a given ω it can be solved for ξ.

2.3.2 Solid Rods

For the solid rod problem, the Weber's function, Y_m, becomes indeterminate when r equals zero. Consequently, the general solutions, equations (2.8) becomes:

$$\begin{aligned} f(r) &= C_1 J_m(\alpha r), \\ g_r(r) &= C_2 J_{m+1}(\beta r), \\ g_z(r) &= C_3 J_m(\beta r), \end{aligned} \tag{2.18}$$

for the inner layer of the solid rod bounded by $r = 0$ and $r = r_1$ surfaces where J_m is Bessel function of the first kind. C_1, C_2, and C_3 are arbitrary constants for this layer. The displacement and stress components at the interface $r = r_1$ can be written in terms of these constants as:

$$\begin{aligned} \{U_1\} &= [R]\{C\}, \\ \{S_1\} &= [T]\{C\}, \end{aligned} \tag{2.19}$$

where

$$\{C\}^T = \langle C_1 \quad C_2 \quad C_3 \rangle.$$

$[R]$ and $[T]$ are three by three matrices, containing the Bessel function J_m, and are given in Appendix A. The stiffness matrix, $[K]$, relating the stresses and the displacements can be obtained from equations (2.19) as:

$$\{S_1\} = [T][R]^{-1}\{U_1\} = [K]\{U_1\}. \tag{2.20}$$

The propagator matrix in equation (2.13), nevertheless, can still be employed for the first interface to the $(N+1)^{\text{th}}$ interface. The insertion of equation (2.20) into equation (2.13) yields:

$$\left\{ \begin{array}{c} \{U_{N+1}\} \\ \{S_{N+1}\} \end{array} \right\} = \left[\begin{array}{c} [P]_{11} + [P]_{12}\,[K] \\ [P]_{21} + [P]_{22}\,[K] \end{array} \right] \left\{ \{U_1\} \right\}. \tag{2.21}$$

By invoking the boundary condition of the traction free surface at the outer radius of the rod , the dispersion relation of the solid rod can be written as:

$$|[P]_{21} + [P]_{22}[K]| = 0. \tag{2.22}$$

2.4 Rayleigh-Ritz Type Approximations

Nelson *et al.* (1971) presented an *extended Ritz technique* using discretization in the radial direction in order to model radial inhomogeneity. The technique was applied to study dispersion in laminated cylinders with general orthotropic layers. Huang and Dong (1984) expanded the study by applying the same method to laminated cylinders with general anisotropic layers. The complex frequency spectrum for laminated composite cylinders were presented in their study. Only modal behavior was considered in the former of these studies. In this section, the method is extended to investigate the wave propagation in laminated cylinders.

Consider the k^{th} anisotropic sublayer bounded by $r = r_{\text{k}}$ and $r = r_{\text{k+1}}$ surfaces. The sublayer has anisotropic modulii C^{k}_{pq} $(p, q = 1, 2, \ldots, 6)$ and density ρ_{k}. In general, fibre-reinforced composites will have the form of material symmetry. However, when the fibres make an angle with the coordinate direction, their properties will appear as transverse isotropic. With reference to the cylindrical coordinates (r, θ, z), the stress-strain relation

for the k^{th} sublayer is given by:

$$\begin{Bmatrix} \sigma_{rrk} \\ \sigma_{\theta\theta k} \\ \sigma_{zzk} \\ \sigma_{\theta zk} \\ \sigma_{rzk} \\ \sigma_{r\theta k} \end{Bmatrix} = \begin{bmatrix} C_{11}^{\mathrm{k}} & C_{12}^{\mathrm{k}} & C_{13}^{\mathrm{k}} & C_{14}^{\mathrm{k}} & C_{15}^{\mathrm{k}} & C_{16}^{\mathrm{k}} \\ C_{12}^{\mathrm{k}} & C_{22}^{\mathrm{k}} & C_{23}^{\mathrm{k}} & C_{24}^{\mathrm{k}} & C_{25}^{\mathrm{k}} & C_{26}^{\mathrm{k}} \\ C_{13}^{\mathrm{k}} & C_{23}^{\mathrm{k}} & C_{33}^{\mathrm{k}} & C_{34}^{\mathrm{k}} & C_{35}^{\mathrm{k}} & C_{36}^{\mathrm{k}} \\ C_{14}^{\mathrm{k}} & C_{24}^{\mathrm{k}} & C_{34}^{\mathrm{k}} & C_{44}^{\mathrm{k}} & C_{45}^{\mathrm{k}} & C_{46}^{\mathrm{k}} \\ C_{15}^{\mathrm{k}} & C_{25}^{\mathrm{k}} & C_{35}^{\mathrm{k}} & C_{45}^{\mathrm{k}} & C_{55}^{\mathrm{k}} & C_{56}^{\mathrm{k}} \\ C_{16}^{\mathrm{k}} & C_{26}^{\mathrm{k}} & C_{36}^{\mathrm{k}} & C_{46}^{\mathrm{k}} & C_{56}^{\mathrm{k}} & C_{66}^{\mathrm{k}} \end{bmatrix} \begin{Bmatrix} \epsilon_{rrk} \\ \epsilon_{\theta\theta k} \\ \epsilon_{zzk} \\ \gamma_{\theta zk} \\ \gamma_{rzk} \\ \gamma_{r\theta k} \end{Bmatrix} \tag{2.23}$$

2.4.1 Displacement Based Rayleigh-Ritz Type Approximation

Let the diplacement components u, v, and w be approximated by interpolation polynomials in the radial direction as:

$$\{U\} = [N]\{\tilde{q}\}, \tag{2.24}$$

where

$$\{U\}^{\mathrm{T}} = \langle u \;\; v \;\; w \rangle, \tag{2.25}$$

$$\{\tilde{q}\}^{\mathrm{T}} = \left\langle u^b \;\; v^b \;\; w^b \;\; u^m \;\; v^m \;\; w^m \;\; u^f \;\; v^f \;\; w^f \right\rangle, \tag{2.26}$$

$$[N] = \begin{bmatrix} n_1 & 0 & 0 & n_2 & 0 & 0 & n_3 & 0 & 0 \\ 0 & n_1 & 0 & 0 & n_2 & 0 & 0 & n_3 & 0 \\ 0 & 0 & n_1 & 0 & 0 & n_2 & 0 & 0 & n_3 \end{bmatrix}. \tag{2.27}$$

In equations (2.24)-(2.26), the generalized displacements u^b, u^m, u^f are taken at the back (inner), middle, and front (outer) nodal surfaces of the sublayer. The interpolation polynomials n_i are quadratic functions given by:

$$n_1 = 1 - 3\eta + 2\eta^2 \quad ; \quad n_2 = 4\eta - 4\eta^2 \quad ; \quad n_3 = -\eta + 2\eta^2, \tag{2.28}$$

where $\eta = (r - r_{\mathrm{k}})/h_{\mathrm{k}}$, h_{k} being the thickness of the k^{th} sublayer.

By using Hamilton's principle, the Lagrangian, L_{k}, for the k^{th} anisotropic sublayer is

calculated as:

$$L_{\mathrm{k}} = \frac{1}{2}\int_t\int_z\int_\theta\Big\{\int_{r_{\mathrm{k}}}^{r_{\mathrm{k}+1}}\Big[\rho_{\mathrm{k}}\left\{\dot{\bar{U}}\right\}^{\mathrm{T}}\left\{\dot{U}\right\} - \{\bar{\epsilon}\}^{\mathrm{T}}\left[C^{\mathrm{k}}\right]\{\epsilon\}\Big]rdr\Big\}d\theta dzdt. \tag{2.29}$$

Overbar and overdot denote complex conjugate and time differentiation, respectively. $\{\epsilon\}$ represents the strain vector with six strain components given in equation (2.23).

By substituting equation (2.24) into strain-displacement relations and these in turn in equation (2.29), the Lagrangian can be written in term of generalized coordinates, equation (2.26). Upon setting the first variation of the summation of the contribution from all sublayers to zero, the governing equation for the entire cylinder is obtained as:

$$[K_1]\{\tilde{Q}\}'' + [K_2]\{\tilde{Q}\}' - [K_3]\{\tilde{Q}\} - [M]\{\ddot{\tilde{Q}}\} = 0. \tag{2.30}$$

The matrices $[M]$, $[K_1]$, $[K_2]$, and $[K_3]$ are defined in Appendix B. Here $[K_1]$ and $[M]$ are real symmetric, $[K_2]$ is skew-hermitian and $[K_3]$ is hermitian. Prime denotes differentiation with respect to z. The vector $\{\tilde{Q}\}$ contains the generalized nodal coordinates for the cylinder.

A solution representing harmonic wave propagation for equation (2.30) can be assumed in the form:

$$\{\tilde{Q}\} = \{Q_0\}e^{-i(\xi z - \omega t)}e^{im\theta}, \tag{2.31}$$

where $\{Q_0\}$ represents the nodal amplitude vector. Substitution of equation (2.31) into equation (2.30) results in a set of linear homogeneous equations as:

$$\Big\{-\xi^2[K_1] - i\xi[K_2] - [K_3] + \omega^2[M]\Big\}\{Q_0\} = 0. \tag{2.32}$$

For a nontrivial solution $\{Q_0\}$ the determinant of the coefficient matrix must be zero and this results in quadratic algebraic eigenvalue problem for ξ when ω is specified. This equation serves as the dispersion relation for the cylinder.

2.4.2 Displacement and Stress Based Rayleigh-Ritz Type Approximation

In this section, the displacements at a point in the k^{th} anisotropic sublayer are approximated by interpolation polynomials as:

$$\{U\} = [N_1]\{\tilde{q}\}' + [N_2]\{\tilde{q}\}, \tag{2.33}$$

where

$$\{\tilde{q}\}^{\mathrm{T}} = \left\langle u^b \quad \sigma^b \quad v^b \quad \tau^b \quad w^b \quad \chi^f \quad u^f \quad \sigma^f \quad v^f \quad \tau^f \quad w^f \quad \chi^f \right\rangle. \tag{2.34}$$

$[N_1]$ and $[N_2]$ are given in Appendix C. The generalized coordinates, $\{\tilde{q}\}$, which are displacements and tractions are taken at the back (inner) and front (outer) nodal surfaces of the sublayer.

By using Hamilton's principle, following the procedure presented in section 2.4.1, the governing equation for the cylinder is found to be:

$$\begin{aligned}[K_4]\{\tilde{Q}\}^{iv} \;+\; & [K_5]\{\tilde{Q}\}''' + \left\{[E_1]\{\tilde{Q}\}'' - [C_1]\{\ddot{\tilde{Q}}\}''\right\} + \left\{[E_2]\{\tilde{Q}\}' - [C_2]\{\ddot{\tilde{Q}}\}'\right\} \\ + \; & \left\{[E_3]\{\tilde{Q}\} + [M_1]\{\ddot{\tilde{Q}}\}\right\} = 0. \end{aligned} \tag{2.35}$$

The matrices $[C_1]$, $[C_2]$, $[M_1]$, $[K_4]$, $[K_5]$, and $[E_1]$ through $[E_3]$ are defined in Appendix C. Note that $[C_1]$ and $[K_4]$ are real symmetric, $[M_1]$, $[E_1]$, and $[E_3]$ are hemitian, and $[C_2]$, $[K_5]$, and $[E_2]$ are skew-hermitian. With the assumption of a solution to harmonic wave propagation be in the form as in equation (2.31), a set of homogeneous equations can be obtained from the above equation as:

$$\left\{\xi^4[K_4] + i\xi^3[K_5] - \xi^2[K_6] - i\xi[K_7] + [K_8]\right\}\{Q_0\} = 0, \tag{2.36}$$

where

$$\begin{aligned}[K_6] &= [E_1] + \omega^2[C_1] \\ [K_7] &= [E_2] + \omega^2[C_2] \\ [K_8] &= [E_3] - \omega^2[M_1] \end{aligned} \tag{2.37}$$

Again, for a nontrivial solution, the determinant of the coefficients matrix must be zero. This results in the fourth order eigenvalue problem which serves as the dispersion relation to solve for ξ when ω is specified. Alternatively, for a given ξ, the dispersion relation can be written in the form of standard eigenvalue problem to solve for ω as:

$$[K_\xi]\{Q_0\} = \omega^2 [M_\xi]\{Q_0\}, \tag{2.38}$$

where

$$\begin{aligned} [K_\xi] &= \xi^4 [K_4] + i\xi^3 [K_5] - \xi^2 [E_1] - i\xi [E_2] + [E_3], \\ [M_\xi] &= [M_1] + \xi^2 [C_1] + i\xi [C_2]. \end{aligned} \tag{2.39}$$

It should be noted here that the generalized coordinates (equation (2.26)) in section 2.4.1 are nodal displacement values. The method therefore ensures only the continuity of displacements at the interfaces of the sublayers. Here, the generalized coordinates, equation (2.34), are displacements and tractions at the nodal points. The method thus assures the continuity of both the displacements and the stresses at the interfaces. For convenience, in what follows in this thesis, the displacement based Rayleigh-Ritz type approximation will be referred to as *displacement continuity method* whilst the stress and displacement based Rayleigh-Ritz type approximation will be referred to as *stress continuity method.*

2.5 Roots of Dispersion Equations

Dispersion equations obtained in sections 2.3 and 2.4 can be used to evaluate ω for a given ξ, or alternately, for a given ω, they can be solved for ξ. Due to physical reasons, only real values are acceptable for the frequency, ω. The wavenumber, ξ, on the other hand, can have the complex form. For $z \geq 0$, the complex wavenumber, ξ, is admissible only in the form of:

$$\xi = \xi_R - i\xi_I, \tag{2.40}$$

where ξ_R and ξ_I are real and imaginary parts of complex wavenumber, respectively. From the viewpoint of the stability of the system, only $\xi_I \geq 0$ is admissible. The roots with $\xi_I = 0$ and $\xi_R > 0$ produce modes propagating in the positive $z-$direction. In contrast, when $\xi_R = 0$ and $\xi_I > 0$, the modes are non-propagating. When ξ_R and ξ_I are both non-zero, the modes are evanescent for which edge vibrations occurs - that is, the motions are confined near the edge. For an infinite cylinder, only propagating modes exist from the physical standpoint of the system. The non-propagating and evanescent modes, however, are significant in the problem of semi-infinite and finite cylinders with prescribed end conditions. It can be shown that if ξ is a root of the dispersion relation, then $-\bar{\xi}$ is also a root. This conforms to the physical condition that waves may propagate in either the positive or the negative $z-$direction.

The main interest here is to obtain the frequency spectrum (plot of frequency vs wavenumber). Since the wavenumber can be in complex form, the frequency spectrum has three different kinds of branches: real, imaginary, and complex (for detail see Mindlin 1960) corresponding to real, imaginary, and complex roots for ξ, respectively. The real branches corresponding with the propagating modes are the branches which dominate the dynamic response of the cylinder. The imaginary and complex branches represent non-propagating and evanescent modes, respectively, and these modes decay with z.

An approximation to the frequency spectrum can be obtained by using Rayleigh-Ritz type approaches. The real branches of the approximate spectrum can easily be plotted by solving the standard eigenvalue problems given by equation (2.32) or (2.38). However, if imaginary and complex branches of the approximate frequency spectrum are to be obtained, then the quadratic, equation (2.32), or the fourth order eigenvalue problem, equation (2.36), which involves greater amount of computer time and core memory, has to be solved. It may be noted that, in solving for real branches, the stress continuity method requires less computational time than the displacement continuity approach for the same number of sublayers. This is because, with the same number of sublayers modelled, the

number of degrees of freedom provided by the stress continuity method is less than that provided by the displacement continuity approach.

For a fixed value of either ω or ξ, the exact dispersion relations obtained in section 2.3 are transcendental functions of either ξ or ω, respectively. It is possible to evaluate the roots of these equations by some search method. This approach will be computationally formidable since the roots are sparsely scattered. Herein, Muller's method (Muller 1956) is employed to recover the exact roots in the propagator matrix approach. Approximate roots obtained from either the displacement continuity or the stress continuity approach are used as initial guesses in the Muller's method. If the roots are required over a given range of ξ (or ω), approximate roots from the Rayleigh-Ritz type approaches are required only at the first step to use as initial guesses. At the next step, ξ (or ω) is changed by a small increment and the exact dispersion relation is solved taking the exact roots from the previous step as initial guesses for the current step. The process is repeated until the range of interest is scanned.

Note that the exact dispersion relation in section 2.3 contains the Hankel functions for complex arguments. These Hankel functions are obtained from the relations between solutions as (National Bureau of Standard 1964):

$$\begin{aligned} H_m^{(1)}(\zeta r) &= J_m(\zeta r) + iY_m(\zeta r), \\ H_m^{(2)}(\zeta r) &= J_m(\zeta r) - iY_m(\zeta r), \end{aligned} \tag{2.41}$$

where ζr denotes αr or βr in equation (2.8). IMSL subroutine (1984) is employed to evaluate the Bessel function of the first kind for complex arguments, $J_m(\zeta r)$. Following the formula given in the National Bureau of Standard (1964), a computer code is written to evaluate the Weber's function, $Y_m(\zeta r)$ for complex arguments. This computer code is validated against Walfram (1988). For a thin cylinder, however, where r is large compared to the thickness, H, of the cylinder, the argument ζr of the Hankel functions becomes magnified. The Hankel functions for this case are evaluated by using the asymptotic

expansion forms (National Bureau of Standard 1964):

$$\begin{aligned} H_m^{(1)}(\zeta r) &= \sqrt{\tfrac{2}{(\pi\zeta r)}}\Big\{E(m,\zeta r)+iF(m,\zeta r)\Big\}e^{i(\zeta r)}e^{-i(m/2+1/4)\pi}, \\ H_m^{(2)}(\zeta r) &= \sqrt{\tfrac{2}{(\pi\zeta r)}}\Big\{E(m,\zeta r)-iF(m,\zeta r)\Big\}e^{-i(\zeta r)}e^{i(m/2+1/4)\pi}, \end{aligned} \tag{2.42}$$

where $E(m,\zeta r)$ and $F(m,\zeta r)$ are given in Appendix D. Note that $E(m,\zeta r)$ and $F(m,\zeta r)$ are well behaved for any argument of ζr. However, the Hankel functions may not be bounded due to the exponent terms. When $|\mathrm{Im}(\zeta r)|$ is large, one of the Hankel functions is exponentially magnified while another is comparatively very small. The numerical evaluation for this case becomes inaccurate and causes singularity in the matrix $[D_k]$ in equation (2.9). Since the value of ζ is fixed for any pair of ω and ξ, the only control variable therefore is r. Multiplying $H_m^{(1)}(\zeta r)$ and $H_m^{(2)}(\zeta r)$ by $e^{-i\zeta r_m}$ and $e^{i\zeta r_m}$ (where r_m is the mean radius of the layer), respectively, tranforms the exponent terms in equation (2.42) to $e^{\pm i\zeta|r-r_m|}$. Since these multipliers are constant for each layer, they can then be absorbed in the arbritary constants of the layer.

2.6 Numerical Results and Discussion

In this section, eight numerical examples for dispersion characteristics of homogeneous and laminated cylinders are presented:

1. A homogeneous elastic rod.
2. A two-layered isotropic hollow cylinder.
3. A homogeneous elastic isotropic cylinder with the Poisson's ratio ν of 0.3, H/R of 1.5, and circumferential wavenumbers, m, of 1 and 3.
4. A 4 ply $[+30/-30]_s$ graphite/epoxy with H/R of 0.667 and circumferential wavenumbers, m, of 1 and 3.

5. A 4 ply $[+15/-15]_s$ graphite/epoxy cylinder, $H/R = 0.667$, and circumferential wavenumber, m, of 1 and 3.

6. A 4 ply $[+15/-15]_s$ graphite/epoxy cylinder, $H/R = 0.10$, and circumferential wavenumbers, m, of 1 and 3.

7. A 16 ply $[+15/-15]_s$ graphite/epoxy cylinder, $H/R = 0.10$, and a circumferential wavenumber, m, of 1.

8. A 12 ply $[0_2/+45/-45/0_2]_s$ graphite/epoxy cylinder, $H/R = 0.10$, and a circumferential wavenumber, m, of 1.

The first two examples are to illustrate the applicability and the efficiency of the propagator matrix mehod. The wave propagation and modal behaviors of the two-layered isotropic cylinder are investigated in the second example. The accuracy of the results obtained by the Rayleigh-Ritz type approximations tested against the analytical solutions is illustrated in the third example. The effect of circumferential wavenumber on the dispersion characteristics of isotropic cylinder is also investigated. The last five examples compare the accuracy of the results obtained from the two Rayleigh-Ritz type approximations for laminated composite cylinders. The factors effecting the dispersion characteristics of laminated composite cylinders are also investigated in detail.

When the laminated composite cylinder is considered, it is assumed that the wavelength is much larger than the fibre diameter and spacing between the fibres. Each layer or lamina can therefore be modelled as a transversely isotropic medium with the symmetry axis aligned with the fibre direction (Datta *et al.* 1984). For the laminated composite cylinders considered in all examples, the elastic properties for each ply relative to their natural elastic axes are (Huang and Dong 1984):

$$\begin{aligned} &E_L = 13.9274 \times 10^{10} N/m^2, \quad E_T = 1.5169 \times 10^{10} N/m^2; \\ &G_{LT} = G_{TT} = 0.5861 \times 10^{10} N/m^2, \quad \nu_{LT} = \nu_{TT} = 0.21, \end{aligned} \tag{2.43}$$

where E and G denote modulus of elasticity and shear modulus, respectively. ν is the Poisson's ratio. Subscripts L and T represent the fibre and the transverse directions, respectively. In all numerical results presented in this chapter, the frequency and wavenumber, whenever referred, are the normalized frequency Ω and normalized wavenumber γ with the forms of:

$$\Omega = \frac{\omega}{\omega_{ref}} \quad ; \quad \gamma = \frac{\xi}{\xi_{ref}}, \tag{2.44}$$

where ω_{ref} and ξ_{ref} are the reference frequency and the reference wavenumber, respectively. For simplicity, all sublayers in cylinder are modelled with equal thicknesses.

2.6.1 Efficacy of the Propagator Matrix Approach

The applicability, the accuracy, and the efficiency of the propagator matrix method are illustrated by the following two numerical examples. The wave propagation and modal behaviors of the two-layered isotopic cylinder are also investigated.

Example 1

The axisymmetric vibration of the harmonic waves in a solid rod with Poisson's ratio of 0.31 is considered. The frequency spectrum is shown in Figure 2.2. The reference frequency and reference wave number are, respectively;

$$\omega_{ref} = \frac{\delta v_s}{H} \quad ; \quad \xi_{ref} = \frac{\delta}{H},$$

where δ is the lowest nonzero root of $J_1(\delta) = 0$, v_s is the shear wave velocity and H is the total thickness of the rod. The dashed lines show the complex branches and the circles represent the results given by Onoe *et al.* (1962). By stipulating the axially symmetric vibration, the longitudinal and torsional modes are uncoupled. Only the longitudinal modes are illustrated herein. Onoe *et al.* presented the spectrum showing purely real, imaginary and complex branches in which the complex branches were sketched approximately, except those near the coordinate planes. As seen in Figure 2.2, the discrepancy

between the results from the present method and the approximate results presented by Onoe *et al.* is pronounced for these complex branches except for those near the planes. For the purely real and imaginary branches, the two results are in excellent agreement. This confirms the applicability and the accuracy of the method.

Example 2

The vibration of harmonic waves in an infinite composite cylinder is considered. The cylinder is composed of two isotropic layers perfectly bonded together. The mechanical properties of the two layers are: $\nu_1 = \nu_2 = 0.30$; where ν denotes the Poisson's ratio; $\mu_1/\mu_2 = 1; \rho_1/\rho_2 = 2$; $h_1/h_2 = 1$. The subscripts 1 and 2 represent the inner and outer layer, respectively. The ratio of the thickness to the mean radius of the outer layer, h_2/R_2, is 0.20. The circumferential wave number, m, is 1. The reference frequency and the reference wavenumber are, respectively:

$$\omega_{ref} = \frac{2\pi v_{s2}}{H} \quad ; \quad \xi_{ref} = \frac{2\pi}{H},$$

where v_{s2} is the shear wave velocity in the outer layer.

Armenàkas (1971) presented the results for the propagating modes (shown as circles in Figure 2.3). It can be seen that the results from the present method and those obtained by Armenàkas are in excellent agreement. The spectrum of this cylinder showing real, imaginary and complex branches is presented in Figure 2.4.

It can be noticed that the propagator matrix method does not require any change in the computer codes in order to accommodate more layers of different material properties. Unlike the stiffness method proposed by Moore (1990), the propagator matrix approach requires the computation of only 4×4 (for rod problems) or 6×6 matrix (for hollow cylinder cases). Since the formulation is based upon the three-dimensional theory of elasticity, the roots are exact. To the best of the author's knowledge, the exact complex frequency spectrum of laminated isotropic cylinder has not yet been reported.

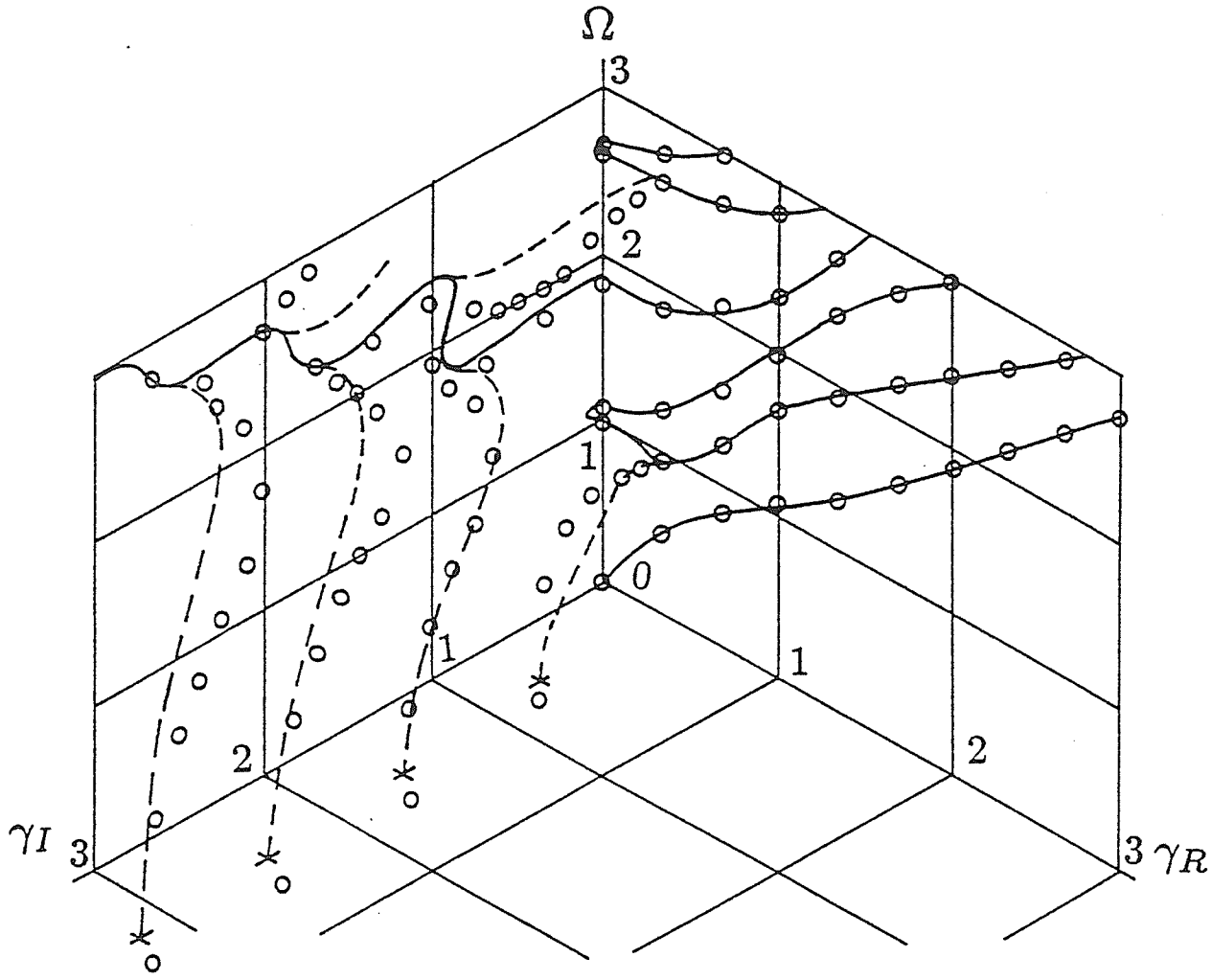

Figure 2.2: Complex frequency spectrum of isotropic rod with $\nu = 0.31$.

(— present study; ○ Onoe *et al.* 1962)

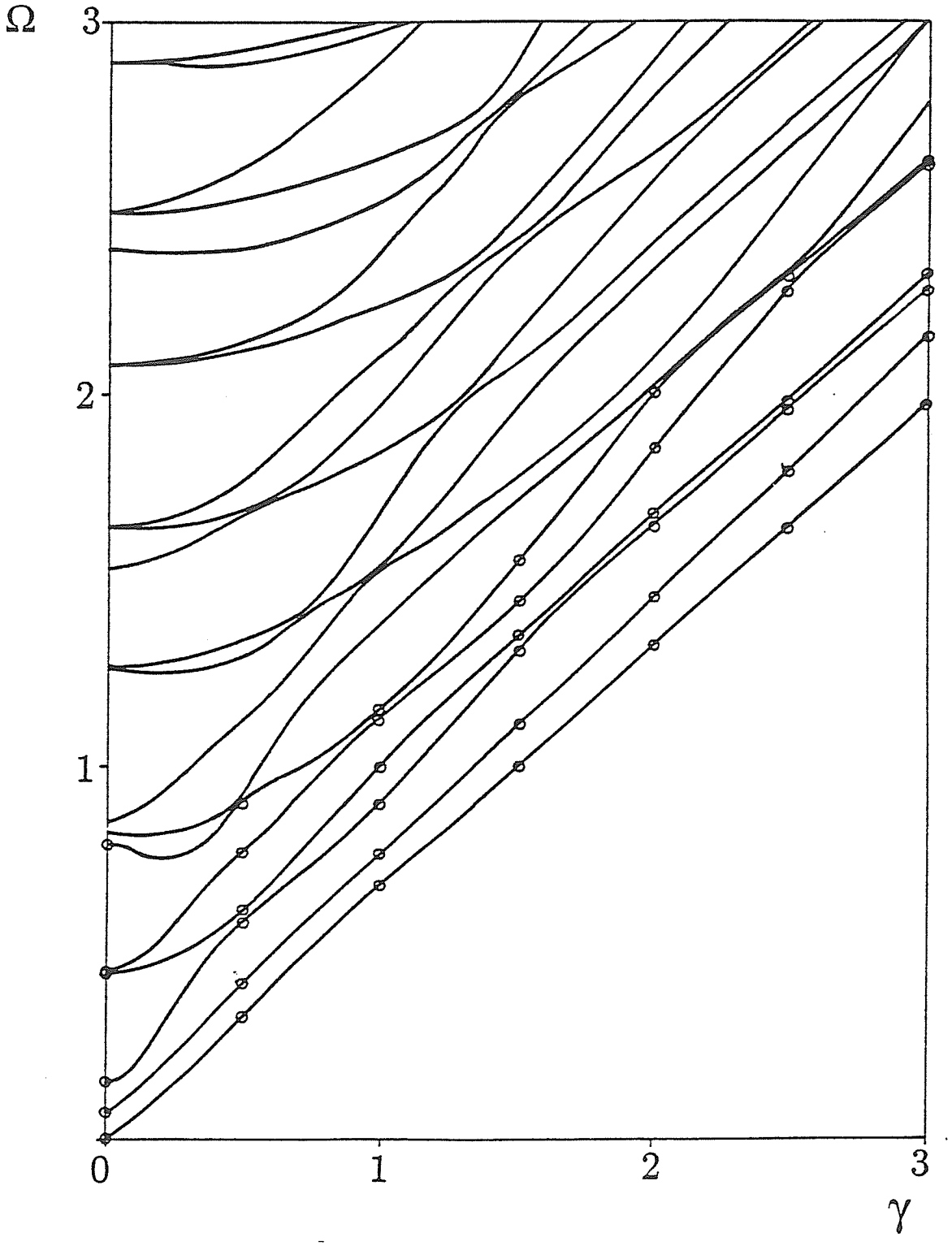

Figure 2.3: Frequency spectrum of two-layered isotropic cylinder

(— present study; ○ Armenàkas, 1971)

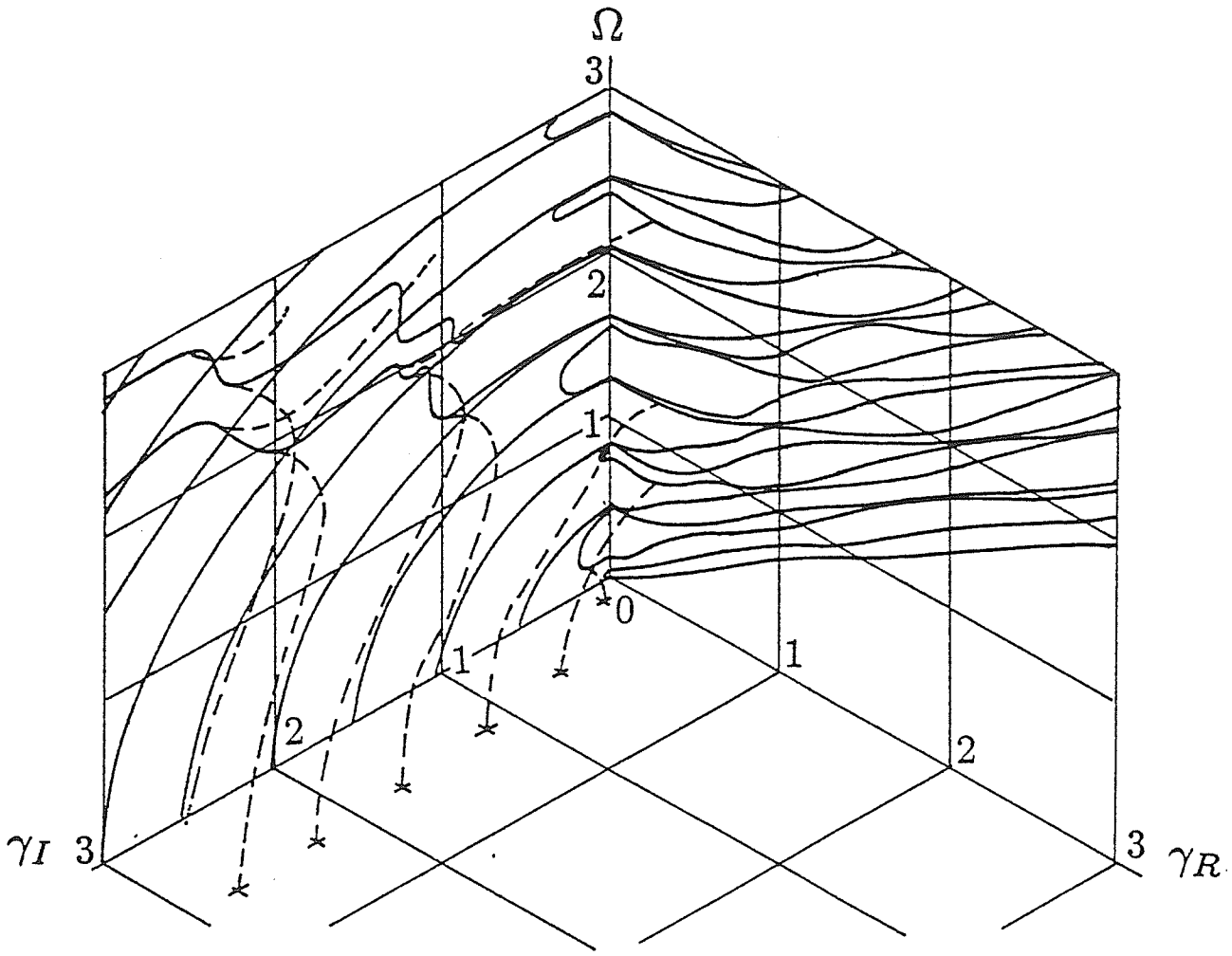

Figure 2.4: Complex frequency spectrum of two-Layered isotropic cylinder.

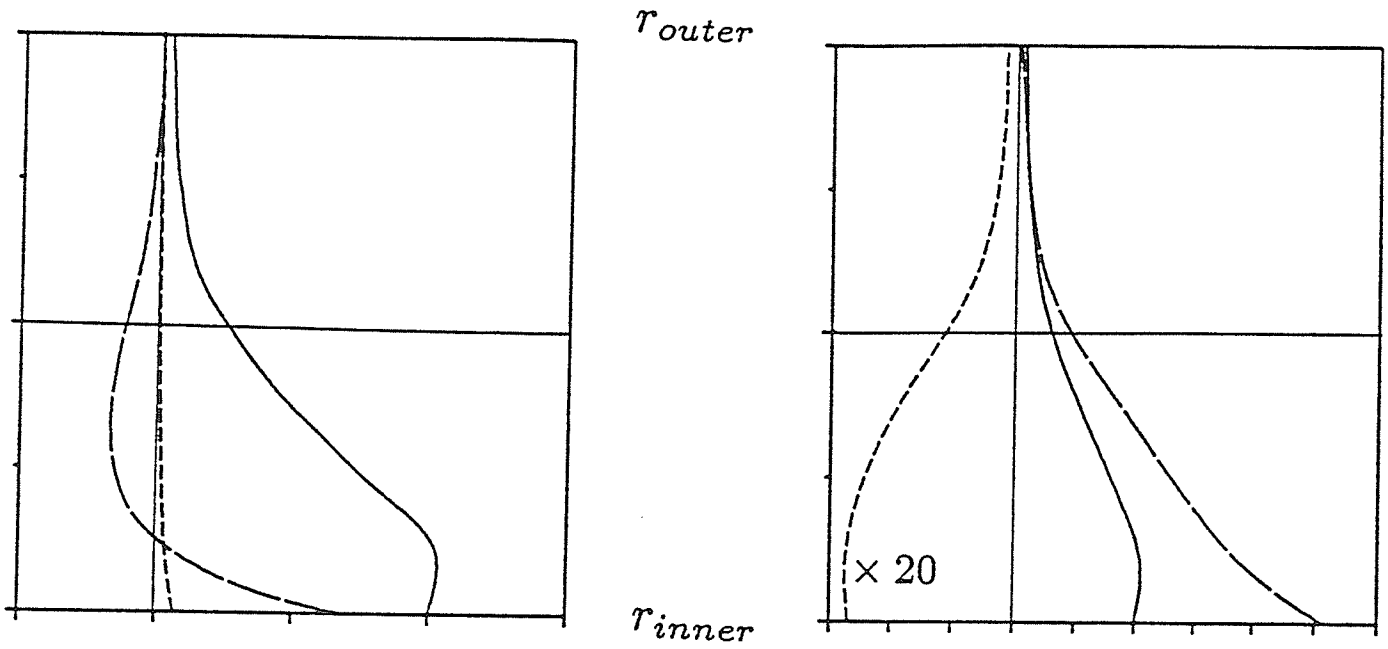

(a) $\gamma = 1.4955$ (b) $\gamma = 1.3376$

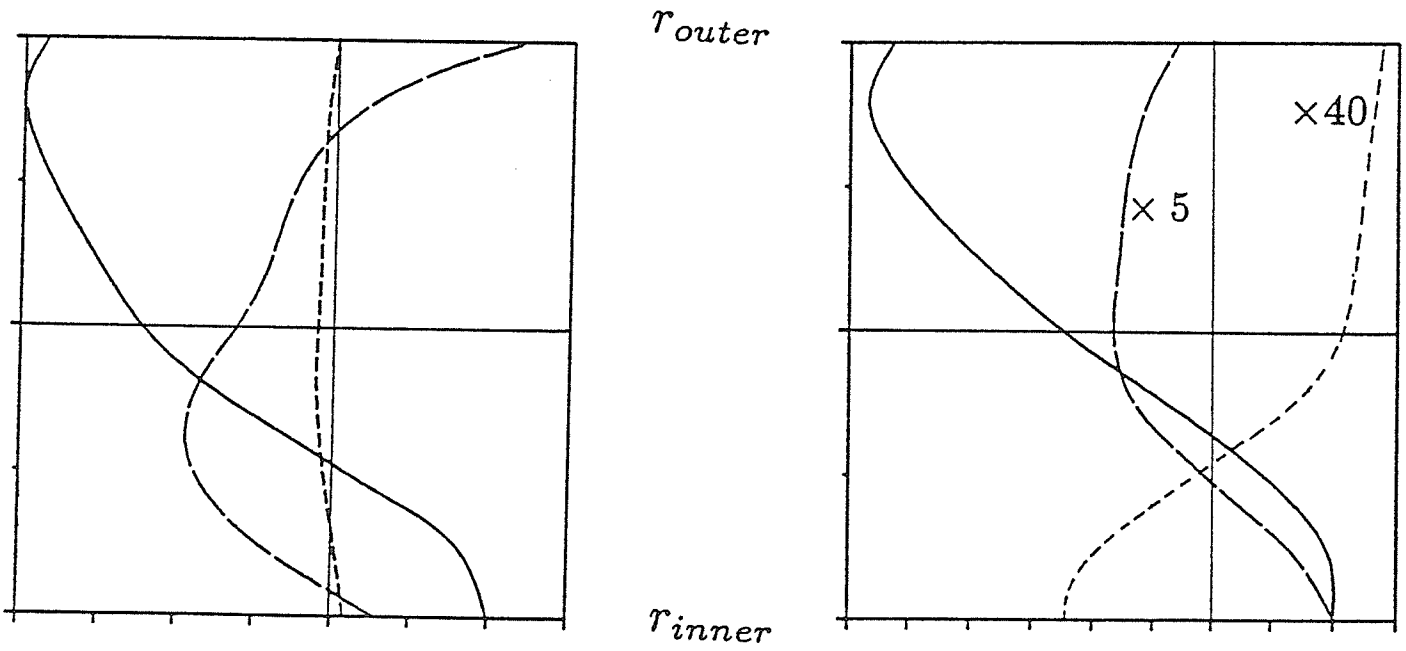

(c) $\gamma = 1.1116$ (d) $\gamma = 0.9943$

Figure 2.5: Displacement distribution for propagating modes at normalized frequency Ω of 1.0 (— u, - - - v, – – w).

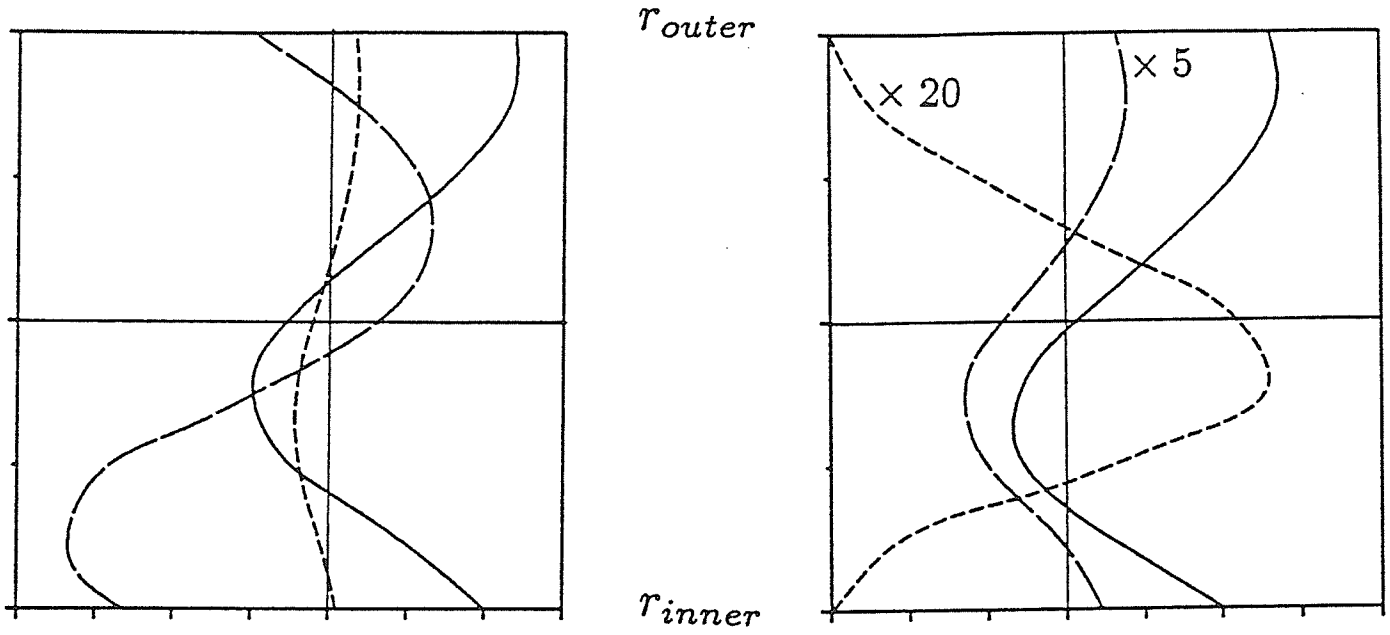

(e) $\gamma = 0.8026$ (f) $\gamma = 0.7149$

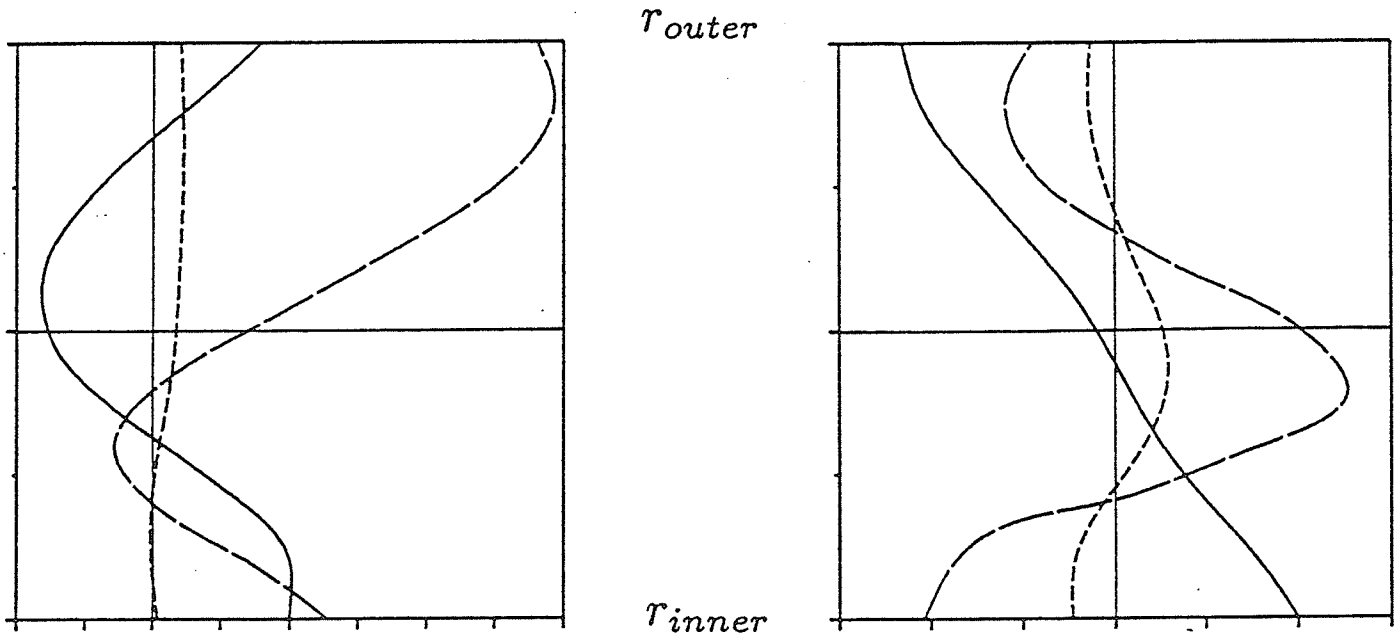

(g) $\gamma = 0.5557$ (h) $\gamma = 0.3133$

Figure 2.5: Displacement distribution for propagating modes at normalized frequency Ω of 1.0 (— u, - - - v, – – w).

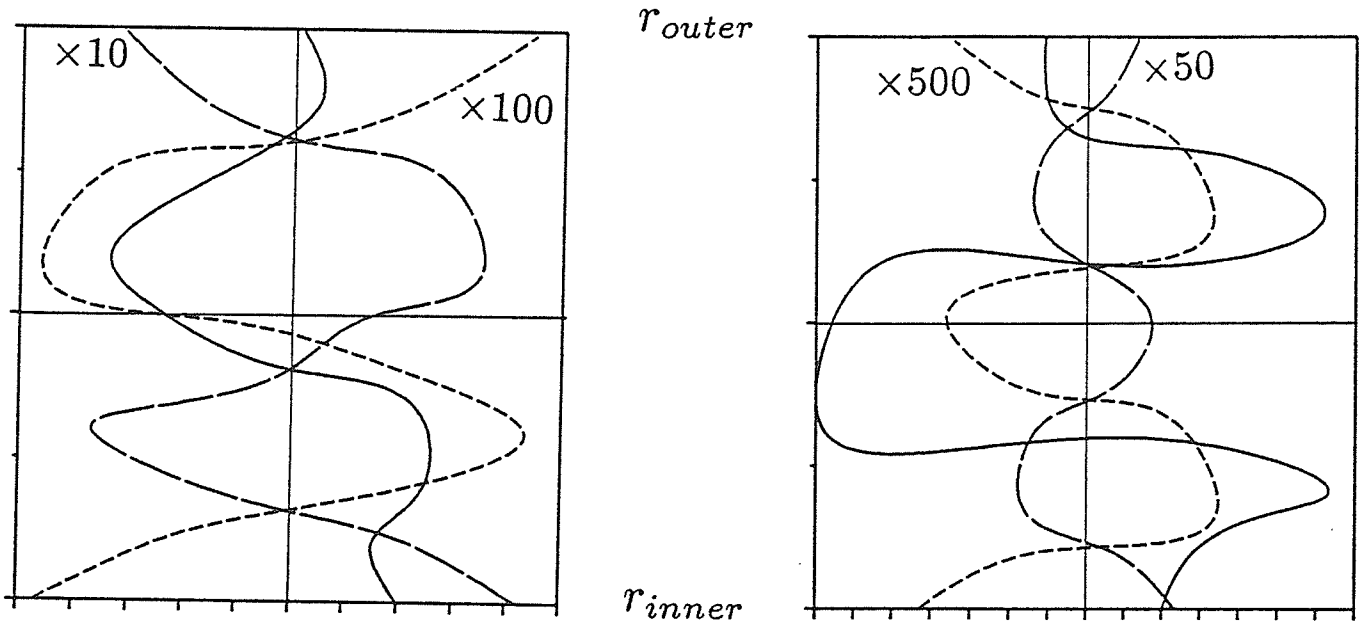

(a) $\gamma = 0.9138i$ (b) $\gamma = 1.5847i$

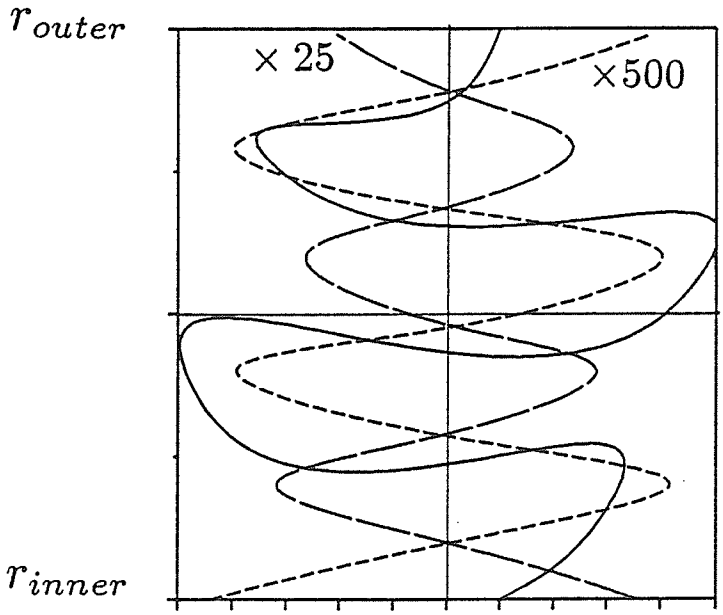

(c) $\gamma = 2.1905i$

Figure 2.6: Displacement distribution for non-propagating modes at normalized frequency Ω of 1.0 (— u, - - - v, – – w).

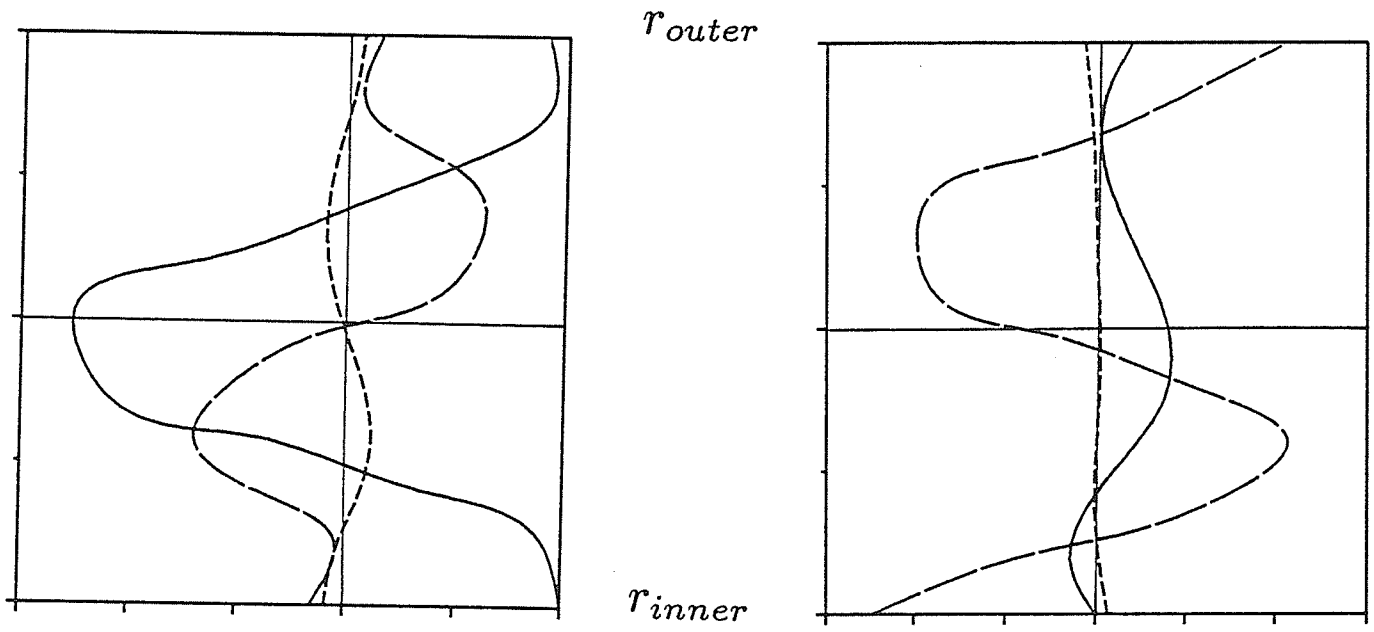

(a) Real part

(b) Imaginary part

Figure 2.7: Displacement distribution for evanescent modes at Ω of 1.0 and γ of $0.4392 - 0.6837i$ (— u, - - - v, – – w).

Figure 2.5 shows the displacement distribution through the thickness of the cylinder for normalized frequency, $\Omega = 1.0$. Figures 2.5a, 2.5c, 2.5e and 2.5g show that the torsional motion is insignificant for the first, third, fifth and seventh propagating modes. The radial and axial motions are coupled for these modes. The radial motion predominates for the first and the third propagating modes (Figures 2.5a and 2.5c), whereas for the fifth and the seventh propagating modes the axial motion is predominant (Figures 2.5e and 2.5g). The presence of the torsional motion becomes paramount in the second, fourth, and sixth propagating modes (Figures 2.5b, 2.5d, and 2.5f, respectively). Figure 2.5h reveals that all motion is coupled in the eighth propagating mode. Armenàkas (1971) commented that the motion is concentrated in the inner layer. This is true for the first and the second propagating modes, however, for the third and the fourth propagating modes the motion is stronger in the outer layer.

One interesting characteristic of guided waves in the cylinder for the flexural case ($m = 1$) is that some of the branches in the imaginary plane extend to zero frequency. The behavior of these branches (Figure 2.4) is similar to that of the axisymmetric torsional case (Mason, 1968). The investigation of the mode shapes of these non-propagating modes (Figure 2.6) for $\Omega = 1$ reveals that the torsional motion predominates over the radial and axial motions. On the other hand, for evanescent mode, the torsional motion is negligible as seen in Figure 2.7 for $\Omega = 1$.

2.6.2 Accuracy of Rayleigh-Ritz Type Approximations

Example 3

The accuracy of the results obtained by the Rayleigh-Ritz type approximations is tested against the analytical solution for propagation in a homogeneous cylinder with different circumferential wavenumbers. The propagation of waves in homogeneous isotropic

cylinder with the Poisson's ratio ν of 0.3 and the thickness to radius ratio, H/R, of 1.5 is considered in this example. Two circumferential wavenumbers m, which are 1 and 3, are considered. The reference frequency and the reference wavenumber are defined, respectively, as:

$$\omega_{ref} = \frac{\pi v_s}{H}, \quad \gamma_{ref} = \frac{\pi}{H}.$$

Figures 2.8 show the frequency spectrum for these examples. The Rayleigh-Ritz type approximations, the displacement continuity method (dashed lines) and the stress continuity (solid lines), yield excellent results in comparison with the analytical solutions (circles) in the low frequency regimes. However, for higher modes, the discrepancy between the two approximate methods becomes noticeable. It can be observed that the results obtained from the stress continuity are lower than those obtained by the displacement continuity approach. Since both of the approximations employ the consistent mass approach, the stress continuity will generate the results closer to the analytical solutions.

Armenàkas *et al.* (1969) illustrated that the effect of the variation in circumferential wavenumber on dispersion behavior of thin-walled isotropic cylinder is considerably negligible. For thick-walled cylinders, an inspection of Figures 2.8 reveals that the change in circumferential wavenumber is quite pronounced only in low wavenumber regimes (Braga *et al.*, 1990). A thorough investigation of thick cylinders shows that the rigid body motion does not appear when the circumferential wavenumber is 3. The variation in circumferential wavenumber, however, does not affect the accuracy of the results obtained by the approximate methods.

2.6.3 Factors Effecting the Dispersion Characteristics of Laminated Composite Cylinders

Examples 4-8

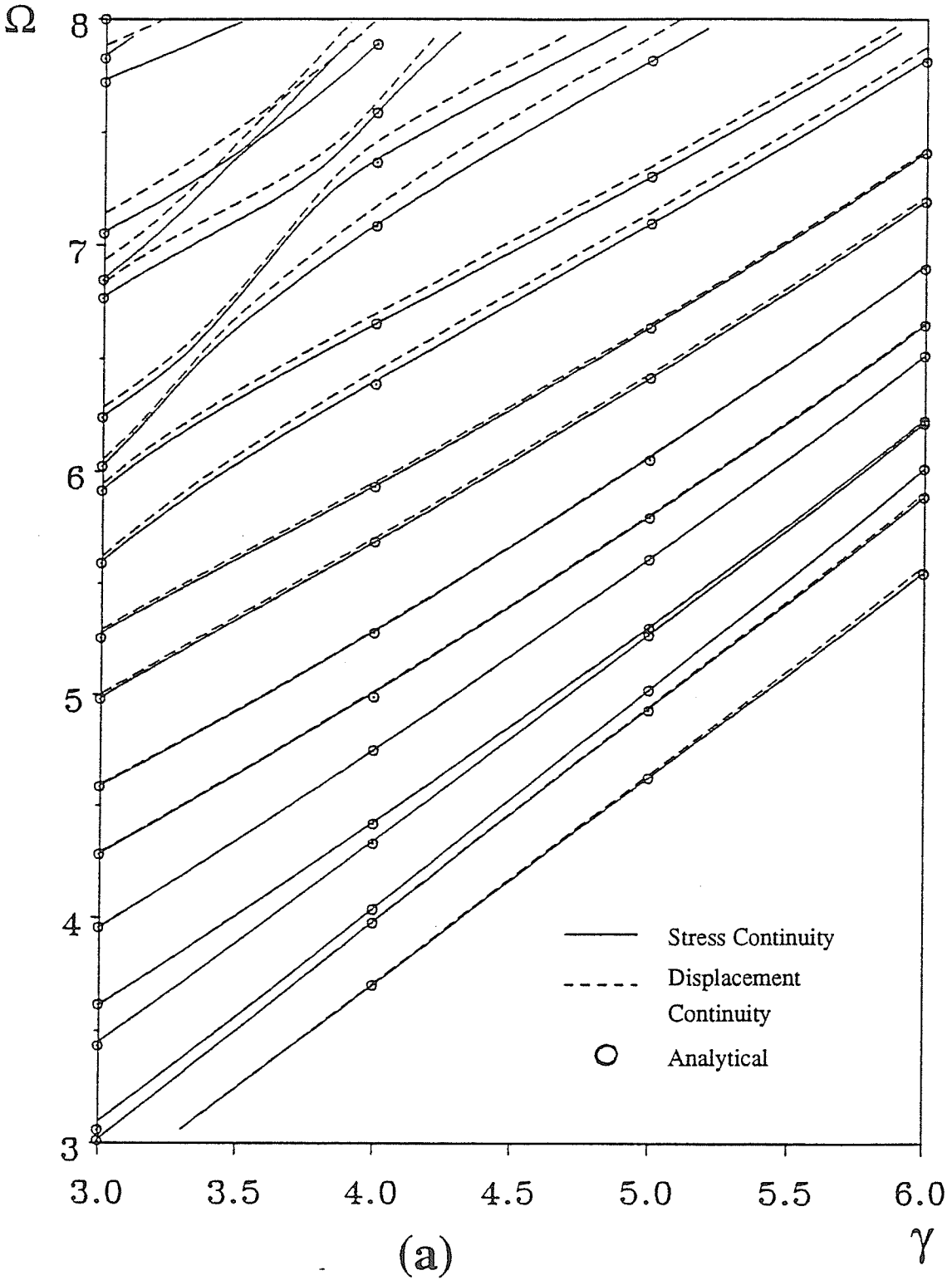

Figure 2.8: Frequency spectrum for a homogeneous isotropic cylinder with $\nu = 0.3$, $H/R = 1.5$, and (a) $m = 1$, (b) $m = 3$.

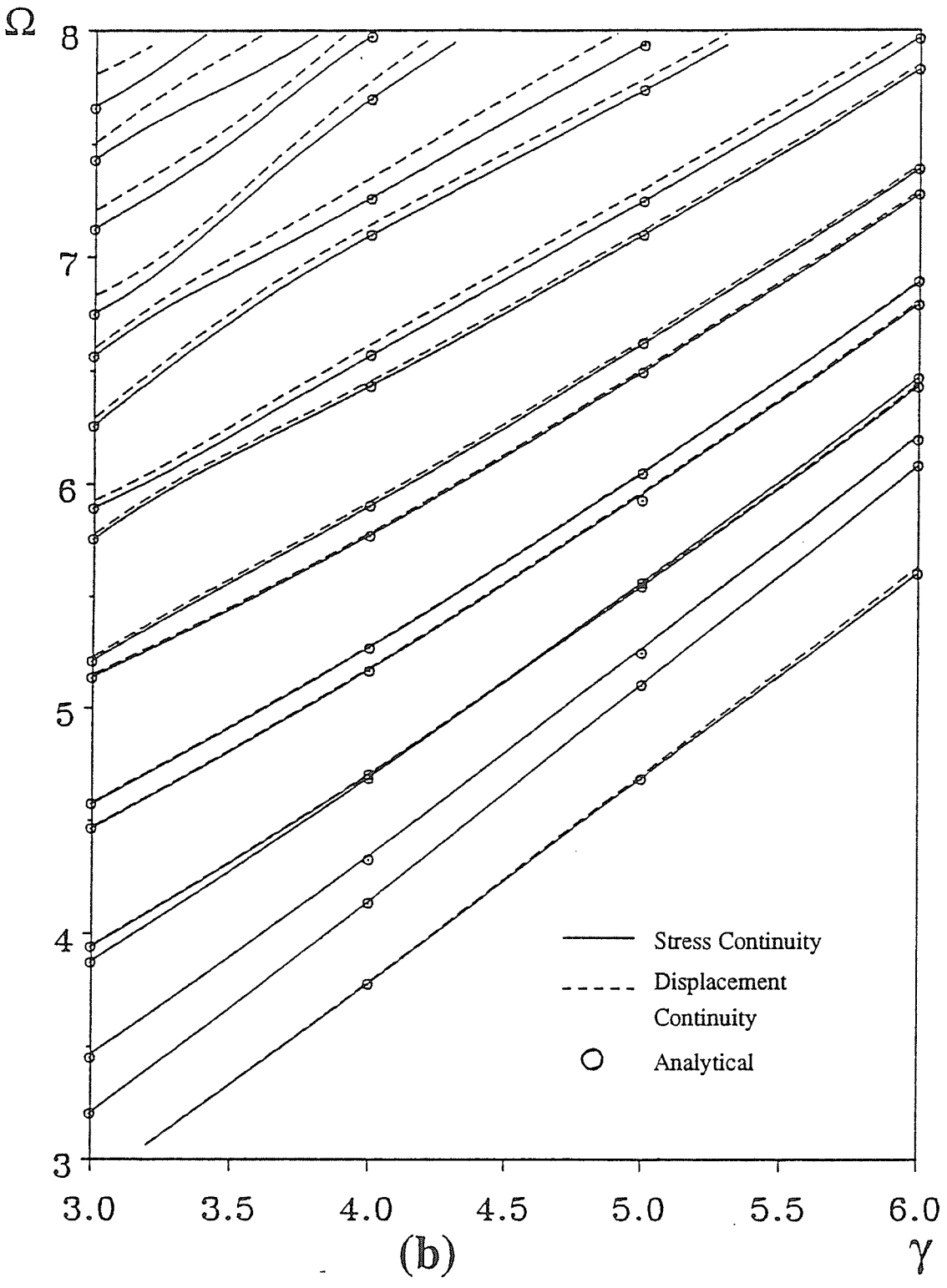

Figure 2.8: Frequency spectrum for a homogeneous isotropic cylinder with $\nu = 0.3$, $H/R = 1.5$, and (a) $m = 1$, (b) $m = 3$.

The last five examples are considered in an investigation of the factors effecting the dispersion characteristics of laminated composite cylinders. Attention will be focussed mainly on the dominant branches, which are real branches of the frequency spectrum. The reference frequency and the reference wavenumber are, respectively:

$$\omega_{ref} = \frac{v_L}{H} \quad ; \quad \xi_{ref} = \frac{\pi}{H},$$

where

$$v_L^2 = \frac{E_L}{\rho}.$$

Figures 2.9 to 2.13 illustrate the frequency spectrum for the cylinders in examples 4 to 8, respectively.

a) The Effect of Circumferential Wavenumber

The variation in the circumferential wavenumber has a similar effect on the dispersion characteristics of a laminated composite cylinder as on those of a homogeneous cylinder. The effects are mostly concentrated in the low wavenumber regions. The comparison of Figures 2.9a to 2.9b and 2.10a to 2.10b for examples 4 and 5, respectively, reveals that there is no rigid body motion for the circumferential wavenumber of 3. The process of wave velocity reaching the constant phase velocity stage is also slow-down with the higher circumferential wavenumber. For relatively thin tube, Figures 2.11 for example 6, the change in the circumferential wavenumber from 1 to 3 does not significantly alter the dispersion characteristics of the cylinder.

b) The Effect of Thickness to Mean Radius Ratio

Figures 2.10 and 2.11 for examples 5 and 6, respectively, illustrate the influence of the H/R ratio on the dispersion characteristics of laminated composite cylinder. It should be noted that the higher the H/R ratio, the thicker the cylinder. With the circumferential

wavenumber of 1, the variation in H/R ratio shows no significant influence on the dispersion behavior. The effect of H/R ratio becomes more pronounced for the circumferential wavenumber of 3. It is noticed that the change in H/R ratio does affect the values of the cut-off frequencies, i.e. the frequencies for zero wavenumber, in low frequency regimes and the degree of weak coupling. The corresponding dispersion curves of a thin cylinder have the typical configuration of *weak coupling*, namely, they come close together near the region of intersection or contact of the dispersion curves (Armenàkas *et al.* 1969). The comparison of Figures 2.10a and 2.11a, and 2.10b and 2.11b demonstrates that the thinner the cylinder, the higher the degree of weak coupling phenomenon. The effects, however, are localized in the region of low wavenumbers.

c) The Effect of Layering and Ansiotropy

Layering herein means the number of laminae in the laminated composite cylinder. Figures 2.11a and 2.12 for examples 6 and 7, respectively, show that the effect of layering is very significant. Layering has a tendency of increasing phase velocities for high modes. It is very interesting that for the sixteen ply of graphite/epoxy, the discrepancy of the results obtained from both approximate methods become less in comparison to that for the four ply cylinders.

When laminated composite cylinder is composed of many different orientations of the lamina, the cylinder is considered to have high degrees of anisotropy. Figure 2.13 illustrates the frequency spectrum of a multi-angle symmetric laminated cylinder used in the aerospace industry. It can be observed from Figure 2.13 for example 8 that the wave velocities approach the constant phase velocity stage slower than in $[+15/-15]_s$ or $[+30/-30]_s$ ply lay up tube. In comparing the frequency spectrum of the 12 ply $[0_2/+45/-45/0_2]_s$ graphite/epoxy cylinder (Figure 2.13) with that of the 16 ply $[+15/-15]_s$ cylinder (Figure 2.12) it can be noticed that both spectra have a similar pattern, especially in the region of small wavenumber, ξ. The cut-off frequencies as well as the

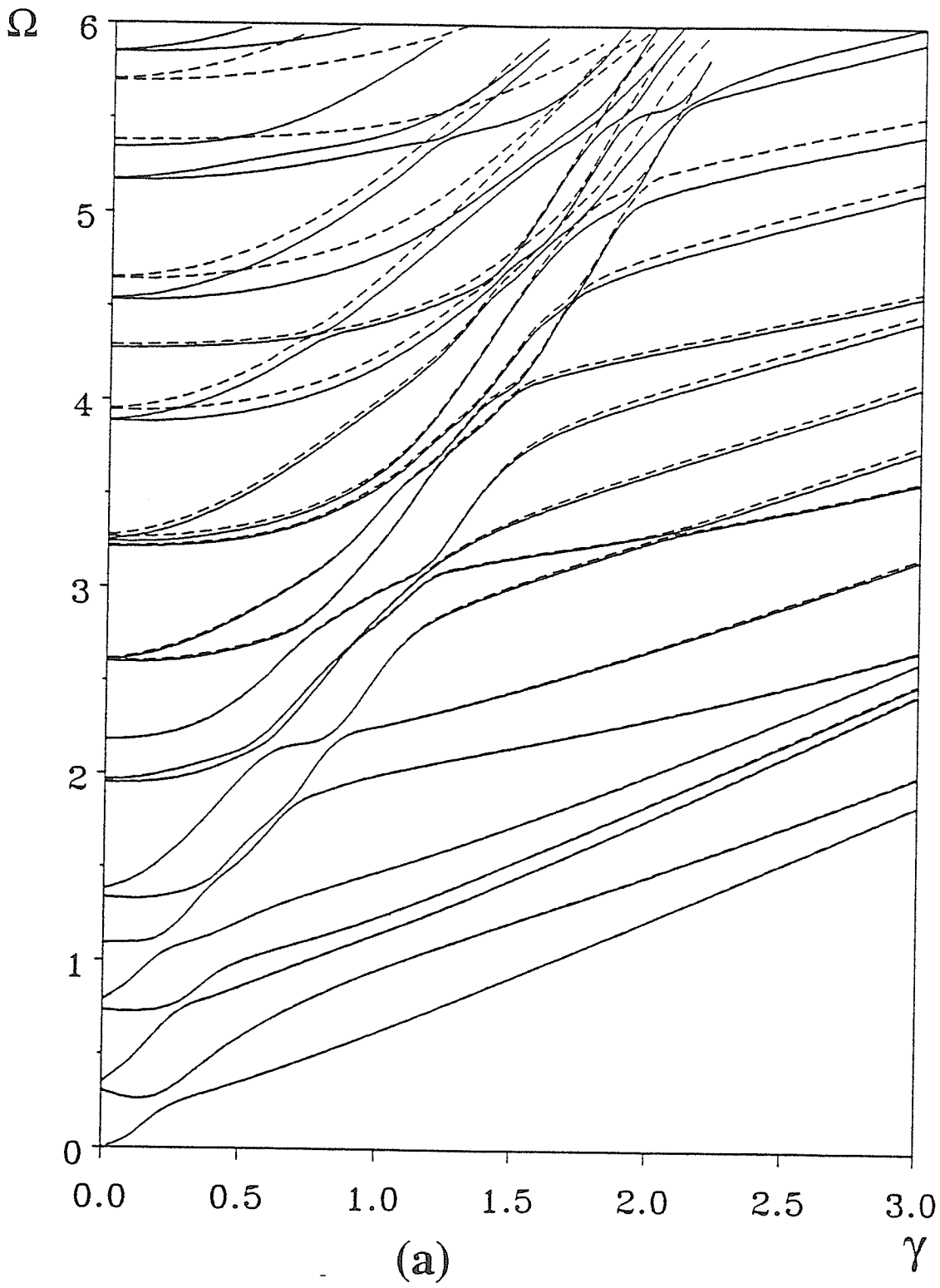

Figure 2.9: Frequency spectrum for a 4 ply $[+30/-30]_s$ graphite/epoxy cylinder with $H/R = 0.667$, and (a) $m = 1$, (b) $m = 3$.

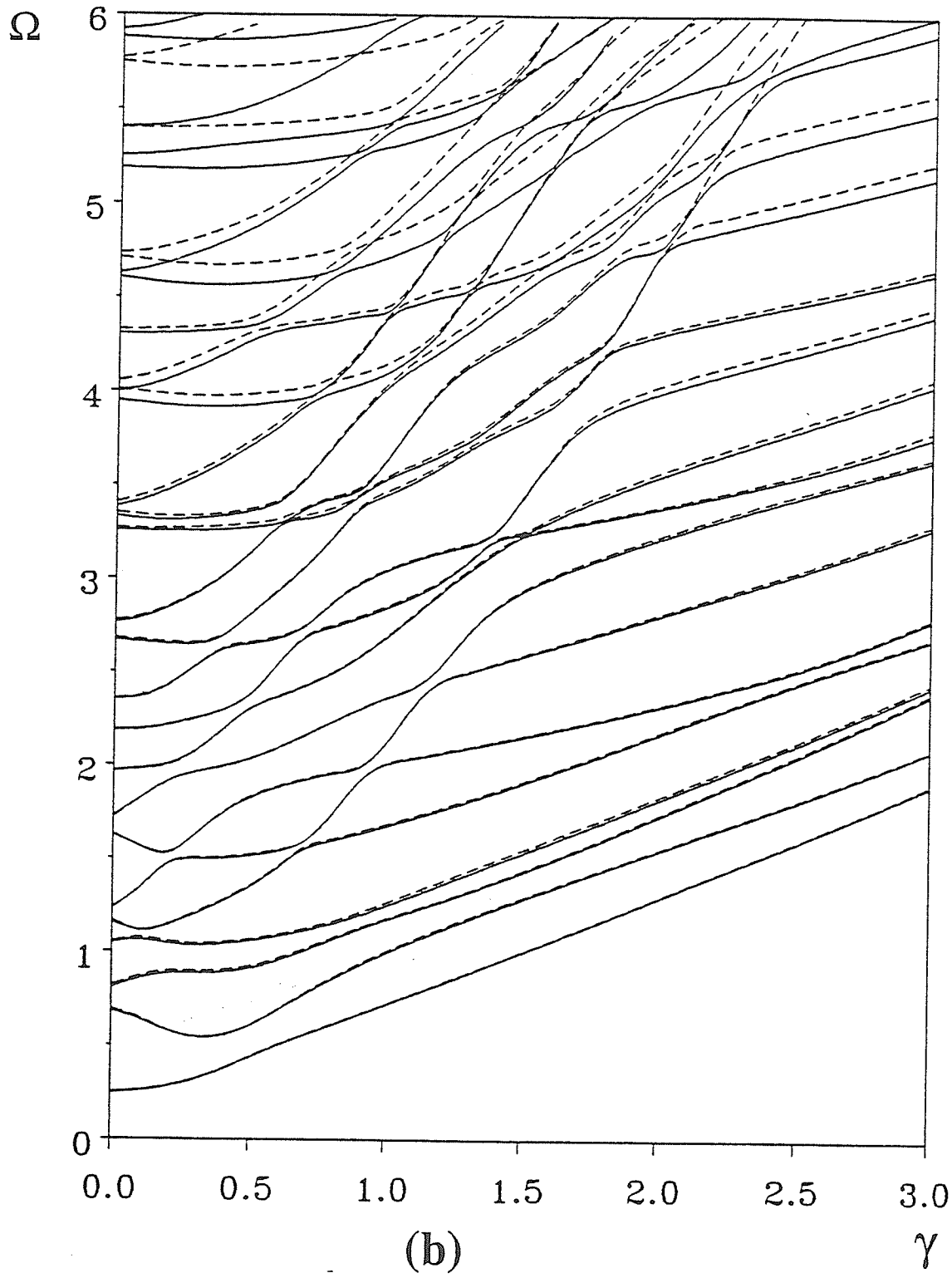

Figure 2.9: Frequency spectrum for a 4 ply $[+30/-30]_s$ graphite/epoxy cylinder with $H/R = 0.667$, and (a) $m = 1$, (b) $m = 3$.

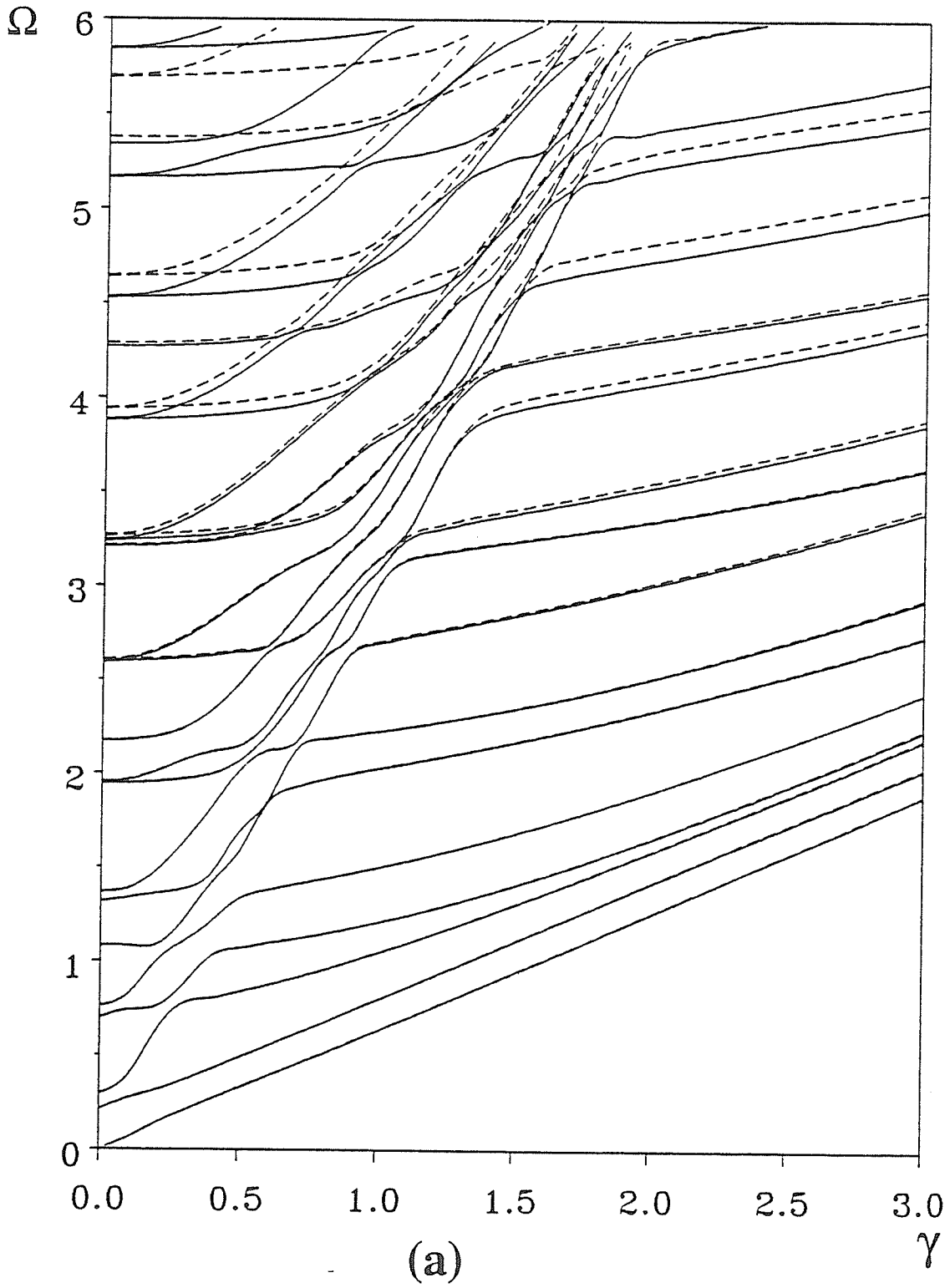

Figure 2.10: Frequency spectrum for a 4 ply $[+15/-15]_s$ graphite/epoxy cylinder with $H/R = 0.667$, and (a) $m = 1$, (b) $m = 3$.

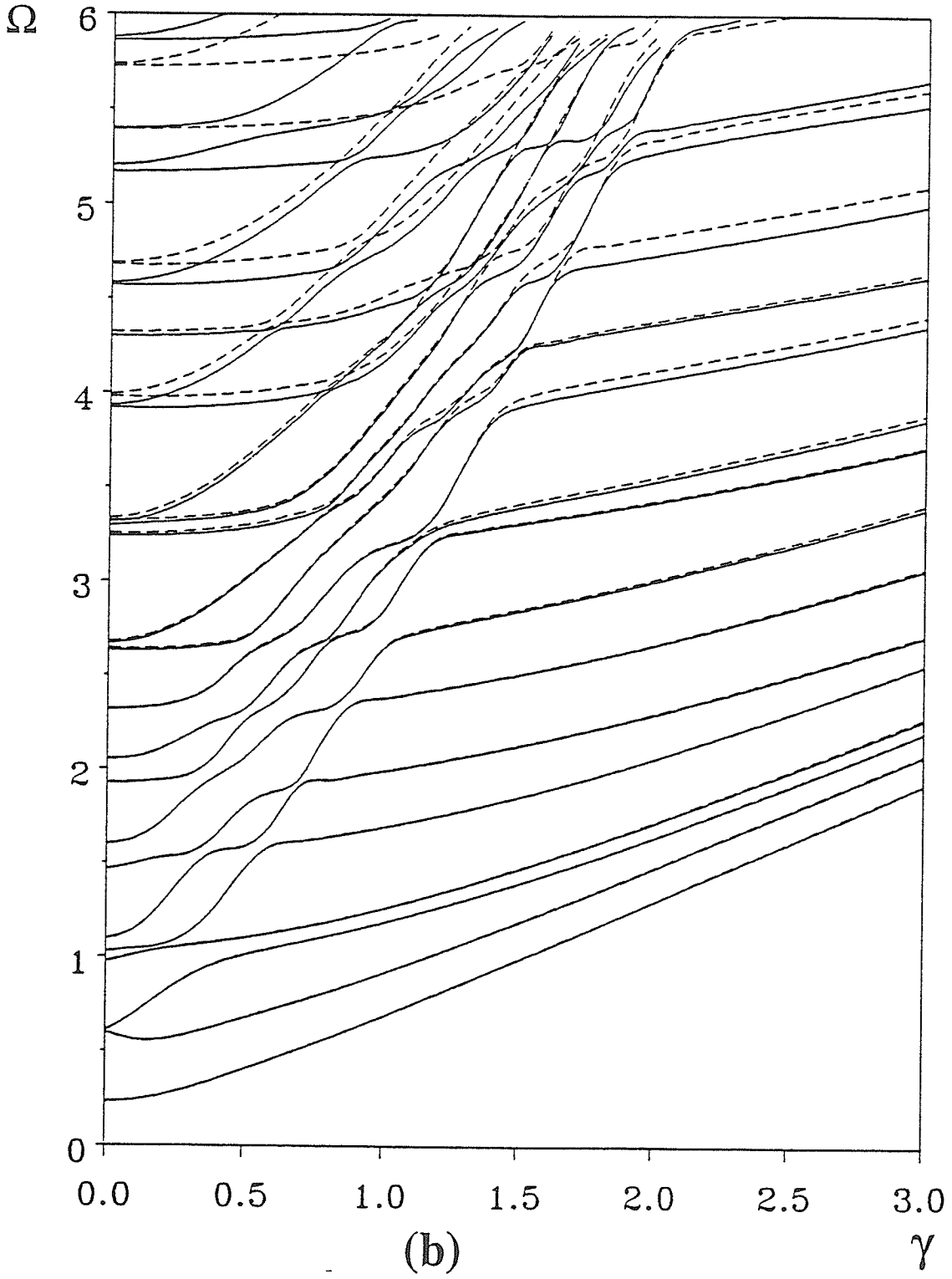

Figure 2.10: Frequency spectrum for a 4 ply $[+15/-15]_s$ graphite/epoxy cylinder with $H/R = 0.667$, and (a) $m = 1$, (b) $m = 3$.

first propagating mode for both cylinders are almost identical.

2.7 Concluding Remarks

The elastic wave propagation in isotropic and laminated cylinders is investigated by the propagator matrix method and the Rayleigh-Ritz type approximations. The propagator matrix is established from the relation of the stresses and displacements between the two interfaces of the sublayer based upon the three-dimensional theory of elasticity for isotropic materials. The dispersion relation of the cylinder is generated from this relation. The Rayleigh-Ritz type approximations are employed to investigate the dispersion characteristics for laminated composite cylinders when the analytical solution is unattainable. The methods divide the cylinder into several sublayers and approximate the displacement distribution through the thickness of the sublayers by interpolation functions in terms of discrete generalized coordinates. These generalized coordinates may involve only displacements or both displacements and stresses at the nodal points. The dispersion relations of the cylinder obtained by Rayleigh-Ritz type approximations are in the forms of eigenvalue problem. It is shown that the dispersion behavior predicted by the Rayleigh-Ritz type approximations agree well with the analytical solution. It may be noted that although the stress continuity method yields more accurate results than those obtained by the displacement continuity approach, the discrepancy of the results from the two methods is considerably small. Observation made here further suggest that the displacement continuity method can be exploited in solving the wave scattering problems.

The results illustrate that the measurable changes in phase velocity are caused by the variation of circumferential wavenumber, the thickness to radius ratio, the layering, and the degree of anisotropy. Most of the effects, however, are quite appreciable at low frequencies and low wavenumber regime.

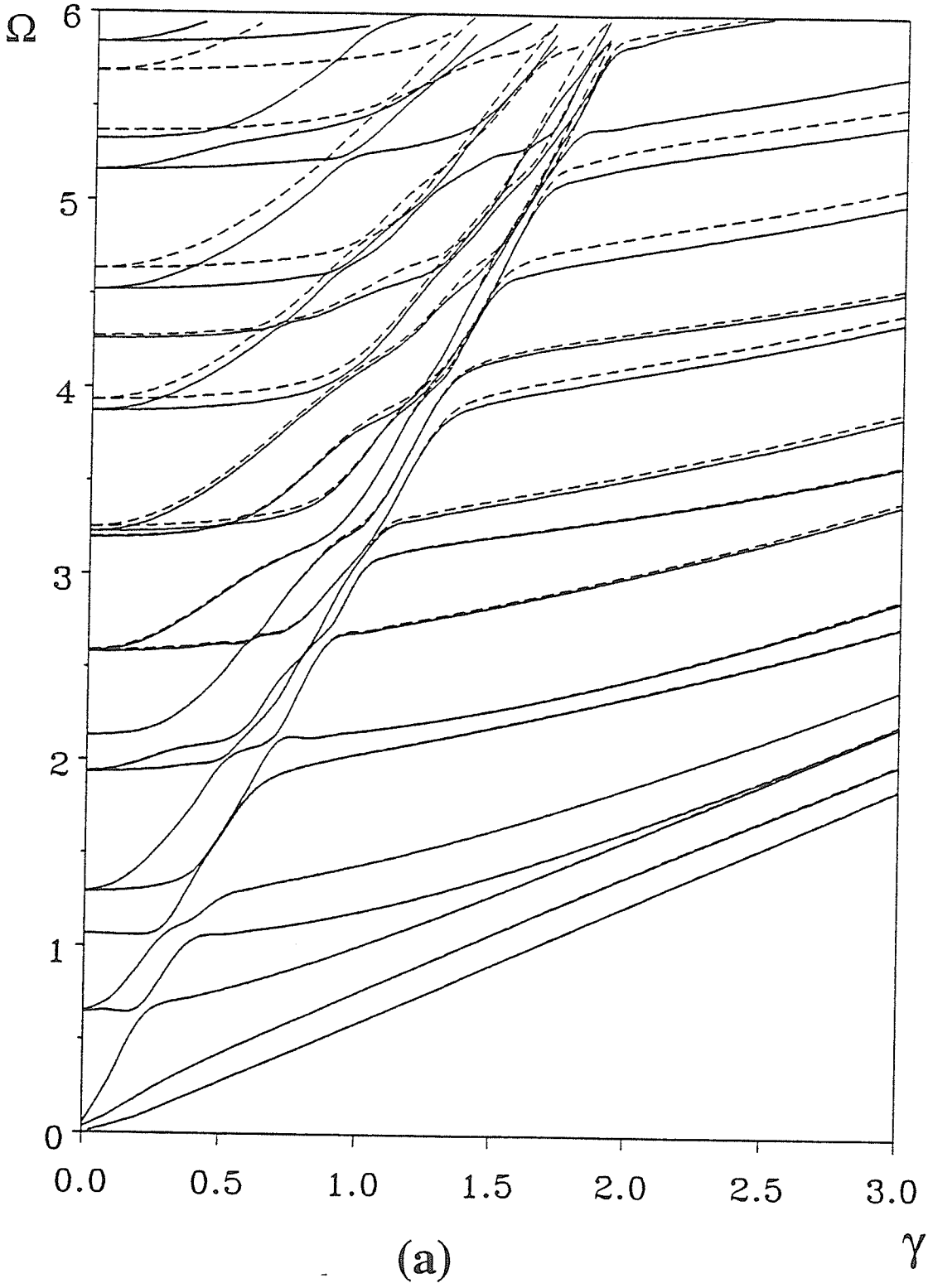

Figure 2.11: Frequency spectrum for a 4 ply $[+15/-15]_s$ graphite/epoxy cylinder with $H/R = 0.10$, and (a) $m = 1$, (b) $m = 3$.

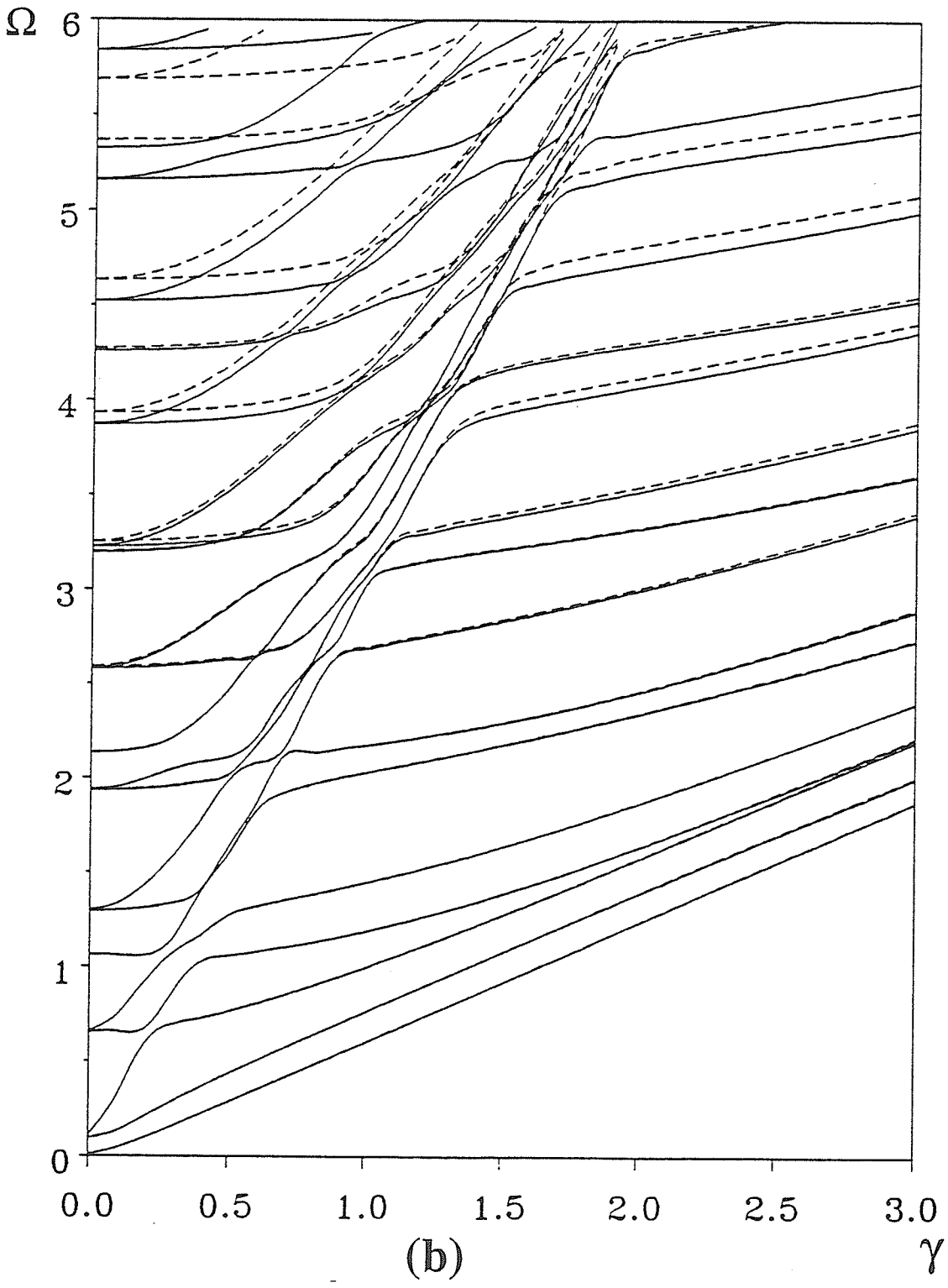

Figure 2.11: Frequency spectrum for a 4 ply $[+15/-15]_s$ graphite/epoxy cylinder with $H/R = 0.10$, and (a) $m = 1$, (b) $m = 3$.

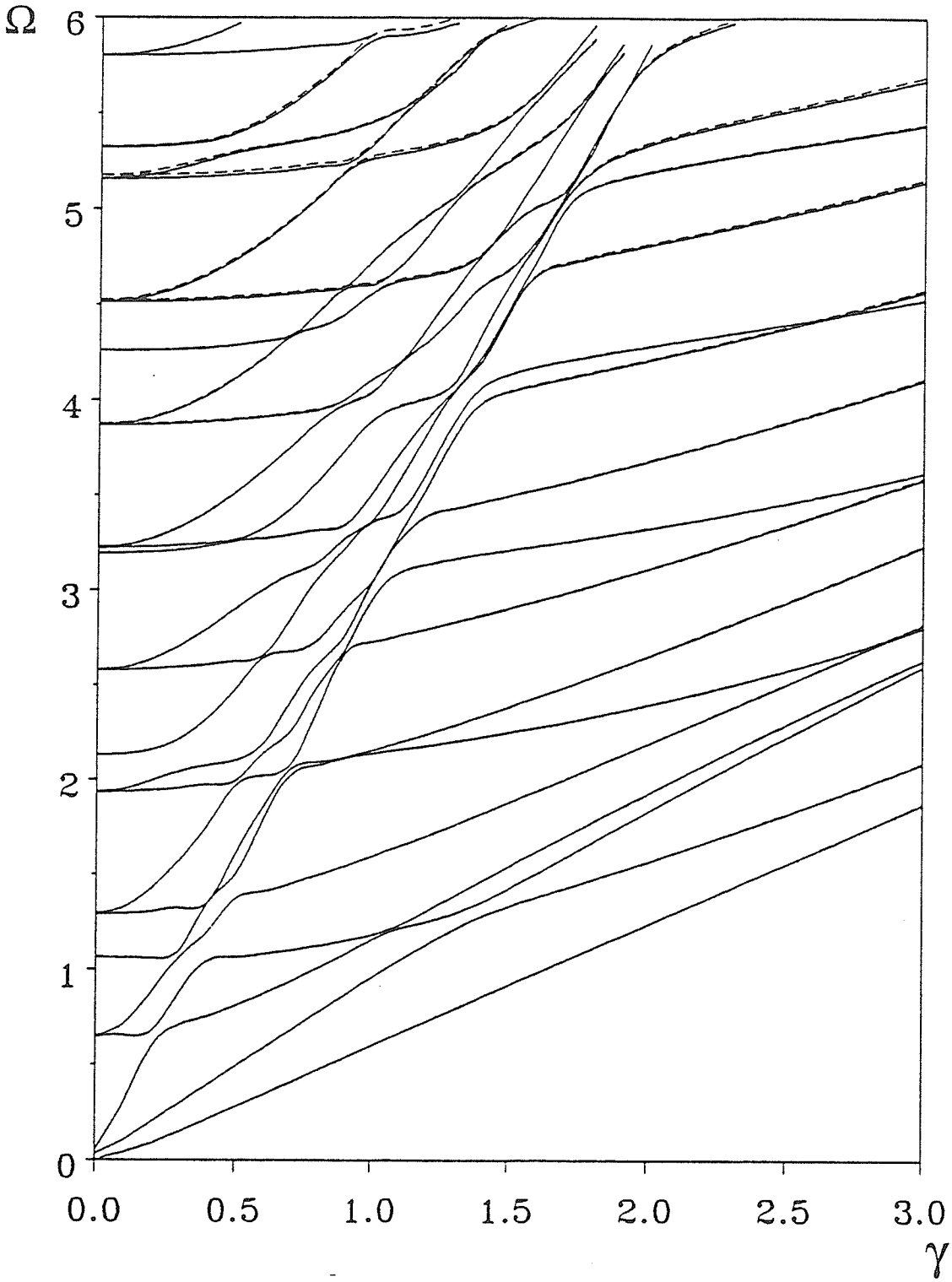

Figure 2.12: Frequency spectrum for a 16 ply $[+15/-15]_s$ graphite/epoxy cylinder with $H/R = 0.10$, and $m = 1$.

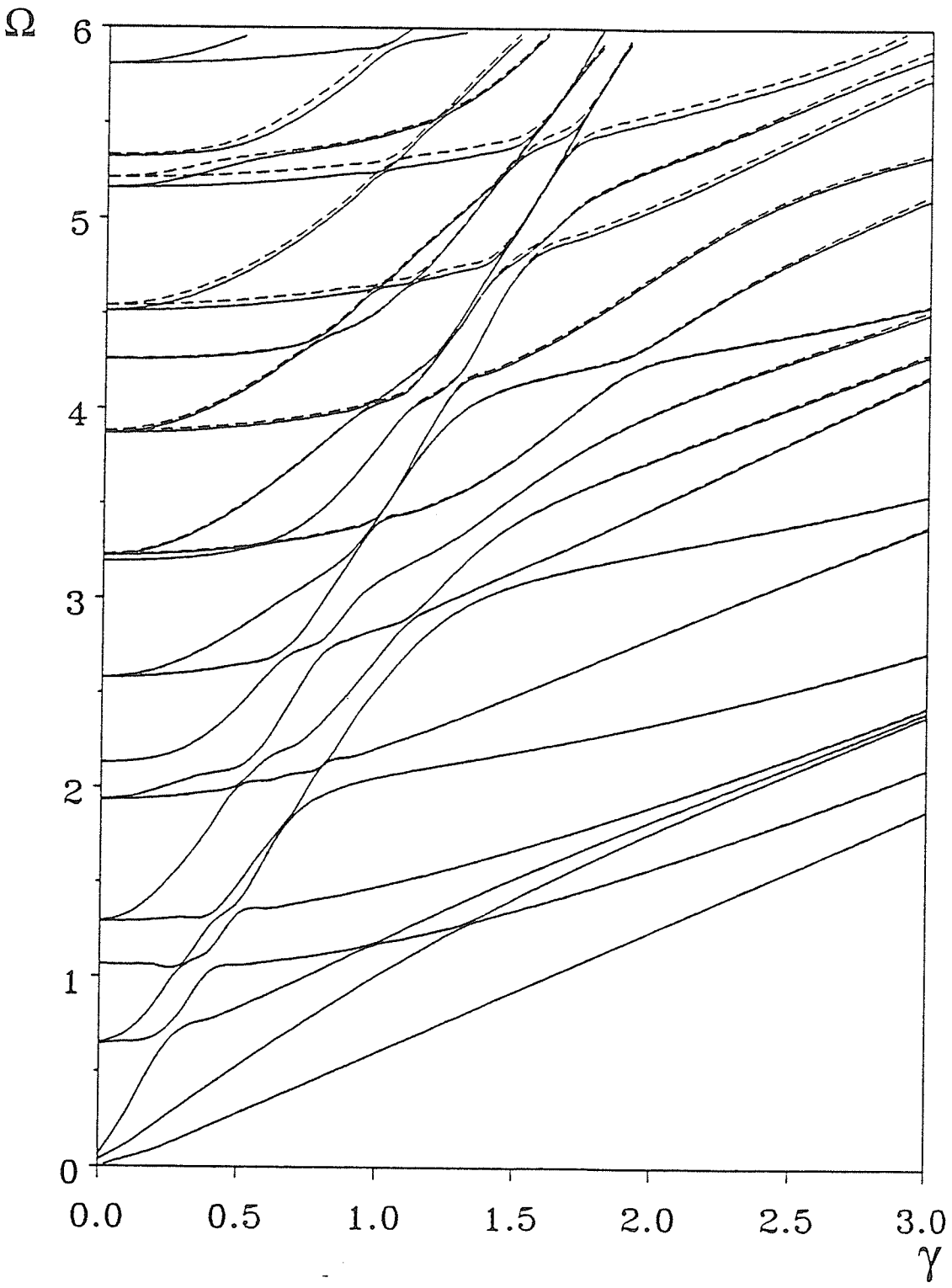

Figure 2.13: Frequency spectrum for a 12 ply $[0_2/+45/-45/0_2]_s$ graphite/epoxy cylinder with $H/R = 0.10$, and $m = 1$.

Chapter 3

Free End Reflection of Waves in Semi-infinite Cylinders

3.1 General

As mentioned in Chapter 1, the study of wave propagation in cylinders has many applications, such as nondestructive evaluation of material properties, flaw detection, and the determination of resonance. Free end reflection problem, one of the scattering problems, which is investigated in the present chapter also requires the basic knowledge of wave propagation which was presented in Chapter 2. The present study of free end reflection in cylinder will help in contriving suitable techniques to analyse more complicated problem of wave scattering due to cracks in cylinder.

When a wave travels along a semi-infinite cylinder and strikes at the free edge of the cylinder, an infinite number of reflected waves is generated. These reflected waves may have real, imaginary, or complex wavenumbers. Only a finite number of these waves, with real wavenumbers, propagate energy. The imaginary and complex modes carry

no energy and their amplitudes exponentially decay with the distance. However, these non-propagating and evanescent modes, the imaginary and complex modes, respectively, are as significant as the propagating modes at the edge of the cylinder in satisfying the traction free end condition. The reflected wave field is represented by the modal sum of a finite number of wave functions (Karunasena *et al.*, 1991). These wave functions or eigenfunctions at discrete points through the thickness of the cylinder can be obtained from the propagator matrix for laminated isotropic cylinders. On the other hand, the Rayleigh-Ritz type approximation with displacement continuity, presented in Chapter 2, is employed where analytical solution is unattainable. The amplitudes of the wave functions are determined by satisfying the traction free end conditions using the least square and variational methods.

The validation and the accuracy of the methods are demonstrated by comparing the results with existing results for a homogeneous isotropic elastic solid rod. The comparison between the results obtained from the displacement continuity method and the propagator matrix approach illustrates the applicability of the Rayleigh-Ritz type approximation in the free end reflection problem. Numerical results for a two-layered isotropic cylinder and for a four ply graphite/epoxy cylinder are presented. In each case, the division of energy among various reflected modes is also presented.

3.2 Description of the Problem

A semi-infinite laminated cylinder considered occupies the region $z \geq 0$ in the cylindrical coordinates r, θ, and z as shown in Figure 3.1. The layers or laminae may have distinct mechanical properties as well as different thicknesses. These layers are assumed to be perfectly bonded together. The thickness of the cylinder, H, is discretized into N sub-layers to model the radial inhomogeneity and to compute the eigenvectors at discrete points. The cylinder is excited at $z = +\infty$ which generates the incident wave with an-

gular frequency of ω and wavenumber of ξ_{in}. This time harmonic guided wave travels in the negative $z-$direction and impinges upon the free end $z = 0$ of the cylinder. The objective herein is to investigate the reflected waves generated after the incident wave strikes the free edge of the cylinder.

3.3 Wave Functions

Wave functions required for the reflection analysis are obtained by considering the elastic wave propagation in the corresponding infinite cylinder. For this purpose, each layer is divided into several sublayers so that the total number of sublayers through the thickness, H, is N. Two approaches are employed in the present chapter, viz. the propagator matrix method for laminated isotropic cylinders, and the displacement based Rayleigh-Ritz type approximation for laminated composite cylinders. The displacement continuity method is preferred over the stress continuity approach mainly due to the fact that, for given ω, the stress continuity approach involves a fourth order eigenvalue problem whilst the displacement continuity method contains only a quadratic eigenvalue problem. One should note here that the fourth order eigenvalue problem requires much larger computer time and core memory than the quadratic eigenvalue problem. Also, it is observed from Chapter 2 that the discrepancy between the results obtained from both the approximate methods is considered small.

As discussed in section 2.5, for a particular value of ω, the roots of the dispersion relations will have the form of complex wavenumber, equation (2.39), as:

$$\xi = \xi_{\mathrm{R}} - i\xi_{\mathrm{I}}.$$

The admissible ξ for the reflected wave field in the semi-infinite cylinder are those real roots with positive group velocity and those non-real roots with $\xi_{\mathrm{I}} > 0$. These conditions ensure that the reflected waves produce bounded displacement and stress fields through-

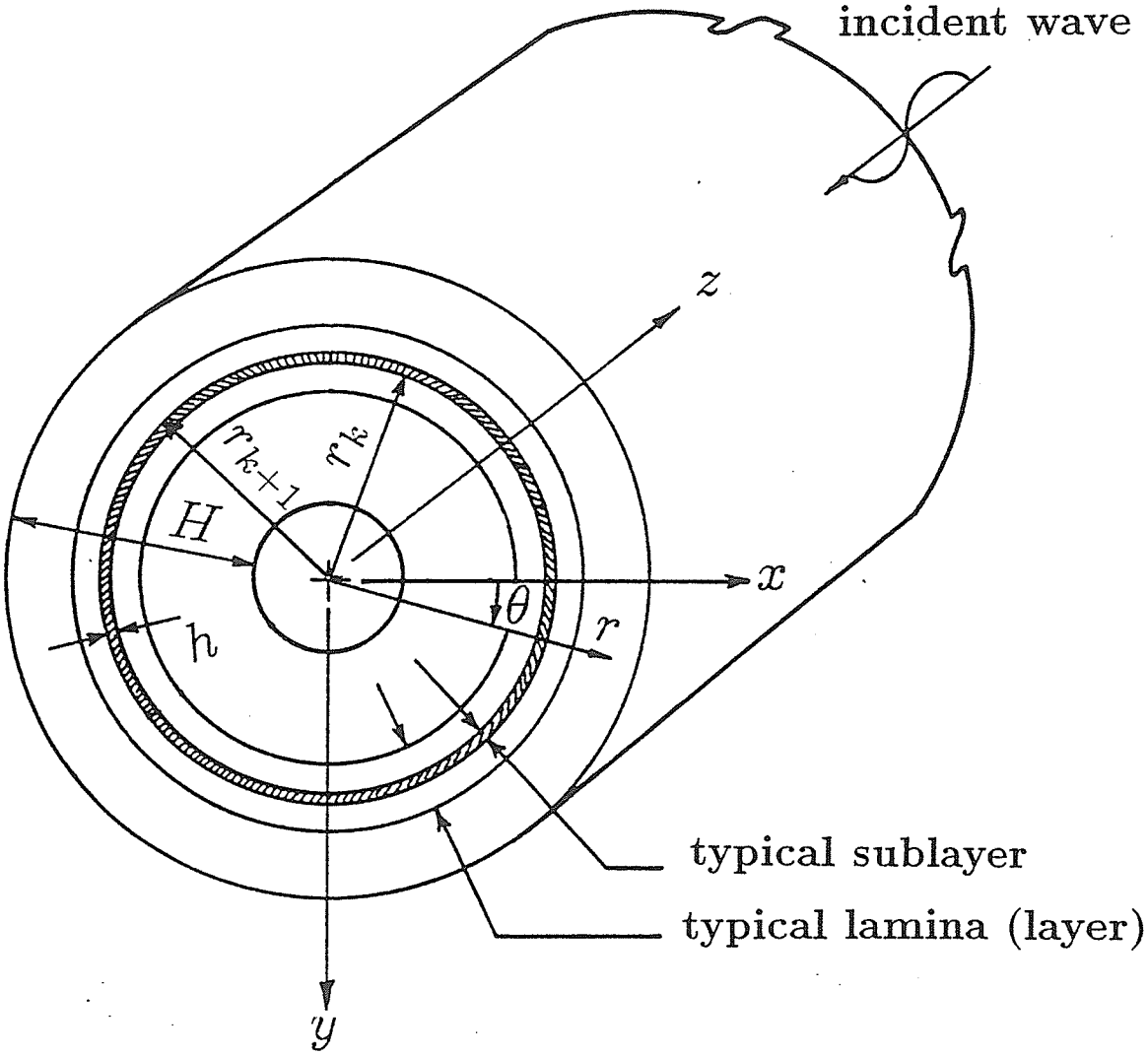

Figure 3.1: Geometry of semi-infinite laminated cylinder

out the cylinder. In solving the transcendental functions, equations (2.17) and (2.22), Muller's method is employed. At the first step, beginning with the lowest frequency, the cylinder is discretized into a sufficiently large number of sublayers and the approximate roots are obtained via the displacement based Rayleigh-Ritz type approximation. Those approximate roots lying in the first quadrant of the complex $\xi-$plane are used as initial guesses to recover the exact roots. It should be noted that the division into sublayers is not required to obtain the exact roots, but is used to compute the eigenvectors in the modal expansion method. At the next step, ω is increased by a small increment and the exact roots from the previous step are taken as initial guesses for the current step. The process is repeated until the frequency range of interest is scanned. As a check, at some intermediate frequencies, the approximate roots from the displacement based Rayleigh-Ritz type approximation are used as initial guesses in the Muller's method to obtain the exact roots as mentioned in section 2.5. After obtaining the wavenumbers, ξ, the sign of the real wavenumbers are adjusted to have positive group velocities.

3.4 Reflected Wave Field and Incident Field

The reflection occurs after the wave strikes the edge $z = 0$ of the cylinder. The reflected waves consist of a finite number of waves with real wavenumber and an infinite number of waves with imaginary and complex wavenumbers. The displacement vector corresponding to these reflected waves $\{q_z\}_{re}$ at any arbitrary z has the form of:

$$\{q_z\}_{re} = \sum_{j=0}^{\infty} A_j \{q_j\} e^{-i(\xi_j z - \omega t)} e^{im\theta}; z \geq 0, \tag{3.1}$$

where

$$\{q_j\}^{\mathrm{T}} = \left\langle u_{1j} \;\; v_{1j} \;\; w_{1j} \;\; \ldots \;\; u_{kj} \;\; v_{kj} \;\; w_{kj} \;\; \ldots \;\; u_{(NP)j} \;\; v_{(NP)j} \;\; w_{(NP)j} \right\rangle, \tag{3.2}$$

NP being the number of nodal points. The displacements u_{kj}, v_{kj}, and w_{kj} at the k^{th} nodal point associated with the j^{th} mode can be obtained from equation (2.11) or (2.32). The complex amplitude A_j of the j^{th} mode is to be determined so that the associated

stress field satisfies the free end condition. The factor $e^{i\omega t}e^{im\theta}$ will be suppressed in the following formulation.

For the purpose of numerical evaluation, the series in equation (3.2) is truncated to J terms. Only the modes corresponding to the wavenumbers with small negative imaginary part are superposed (Gregory and Gladwell, 1989). As mentioned earlier, the wavenumbers having positive imaginary part are unbounded for large z and, therefore, they are not admissible. In the wavenumber determination process, after obtaining the wavenumbers ξ_j for each frequency, only J number of roots are chosen. The selected roots must include all the propagating modes. The real roots are ordered in the descending order of the amplitude while the non-propagating and evanescent modes are ordered in the ascending order of magnitude of their imaginary parts.

The reflected wave field at the edge $z = 0$, $\{q_0\}_{re}$, with J modes approximation can then be written as:

$$\{q_0\}_{re} = [G]\,\{A\}, \tag{3.3}$$

where

$$[G] = [\{q_1\}\ \{q_2\}\ \ldots\ \{q_j\}\ \ldots\ \{q_J\}], \tag{3.4}$$

$$\{A\}^{\mathrm{T}} = \langle A_1\ \ A_2\ \ldots\ A_j\ \ldots\ A_J\rangle\,. \tag{3.5}$$

The stress components (σ_{rz}, $\sigma_{\theta z}$, and σ_{zz}) at discrete points on the surface $z =$ constant of the k^{th} sublayer can be obtained by the stress-strain and the strain-displacement relations as:

$$\begin{aligned}
\sigma_{rz} &= C_{15}\frac{du}{dr} + \frac{C_{25}}{r}(u + imv) - i\xi C_{35}w + iC_{45}(\frac{m}{r}w - \xi v) \\
&\quad + C_{55}(\frac{dw}{dr} - i\xi u) + C_{56}(\frac{im}{r}u + \frac{dv}{dr} - \frac{v}{r}), \\
\sigma_{\theta z} &= C_{14}\frac{du}{dr} + \frac{C_{24}}{r}(u + imv) - i\xi C_{34}w + iC_{44}(\frac{m}{r}w - \xi v) \\
&\quad + C_{45}(\frac{dw}{dr} - i\xi u) + C_{46}(\frac{im}{r}u + \frac{dv}{dr} - \frac{v}{r}),
\end{aligned} \tag{3.6}$$

$$\sigma_{zz} = C_{13}\frac{du}{dr} + \frac{C_{23}}{r}(u + imv) - i\xi C_{33}w + iC_{34}(\frac{m}{r}w - \xi v)$$
$$+C_{35}(\frac{dw}{dr} - i\xi u) + C_{36}(\frac{im}{r}u + \frac{dv}{dr} - \frac{v}{r}).$$

For the isotropic sublayer, with the propagator matrix approach, knowing the three displacement components: u, v, and w; and the three stress components: σ_{rr}, $\sigma_{r\theta}$, and σ_{rz}; together with the above equations, the two required stress components can be written as:

$$\begin{aligned}\sigma_{\theta z} &= -i\xi\mu v + \frac{im\mu}{r}w, \\ \sigma_{zz} &= \frac{\lambda}{(\lambda+2\mu)}\sigma_{rr} + \frac{2\mu\lambda}{r}(u + imv) - i4\mu^2\xi w. \end{aligned} \tag{3.7}$$

In the Rayleigh-Ritz type approximation, with the interpolation polynomial functions, the explicit form of the three stress components in equation (3.6) can be written as:

$$\{S\} = [N_3]\{\tilde{q}\}, \tag{3.8}$$

where

$$\{S\}^{\mathrm{T}} = \langle \sigma_{rz} \;\; \sigma_{\theta z} \;\; \sigma_{zz} \rangle, \tag{3.9}$$

$\{\tilde{q}\}$ is the vector of generalized displacements and is defined in equation (2.26). The matrix $[N_3]$ is given in Appendix E. Note that $\sigma_{\theta z}$ and σ_{zz} may not be continuous at the interfaces between the sublayers. The stress vector containing these stress components due to the reflected field at the free end surface can be formulated as:

$$\{R\}_{re} = [F]\{A\}, \tag{3.10}$$

where

$$[F] = [\{S_1\} \;\; \{S_2\} \;\; \ldots \;\; \{S_j\} \;\; \ldots \;\; \{S_J\}], \tag{3.11}$$

$$\{S_j\}^{\mathrm{T}} = \left\langle \sigma_{rz1j} \;\; \sigma_{\theta z1j} \;\; \sigma_{zz1j} \;\; \ldots \sigma_{rzkj} \;\; \sigma_{\theta zkj} \;\; \sigma_{zzkj} \;\; \ldots \sigma_{rz(NP)j} \;\; \sigma_{\theta z(NP)j} \;\; \sigma_{zz(NP)j} \right\rangle. \tag{3.12}$$

It must be mentioned here that when the circumferential wavenumber, m, is not zero, the wavenumber ξ_j and ξ'_j for propagating modes in the positive and negative

$z-$direction, respectively, are not the same for laminated composite cylinder unless the material properties are symmetric with respect to θ. Once the wavenumber, ξ_j', for the incident mode has been selected, it was found convenient to evaluate the incident field quantities in the (r, θ', z') coordinates where $\theta' = -\theta$ and $z' = -z$. With this, the incident field at the edge $z = 0$, $\{q_0\}_{in}$, with J modes approximation can be written in the same form as equation (3.3) as:

$$\{q_0\}_{in} = A_{in}\{G_{in}\}, \tag{3.13}$$

Similarly, the stress vector due to the incident field at the free edge can be written as:

$$\{R\}_{in} = A_{in}\{F_{in}\}, \tag{3.14}$$

where A_{in} is the amplitude of the incident mode. The displacement and stress vectors, $\{G_{in}\}$ and $\{F_{in}\}$, respectively, are calculated from the wave corresponding to the propagating incident mode.

The traction free condition at $z = 0$ requires that

$$\{R\} = \{R\}_{re} - \{R\}_{in} = 0. \tag{3.15}$$

By minimizing the sum of the squares of the residuals of $\{R\}$, the least square solution for complex amplitude $\{A\}$ is obtained as:

$$\{A\} = A_{in}\Big[\int_{r_i}^{r_o}\left[\bar{F}\right]^{\mathrm{T}}[F]\,r\,dr\Big]^{-1}\Big[\int_{r_i}^{r_o}\left[\bar{F}\right]^{\mathrm{T}}\{F_{in}\}\,r\,dr\Big], \tag{3.16}$$

where r_i and r_o represent the inner and the outer radii of the cylinder, respectively.

An alternate approach of determining the complex amplitude $\{A\}$ is to employ the variational principle (Wu and Plunkett, 1967). Using the principle of virtual displacement, one obtains:

$$\delta\{\bar{q}_0\}^{\mathrm{T}}\{R\} = 0, \tag{3.17}$$

where δ represents variation. The total displacement field $\{q_0\}$ at the free end surface of the cylinder is:

$$\{q_0\} = \{q_0\}_{in} + \{q_0\}_{re}, \tag{3.18}$$

in which

$$\delta\{q_0\} = \delta\{q_0\}_{re}. \tag{3.19}$$

The solution is obtained by substituting equations (3.3), (3.15), and (3.19) into equation (3.18). This leads to:

$$\{A\} = A_{in}\Big[\int_{r_i}^{r_o}\big[\bar{G}\big]^{\mathrm{T}}[F]\,r\,dr\Big]^{-1}\Big[\int_{r_i}^{r_o}\big[\bar{G}\big]^{\mathrm{T}}\{F_{in}\}\,r\,dr\Big]. \tag{3.20}$$

The normalized amplitude B_j of the j^{th} mode is defined by:

$$B_j = \frac{A_j}{A_{in}}. \tag{3.21}$$

Once the amplitude $\{A\}$ is known, the displacement and stress fields anywhere in the cylinder can be computed.

3.5 Energy Flux

One of the physical quantities of interest is the mean total energy flux. Reflected energy is carried only by the various propagating modes which can exist at that particular frequency. The instantaneous value of the energy flux, associated with the j^{th} reflected propagating mode, per unit length in $z-$direction, through a cylinder cross section located at any z ($z \geq 0$) is given by:

$$\tilde{E}_j = -\frac{1}{2}\int_{r_i}^{r_o}\Big[\{R_{zj}\}_{re}^{\mathrm{T}}\frac{d\{\bar{q_{zj}}\}_{re}}{dt} + \{\bar{R_{zj}}\}_{re}^{\mathrm{T}}\frac{d\{q_{zj}\}_{re}}{dt}\Big]r\,dr \quad ; \quad j \leq N_{pr}, \tag{3.22}$$

where

$$\{q_{zj}\}_{re} = A_j\{q_j\}e^{-i(\xi_j z-\omega t)}e^{im\theta}, \tag{3.23}$$

$$\{R_{zj}\}_{re} = A_j\{S_j\}e^{-i(\xi_j z-\omega t)}e^{im\theta}, \tag{3.24}$$

The $\{q_{zj}\}_{re}$ and $\{R_{zj}\}_{re}$ represent, respectively, the displacement and the stress vectors associated with the j^{th} reflected mode at any cross section z. N_{pr} is the number of propagating modes in the reflected field. The time-averaged value of the energy flux, associated

with the j^{th} reflected mode, per unit length in $z-$direction, through the cylinder cross section is obtained by averaging $\tilde{E}_j$ over one cycle. This is given by:

$$E_j = \frac{1}{2\pi/\omega} \int_0^{2\pi/\omega} \tilde{E}_j dt. \tag{3.25}$$

After carrying out the integration in equation (3.25), E_j can explicitly expressed as:

$$E_j = \omega \left|A_j\right|^2 Im\Big[\int_{r_i}^{r_o} [\{F_j\}^{\mathrm{T}} \{\bar{q}_j\}\, r dr]\Big] \quad ; \quad j \leq N_{pr}, \tag{3.26}$$

The mean total energy flux is calculated from the sum of the energy fluxes carried by reflected propagating modes. This is given by:

$$E_{re} = \sum_{j=1}^{N_{pr}} E_j. \tag{3.27}$$

The energy flux of the incident field can be written in the similar form as:

$$E_{in} = \omega \left|A_{in}\right|^2 Im\Big[\int_{r_i}^{r_o} [\{F_{in}\}^{\mathrm{T}} \{\bar{q}\}_{in}\, r dr]\Big]. \tag{3.28}$$

The proportion of the incident energy transferred into the j^{th} reflected propagating mode is:

$$I_j = \frac{E_j}{E_{in}}. \tag{3.29}$$

Since the free end condition requires no energy dissipation when the wave reflects, the percentage difference in energies carried by the incident and the reflected fields is then given by:

$$|\epsilon| = \left|[E_{in} - E_{re}]100/E_{in}\right|. \tag{3.30}$$

The principle of energy conservation requires that $|\epsilon| = 0$. The smallness of the value of $|\epsilon|$ is an useful index to assess the accuracy of the numerical results.

3.6 Numerical Evaluation and Discussion

To validate and to assess the accuracy and the application of the methods, the following three numerical examples are considered:

1. A homogeneous isotropic elastic rod.

2. A two-layered isotropic hollow cylinder.

3. A 4-ply $[+15/-15/+15/-15]$ graphite/epoxy hollow cylinder.

In all examples, the frequency and the wavenumber, whenever referred, are the normalized frequency, Ω, and the normalized wavenumber, γ, with the forms of:

$$\Omega = \frac{\omega}{\omega_{ref}} \quad ; \quad \gamma = \frac{\xi}{\xi_{ref}},$$

where ω_{ref} and ξ_{ref} are the reference frequency and the reference wavenumber, respectively.

The total number of sublayers N used to compute the discrete eigenvectors and the number of modes J used in the modal expansion are very important factors for the accuracy of the method. Reasonably good values of N and J are chosen in such a way that the amplitude $\{A\}$ in equation (3.16) or (3.20) and the proportion of the energy carried by each reflected mode I_j in equation (3.29) converge.

Example 1

The reflection of the first axisymmetric wave in a solid rod with the Poisson's ratio ν of 0.25 is considered. The reference frequency and the reference wavenumber are, respectively;

$$\omega_{ref} = \frac{v_p}{H} \quad ; \quad \xi_{ref} = \frac{1}{H},$$

where v_p is the velocity of dilatation wave. A full discussion of the frequency spectrum for this case was given by Onoe *et al.* (1962). The first three cut-off frequencies are $\Omega = 1.931$, 2.069, and 2.212. The propagator matrix approach with 20 sublayers (corresponding to 42 degrees of freedom) and 21 modes are employed in this present example. Figure 3.2a and 3.2b show the normalized amplitude B_j and the proportion of energy I_j of each reflected

mode. The comparison of the proportion of energy obtained by the present method with that of Gregory and Gladwell (1989) is made. It can be seen that the method presented herein yields results that are in exellent agreement with those obtained by Gregory and Gladwell. For the range of Ω in Figure 3.2, $|\epsilon|$ is less than 0.5 %. From the numerical experimentation, it is observed that there is no discrepancy between the results obtained by the least square method and those obtained by the variational technique, equations (3.16) and (3.20), respectively, in this example.

The numerical results confirmed that the end resonant frequency for this rod is 1.644 which is identical to the one obtained by Gregory and Gladwell.

Example 2

The reflection of the first propagating mode in a two-layered isotropic cylinder is considered. The properties of the two layers are given in Chapter 2 i.e., $\nu_1 = \nu_2 = 0.30$; $\mu_1/\mu_2 = 1$; $\rho_1/\rho_2 = 2$; $h_1/h_2 = 1$. The subscripts 1 and 2 represent the inner and the outer layer, respectively. The ratio of the thickness to the mean radius of the outer layer, h_2/R_2, is 0.20. The circumferential wavenumber m is 1. The reference frequency and the reference wavenumber are, respectively:

$$\omega_{ref} = \frac{2\pi v_{s2}}{H} \quad ; \quad \xi_{ref} = \frac{2\pi}{H},$$

where v_{s2} is the shear wave velocity in the outer layer. The frequency spectrum for this cylinder was presented in Chapter 2. The first four cut-off frequencies are $\Omega =$ 0.059, 0.145, 0.428, and 0.438. The propagator matrix approach and the displacement based Rayleigh-Ritz type approximation are employed in this example to illustrate the applicability and the accuracy of the Rayleigh-Ritz type approximation for the reflection problem. In order that the two methods are to be comparable, the discretizations are made in such a way that both methods have the same number of degrees of freedom. It is found that 99 degrees of freedom (corresponding to 32 and 16 sublayers for the propagator matrix approach and the Rayleigh-Ritz type approximation, respectively) and 30 modes

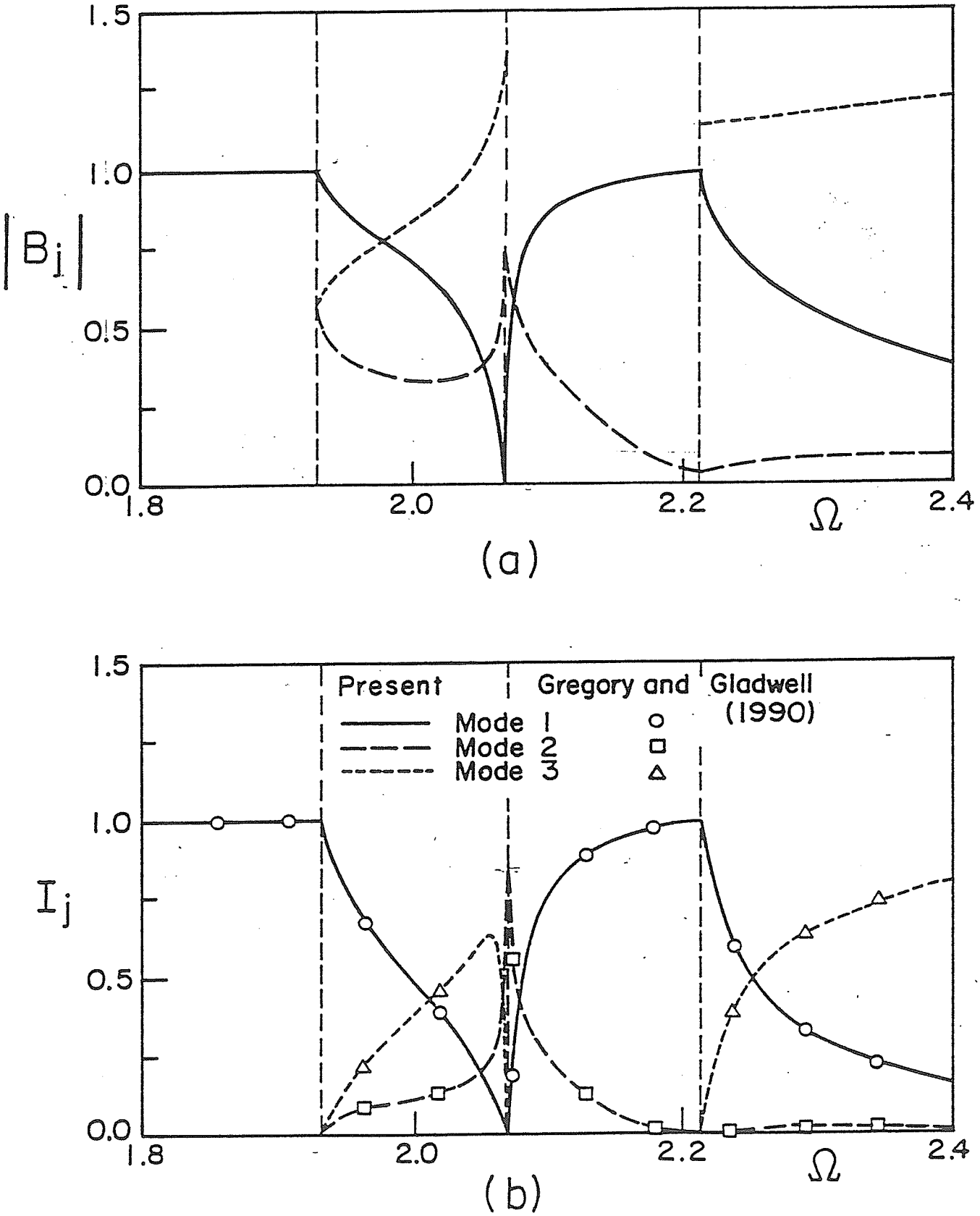

Figure 3.2: Reflection in isotropic elastic rod (a) the normalized amplitude $|B_j|$, (b) the proportion of energy I_j.

provide reasonably good results.

Figures 3.3a and 3.3b illustrate the normalized amplitudes B_j and the proportion of energy I_j of each reflected propagating mode, respectively. It can be observed that the results from both methods are in excellent agreement. For the frequencies lower than the first cut-off frequency, only one reflected propagating mode is possible. This mode has the same absolute amplitude as that of the incident wave and carries all of the energy back. At the first cut-off frequency, the second propagating mode becomes predominant. The amplitude of this second cut-off frequency is comparatively large. This phenomenon, however, is not very stable as the frequency is shifted away from the first cut-off frequency. The first propagating mode recovers its dominacy as the frequency increases. This mode is also predominant in the frequency range between the second and the third cut-off frequencies. Between the third and the fourth cut-off frequencies, the fourth propagating mode has very high amplitude. However, its amplitude is not high enough to be considered as a resonant phenomenon. For the frequency greater than the fourth cut-off frequency, the fifth propagating mode predominates all other modes except in a small region around $\Omega = 0.62$ as shown in the inserts in the Figures. An investigation in this particular region reveals that the first mode is the breathing mode, the second and the fourth modes are torsional modes whilst the third and the fifth modes are the modes coupling of the longitudinal motions.

For the range of Ω considered in Figures 3.3, $|\epsilon|$ is less than 0.5 %. Similar to the first example, the results obtained from the least square method and those obtained by the variational technique show negligible discrepancy.

Example 3

The reflection of the first incoming propagating mode in a 4-ply $[+15/-15/+15/-15]$ graphite/epoxy is considered. The elastic properties for each ply relative to their natural

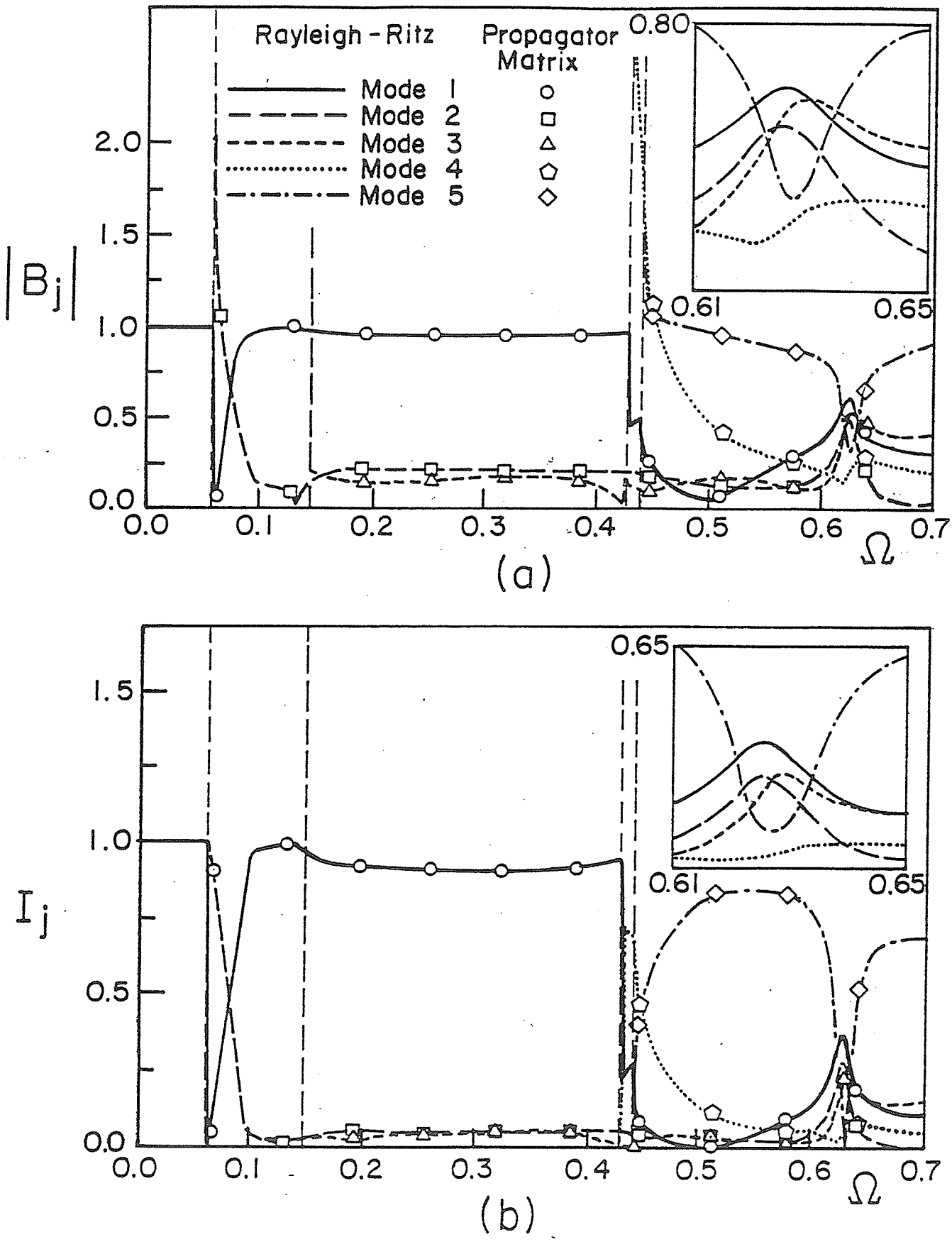

Figure 3.3: Reflection in two-layered isotropic cylinder (a) the normalized amplitude $|B_j|$, (b) the proportion of energy I_j.

elastic axes are given in the previous chapter, equation (2.43), as:

$$E_L = 13.9274 \times 10^{10} N/m^2 \ ; \ E_T = 1.5169 \times 10^{10} N/m^2 \ ;$$

$$G_{LT} = G_{TT} = 0.5861 \times 10^{10} N/m^2 \ ; \ \nu_{LT} = \nu_{TT} = 0.21.$$

The normalized frequency and the normalized wavenumber are given, respectively, by:

$$\omega_{ref} = \frac{v_L}{H} \quad ; \quad \xi_{ref} = \frac{H}{\pi},$$

where

$$v_L^2 = \frac{E_L}{\rho}.$$

The circumferential wavenumber m and H/R are 1 and 0.667, respectively. As previously discussed, when the waves travel in the anisotropic cylinder with the circumferential wavenumber greater than zero, the wavenumber of waves travelling in the positive $z-$direction differs from that of the waves travelling in the negative $z-$direction. Figure 3.4 shows the frequency spectrum for this cylinder. The solid lines represent the waves travelling in the positive $z-$direction, while the dashed lines illustrate the waves travelling in the negative $z-$direction. The first four cut-off frequencies are $\Omega = 0.215$, 0.295, 0.696, and 0.760.

Since the analytical solution is unattainable for laminated composite cylinders, the displacement based Rayleigh-Ritz type approximation is employed in this example. The cylinder is discretized into 16 sublayers (corresponding to 99 degrees of freedom) and 30 modes are considered.

Figures 3.5a and 3.5b show the normalized amplitudes B_j and the proportion of energy I_j of each reflected propagating mode. Unlike the previous example, the propagating modes in the positive and in the negative $z-$direcctions are different. Therefore, for frequencies lower than the first cut-off frequency, the normalized absolute amplitudes of the reflected wave need not be unity. However, the conservation of the energy still holds, i.e. the energy carried by the incident wave is totally transferred to the reflected

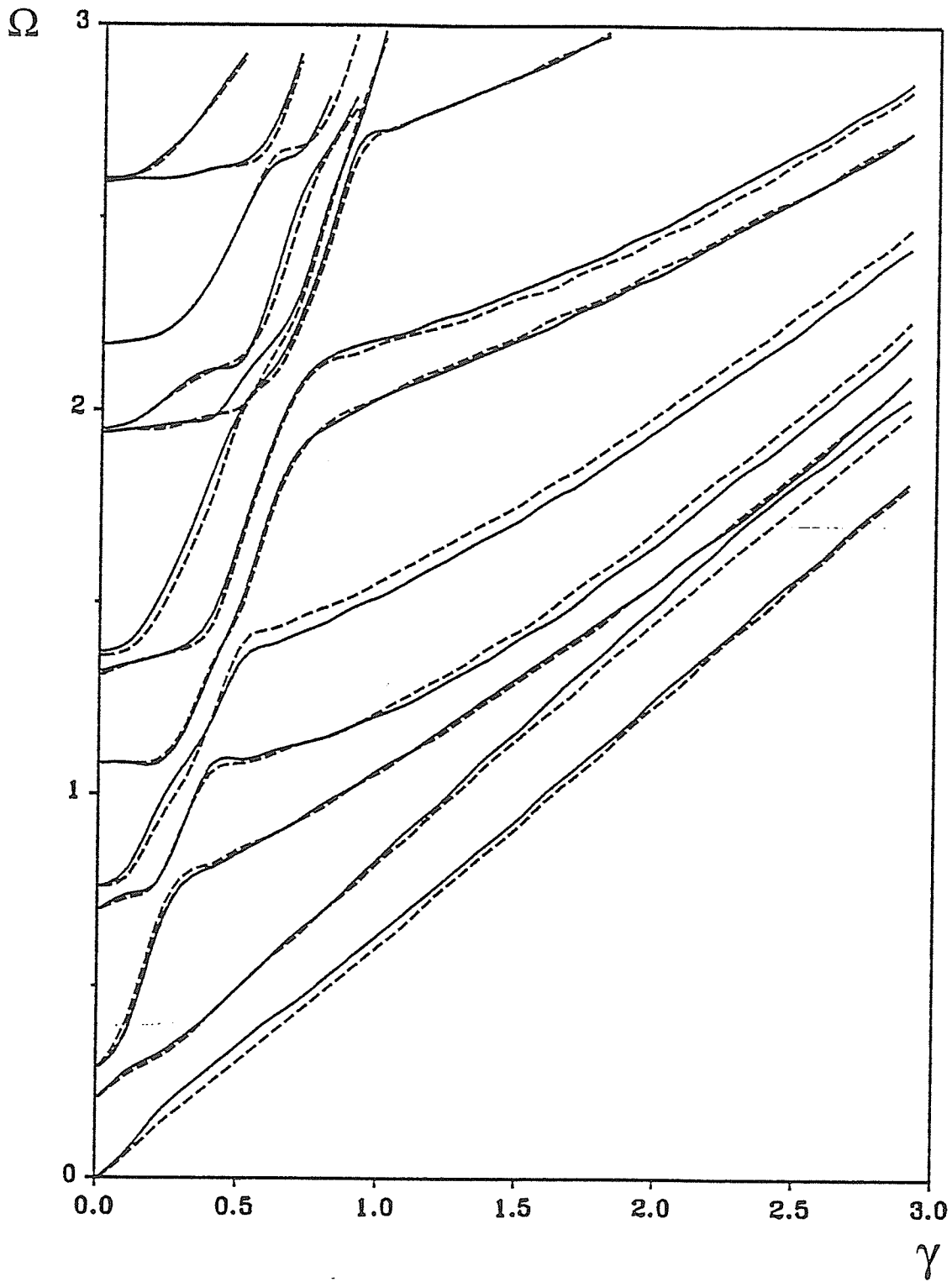

Figure 3.4: Frequency spectrum for 4-ply $[+15/-15/+15/-15]$ graphite/epoxy cylinder.

propagating wave as seen in Figure 3.5b. Similar to the case of layered isotropic cylinder, at the first cut-off frequency, the second mode becomes predominant. In the range between the second and the third cut-off frequencies, all three propagating waves are essential in carrying energy back. Between the third and the fourth cut-off frequencies, the patterns of both the normalized amplitude and the proportion of energy are very irregular. After the fourth cut-off frequency, all propagating modes in the reflected waves are contributing in the transfer of the energy. In this example, it is observed that the numerical results obtained by the least square method are very inaccurate. For the range of Ω considered here, the variational technique yields the $|\epsilon|$ of less than 0.5 % while the least square method gives $|\epsilon|$ up to 15 %. The reason for the anomalous results is that the least square method does not have a physical basis unlike the variational method in which the energy is minimized. Although the sum of the squares of the residuals is minimized in the least square method, the minimized residual sum could be large which results in large error in $|\epsilon|$.

A careful search was made for the end resonant frequency in examples 2 and 3 but none could be found in the range of the frequency considered and no attempt was made to search for the end resonant frequency outside this range.

3.7 Concluding Remarks

The free end reflection of waves in laminated cylinders are investigated by the wave function expansion method. To obtain the required eigenfunctions at the discrete points through the thickness of the cylinder, the propagator matrix approach is employed when the analytical solution is obtainable and the displacement based Rayleigh-Ritz type approximation is used when analytical solution is unattainable. Numerical results confirm the applicability and accuracy of the exploitation of the Rayleigh-Ritz type approximation in the free end reflection problem in laminated cylinders. The least square technique

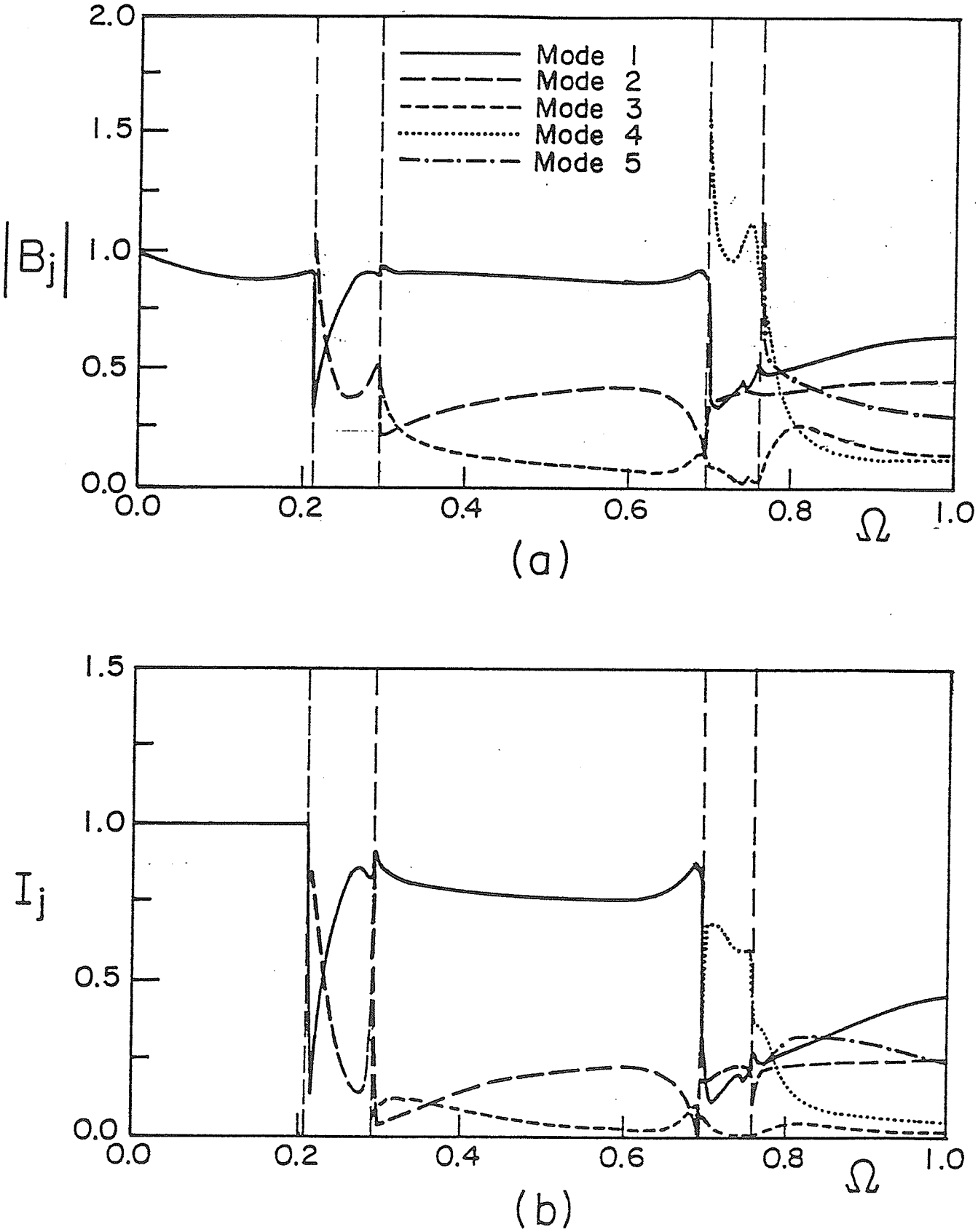

Figure 3.5: Reflection in 4-ply [+15/-15/+15/-15] graphite/epoxy cylinder,

(a) the normalized amplitude $|B_j|$, (b) the proportion of energy I_j.

as well as the variational method are employed in determining the complex amplitudes of the reflected waves. It is found that the results from the least square method are not reliable for the laminated anisotropic case.

Chapter 4

Plane Strain Wave Scattering by Cracks in Cylinders

4.1 General

CANDU Pressurized Heavy Water reactors contain hundreds of horizontally mounted zirconium-niobium (Zr-Nb) pressure tubes. These tubes hold the natural uranium fuel and are separated from the surrounding calandria tubes by garter springs. Having the inside diameter of 103 mm and the wall thickness of 4.2 mm with 6 metres in length, these Zr-Nb pressure tubes are designed to be accessed from either end via the end-fittings and closure plugs. They are routinely refuelled on-power using the fueling machine.

Although the Zr-Nb material is not particularly damage-tolerant, the pressure tubes are reliably designed for the primary pressure boundary. Nevertheless, defects, both from manufacturing and during service, have occasionally occurred. These defects are usually detected in-service using a focussed ultrasonic shear wave technique, the CIGAR (Channel Inspection and Gauging Apparatus for Reactors) system (Dolbey, 1986). How-

ever, it is difficult to obtain reliable information of flaw depth from this method alone. Many approaches were reported to help provide the information on defect size (Silk 1977, Achenbach *et al.* 1979, Golan *et al.* 1980, Tittman 1975, Coffey and Chapman 1983, Bond and Punjani 1984). The reports, however, were concerned typically with defects on the opposite face of a thick specimen. Hutchins and Moles (1991) proposed the hybrid immersion technique to investigate cracks of thin wall tubes. One of the models was to use two symmetrically positioned transducers generating ultrasonic waves and detecting the scattered waves due to the defects. It is with this motivation that the plane strain wave scattering due to defects in cylindrical cross-section is theorectically investigated in this chapter.

For simplicity of the analysis, the waves are generated by a harmonic line load. The cylinder is considered to be infinitely long in the longitudinal direction and, thus, the effect of shear is negligible. The cylinder is composed of layers perfectly bonded together. A hybrid method (Karunasena 1992) is presented in this chapter to solve the problem. In this method, the cross-section is divided into two regions - namely interior and exterior regions. The interior region which contains flaws or loads is modelled by finite elements. The exterior region is represented by a wave function expansion. These wave functions (eigenfunctions) are obtained by displacement based Rayleigh-Ritz type approximation since the analytical solution is unattainable. Continuity conditions for the displacements and interaction forces are imposed at the nodes lying on the boundaries between the two regions. This results in a system of linear equations which can be solved for the unknown wave function amplitudes. These complex amplitudes are used to calculate boundary nodal displacements and, in turn, to obtain interior nodal displacements. Although the method can be applied for general laminated composite cylindrical cross-section, only the numerical results for Zr-Nb pressure tube are presented to illustrate the applicability of the method.

4.2 Description of the Problem

An infinitely long thin wall cylinder with a line notch in the $z-$direction as shown in Figure 4.1 is considered. The cylinder may be composed of layers of distinct mechanical properties and different thicknesses. A time harmonic line load is excited on the cylindrical surface which generates elastic wave propagating in a circumferential, $\theta-$direction. This line load is bounded by the artificial boundaries B^+ and B^- at $\theta = \beta^+$ and $\theta = 2\pi - \beta^-$, respectively. The waves, generated by the load, in the exterior region of the boundaries are represented by wave functions expansion. When these waves strike the notch, the scattering occurs. The notch located at the distance of $\theta = \theta_0$ from the load is contained in another artificial interior region with the boundaries S^+ at $\theta = \theta_0 + \phi^+$, and S^- at $\theta = \theta_0 - \phi^-$. A scattered field from the notch is also represented by the wave functions expansion.

4.3 Finite Element for Interior Region

Consider a region bounded by artificial boundaries R^+ and R^- at $\theta = \theta^+$ and $\theta = 2\pi - \theta^-$, respectively, as shown in Figure 4.2. It is noted that the boundaries R^+ and R^- can be the boundaries B^+ and B^-, or S^+ and S^-, respectively, and θ^+ and θ^- are greater than zero. The region represents the interior region and may contain the line load or notch. This interior region is modelled by nine noded isoparametric finite elements. The coordinates r and θ, and the displacement components u and v in $r-$ and $\theta-$directions, respectively, at a point within a typical nine noded finite element (Figure 4.3) are approximated by polynomial interpolations as:

$$\begin{aligned} r &= \sum_{j=1}^{9} N_j r_j \quad ; \quad \theta = \sum_{j=1}^{9} N_j \theta_j; \\ u &= \sum_{j=1}^{9} N_j u_j \quad ; \quad v = \sum_{j=1}^{9} N_j v_j, \end{aligned} \tag{4.1}$$

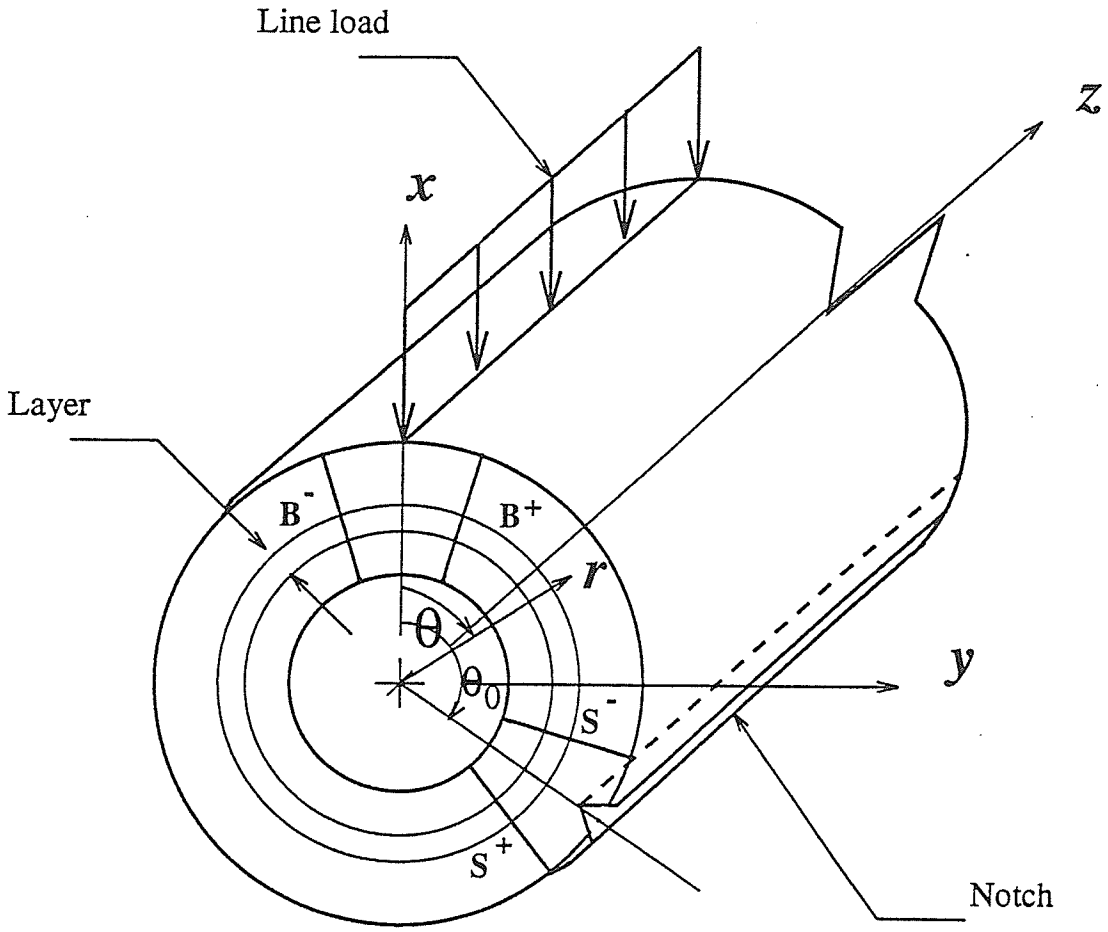

Figure 4.1: Geometry of cylinder with harmonic line load and line notch

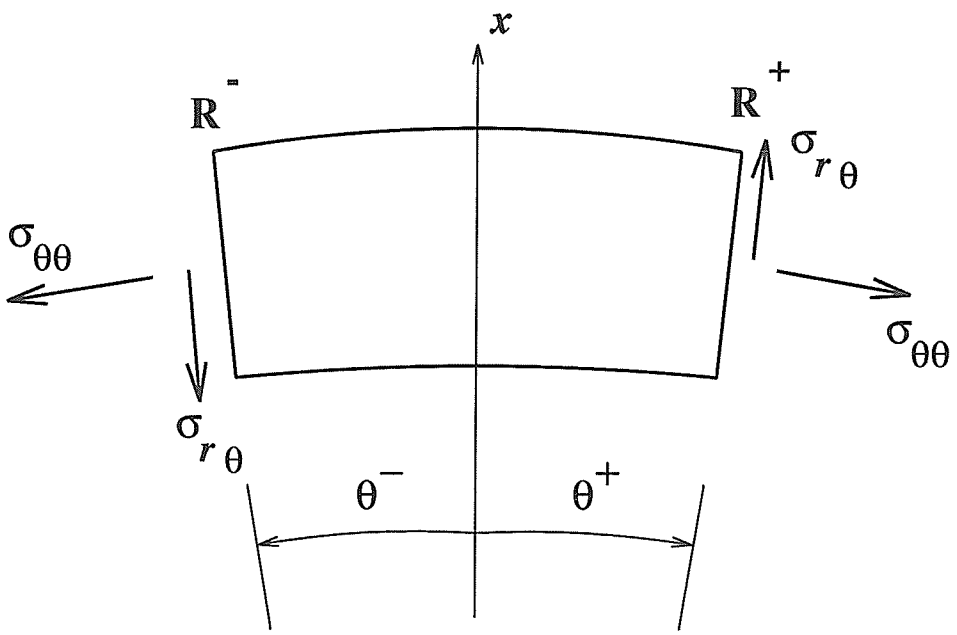

Figure 4.2: An arbitrary interior region

where r_j, θ_j are nodal coordinates and u_j and v_j are nodal displacements. $N_j (j = 1, \ldots, 9)$ are interpolation polynomials given as:

$$\begin{aligned}
N_1 &= \tfrac{\tilde{\xi}\tilde{\eta}}{4}(1-\tilde{\xi})(1-\tilde{\eta}), & N_5 &= -\tfrac{\tilde{\eta}}{2}(1-\tilde{\xi}^2)(1-\tilde{\eta}), \\
N_2 &= -\tfrac{\tilde{\xi}\tilde{\eta}}{4}(1+\tilde{\xi})(1-\tilde{\eta}), & N_6 &= \tfrac{\tilde{\xi}}{2}(1-\tilde{\eta}^2)(1+\tilde{\xi}), \\
N_3 &= \tfrac{\tilde{\xi}\tilde{\eta}}{4}(1+\tilde{\xi})(1+\tilde{\eta}), & N_7 &= \tfrac{\tilde{\eta}}{2}(1-\tilde{\xi}^2)(1+\tilde{\eta}), \\
N_4 &= -\tfrac{\tilde{\xi}\tilde{\eta}}{4}(1-\tilde{\xi})(1+\tilde{\eta}), & N_8 &= -\tfrac{\tilde{\xi}}{2}(1-\tilde{\eta}^2)(1-\tilde{\xi}),
\end{aligned} \tag{4.2}$$

$$N_9 = (1-\tilde{\xi}^2)(1-\tilde{\eta}^2),$$

$\tilde{\xi}$ and $\tilde{\eta}$ are non-dimensionalized coordinates system.

The strain vector, $\{\epsilon\}$, at a point is related to the displacement field through the following equation:

$$\{\epsilon\} = [L]\{U\}, \tag{4.3}$$

where

$$\{\epsilon\}^{\mathrm{T}} = \langle \epsilon_{rr} \quad \epsilon_{\theta\theta} \quad \gamma_{r\theta} \rangle , \tag{4.4}$$

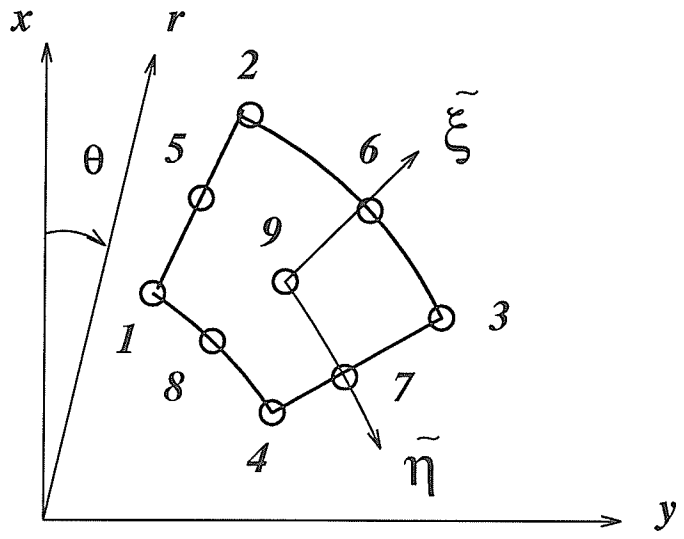

Figure 4.3: Nine noded element in cylindrical coordinate system

$$[L] = \begin{bmatrix} \frac{\partial}{\partial r} & 0 \\ \frac{1}{r} & \frac{1}{r}\frac{\partial}{\partial \theta} \\ \frac{1}{r}\frac{\partial}{\partial \theta} & \frac{\partial}{\partial r} - \frac{1}{r} \end{bmatrix}, \tag{4.5}$$

$$\{U\}^{\mathrm{T}} = \langle u \quad v \rangle . \tag{4.6}$$

In view of equation (4.1), the strain vector can be written in terms of nodal displacements as:

$$\{\epsilon\} = [B]\{q^e\}, \tag{4.7}$$

where

$$[B] = [L][\tilde{N}]. \tag{4.8}$$

$[\tilde{N}]$ is the polynomial interpolation or shape function matrix which contains the shape functions defined in equations (4.2) (Zienkiewicz 1977). $\{q^e\}$ is the nodal displacement vector for the element and is defined as:

$$\{q^e\}^{\mathrm{T}} = \langle u_1 \quad v_1 \quad u_2 \quad v_2 \quad \ldots \quad u_9 \quad v_9 \rangle . \tag{4.9}$$

The total energy functional, $\hat{\pi}$, per unit length in $z-$direction is in the form:

$$\hat{\pi} = \sum_e \Big[\frac{1}{2}\int_\theta \int_r \Big(\{\bar{\epsilon}\}^{\mathrm{T}}[C]\{\epsilon\} - \rho\omega^2\{\bar{U}\}^{\mathrm{T}}\{U\}\Big) r dr d\theta\Big] - \frac{1}{2}\Big[\{\bar{q}_T\}^{\mathrm{T}}\{P_T\} + \{q_T\}^{\mathrm{T}}\{\bar{P}_T\}\Big], \tag{4.10}$$

where

$$\begin{aligned} \{q_T\}^{\mathrm{T}} &= \left\langle \{q_I\}^{\mathrm{T}} \quad \{q_R\}^{\mathrm{T}} \right\rangle, \\ \{P_T\}^{\mathrm{T}} &= \left\langle \{P_I\}^{\mathrm{T}} \quad \{P_R\}^{\mathrm{T}} \right\rangle. \end{aligned} \tag{4.11}$$

$\{q_I\}$ and $\{P_I\}$ are the nodal displacement and force vectors corresponding to the nodes within the interior region, respectively, while $\{q_R\}$ and $\{P_R\}$ represent those quantities vectors corresponding to the nodes lying on the boundaries. $[C]$ is the elastic modulus matrix, $\sum_e$ denotes the summation over all the finite elements and overbar represents the complex conjugate. By substituting equations (4.1) and (4.7) into equation (4.10), and after the conventional assembly process in the finite element method, the total energy functional becomes:

$$\hat{\pi} = \frac{1}{2}\{\bar{q}_T\}^{\mathrm{T}}[S]\{q_T\} - \frac{1}{2}\Big[\{\bar{q}_T\}^{\mathrm{T}}\{P_T\} + \{q_T\}^{\mathrm{T}}\{\bar{P}_T\}\Big], \tag{4.12}$$

where

$$[S] = [K_T] - \omega^2[M_T] = \begin{bmatrix} [S_{II}] & [S_{IR}] \\ [S_{RI}] & [S_{RR}] \end{bmatrix}. \tag{4.13}$$

$[K_T]$ and $[M_T]$ in equation (4.13) are, respectively, the global stiffness and mass matrices of the interior region resulting from the assembly process. The element stiffness and mass matrices, $[k^e]$ and $[m^e]$, respectively, are defined as:

$$\begin{aligned} [k^e] &= \int_\theta \int_r [B]^{\mathrm{T}}[C][B] r dr d\theta, \\ [m^e] &= \int_\theta \int_r \rho[\tilde{N}]^{\mathrm{T}}[\tilde{N}] r dr d\theta. \end{aligned} \tag{4.14}$$

The governing equation of motions of the entire interior region can be obtained by minimizing the energy functional as:

$$\delta\hat{\pi} = \delta\{\bar{q}_T\}^{\mathrm{T}}[S]\{q_T\} - \delta\{\bar{q}_T\}^{\mathrm{T}}\{P_T\} = 0, \tag{4.15}$$

where δ is the first variation.

4.4 Wave Functions for Exterior Region

Wave functions required for the scattering problem are obtained by considering the elastic plane strain wave propagation in the corresponding cylindrical cross-section. The

Rayleigh-Ritz type approximation with displacement continuity at the nodal points (surfaces) is employed in the present study. The method divides the cross section into several sublayers as shown in Figure 4.4. Consider the k^{th} sublayer bounded by $r = r_{\text{k}}$ and $r = r_{\text{k+1}}$ surfaces. The nonvanishing displacement components u and v are approximated by interpolation polynomials in the radial direction as:

$$\{U\} = [N]\,\{\tilde{q}\} \tag{4.16}$$

where

$$\{\tilde{q}\}^{\text{T}} = \left\langle u^b \quad v^b \quad u^m \quad v^m \quad u^f \quad v^f \right\rangle, \tag{4.17}$$

$$[N] = \begin{bmatrix} n_1 & 0 & n_2 & 0 & n_3 & 0 \\ 0 & n_1 & 0 & n_2 & 0 & n_3 \end{bmatrix}. \tag{4.18}$$

The generalized displacements u^b, u^m, and u^f in equation (4.17) are taken at the back (inner), middle, and front (outer) nodal surfaces of the sublayer, respectively. The interpolation polynomials, $n_i (i = 1, 2, 3)$ are quadratic functions given by equation (2.28) as:

$$n_1 = 1 - 3\eta + 2\eta^2 \quad ; \quad n_2 = 4\eta - 4\eta^2 \quad ; \quad n_3 = -\eta + 2\eta^2 \quad , \tag{4.19}$$

where $\eta = (r - r_k)/h_k$, h_k being the thickness of the k^{th} sublayer.

The governing equation for the entire cylindrical cross section is obtained, by using Hamilton's principle, to be:

$$[K_1]\{\tilde{Q}\}'' + [K_2]\{\tilde{Q}\}' - [K_3]\{\tilde{Q}\} - [M]\{\ddot{\tilde{Q}}\} = 0. \tag{4.20}$$

The matrices $[K_1]$, $[K_2]$, $[K_3]$, and $[M]$ can be obtained from Appendix B with the wavenumber $\xi = 0$. It is noted that $[K_1]$, $[K_3]$, and $[M]$ are symmetric, and $[K_2]$ is anti-symmetric. The vector $\{\tilde{Q}\}$ contains the generalized coordinates for the cylinder. Prime and overdot denote differentiations with respect to θ and t, respectively.

A solution for equation (4.20) can be assumed in the form of:

$$\{\tilde{Q}\} = \{Q_0\} e^{-i(m\theta - \omega t)}, \tag{4.21}$$

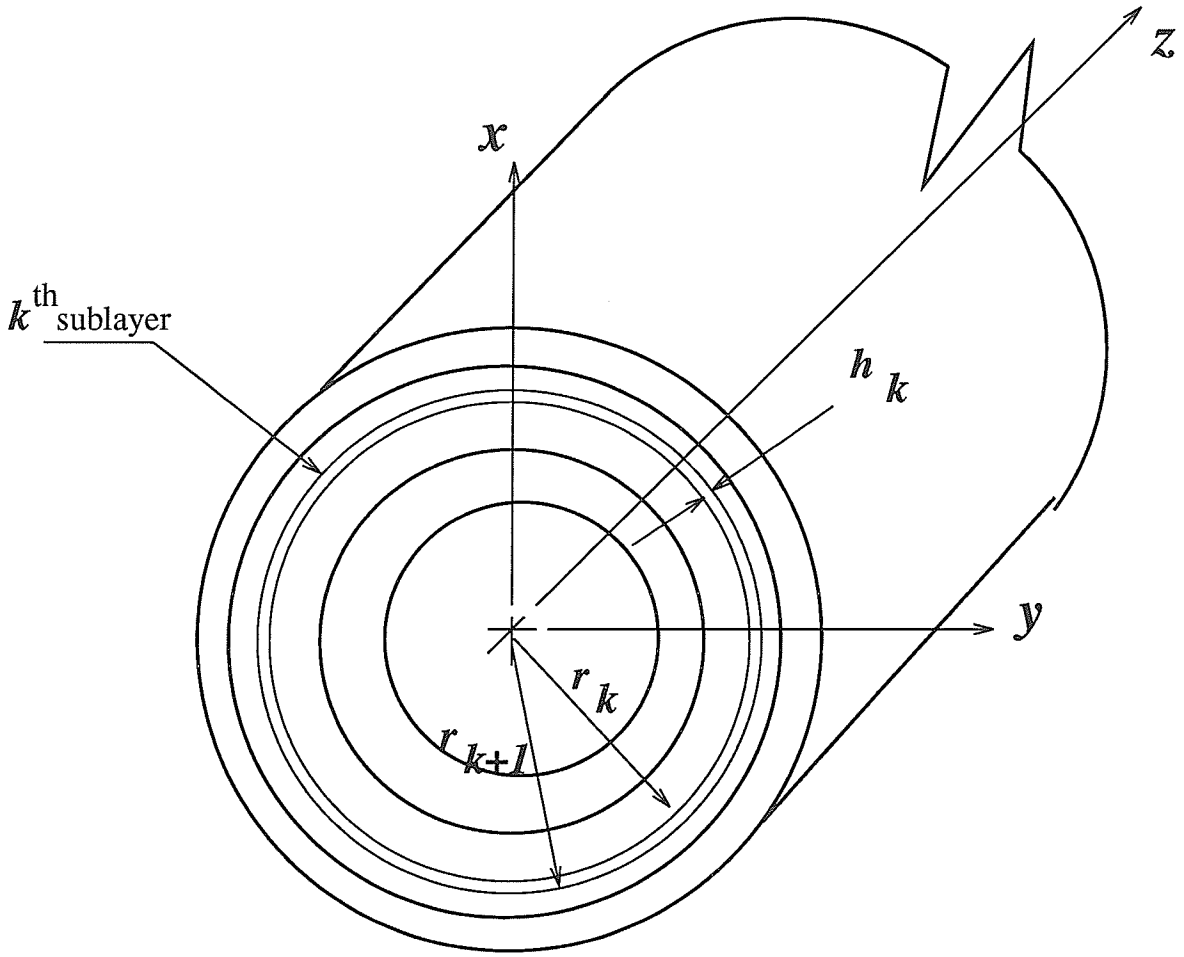

Figure 4.4: Discretization in Rayleigh-Ritz type approximation

where $\{Q_0\}$ represents the nodal amplitude vector, ω the circular frequency, and m the complex circumferential wavenumber. By substituting equation (4.21) into equation (4.20), the following set of linear homogeneous equations is obtained:

$$\Big\{-m^2[K_1] - im[K_2] - [K_3] + \omega^2[M]\Big\}\{Q_0\} = 0. \tag{4.22}$$

For nontrivial solution of $\{Q_0\}$, the determinant of the coefficient matrix must be zero. This results in quadratic algebraic eigenvalue problem. This equation serves as the dispersion relation to evaluate m for a given ω, or alternatively, ω for a specifed m.

The wave functions at discrete nodal points for the j^{th} mode, $\{q_j\}$, can be obtained from the j^{th} mode eigenvector of the equation (4.22) as:

$$\{q_j\}^{\mathrm{T}} = \Big\langle u_{1j} \quad v_{1j} \quad \ldots \quad u_{lj} \quad v_{lj} \quad \ldots \quad u_{(NP)j} \quad v_{(NP)j} \Big\rangle, \tag{4.23}$$

NP being the number of nodal points through the thickness.

4.5 Determination of Circumferential Wavenumber

Equation (4.20) obtained in section 4.4 serves as the dispersion relation of the cylinder in the form of quadratic algebraic eigenvalue problem. This equation can be used to evaluate the frequency, ω, for a given circumferential wavenumber, m, or alternately, for a specified ω, it can be solved for m. Only real ω are admissible due to physical reasons. The circumferential wavenumber, m, on the other hand, can have the form of a complex number as:

$$m = m_{\mathrm{R}} - im_{\mathrm{I}}, \tag{4.24}$$

where m_{R} and m_{I} are real and imagainary parts of the complex circumferential wavenumber, m, respectively. From the viewpoint of the stability of the system, only $m_{\mathrm{I}} \geq 0$ is admissible for $\theta > 0$. When $m_{\mathrm{I}} = 0$ and $m_{\mathrm{R}} > 0$, the roots produce modes propagating in the positive $\theta-$direction. The modes are non-propagating when $m_{\mathrm{R}} = 0$ and $m_{\mathrm{I}} > 0$.

The roots with non-zero m_{R} and m_{I} represent the evanescent modes. It can be shown that if m is a root of the dispersion relation, then $-\overline{m}$ is also a root. This illustrates that the waves may propagate in either the positive or the negative $\theta-$directions. It is also noted that the dispersion equation may produce an infinite number of roots of which only finite numbers are propagating modes. These propagating modes, the roots with real wavenumbers, carry energy. Non-propagating and evanescent modes carry no energy and their amplitudes exponentially decay with distance. However, these modes are as significant as the propagating modes in satisfying the boundary conditions.

4.6 Wave Functions Expansion for Scattered Fields

The scattered displacements vectors, $\{q^+_{R+}\}_{sc}$ and $\{q^+_{R-}\}_{sc}$; and the scattered stresses vectors, $\{S^+_{R+}\}_{sc}$ and $\{S^+_{R-}\}_{sc}$ in the exterior region represented by J modes wave functions expansion of the waves travelling in the positive $\theta-$direction at the boundaries R^+ and R^- are in the forms of, respectively:

$$\begin{aligned}
\{q^+_{R+}\}_{sc} &= \sum_{j=1}^{J} A^+_j \{q^+_j\} e^{-i(m_j\theta^+ - \omega t)}, \\
\{q^+_{R-}\}_{sc} &= \sum_{j=1}^{J} A^+_j \{q^+_j\} e^{-i[m_j(2\pi-\theta^-) - \omega t]}, \\
\{S^+_{R+}\}_{sc} &= \sum_{j=1}^{J} A^+_j \{S^+_j\} e^{-i(m_j\theta^+ - \omega t)}, \\
\{S^+_{R-}\}_{sc} &= -\sum_{j=1}^{J} A^+_j \{S^+_j\} e^{-i[m_j(2\pi-\theta^-) - \omega t]},
\end{aligned} \tag{4.25}$$

where

$$\begin{aligned}
\{q^+_j\}^{\mathrm{T}} &= \left\langle u^+_{1j} \quad v^+_{1j} \quad \ldots \quad u^+_{lj} \quad v^+_{lj} \quad \ldots \quad u^+_{(NP)j} \quad v^+_{(NP)j} \right\rangle, \\
\{S^+_j\}^{\mathrm{T}} &= \left\langle \sigma^+_{r\theta 1j} \quad \sigma^+_{\theta\theta 1j} \quad \ldots \quad \sigma^+_{r\theta lj} \quad \sigma^+_{\theta\theta lj} \quad \ldots \quad \sigma^+_{r\theta (NP)j} \quad \sigma^+_{\theta\theta (NP)j} \right\rangle.
\end{aligned} \tag{4.26}$$

The wave functions $\{q^+_j\}$ is the wave functions $\{q_j\}$ associated with the modes travelling in the positive $\theta-$direction. The stresses $\sigma^+_{r\theta lj}$ and $\sigma^+_{\theta\theta lj}$ at the l^{th} nodal points associated

with the j^{th} mode of wave travelling in the positive $\theta-$direction can be evaluated by using the stress-strain and the strain-displacement relations. The negative sign of $\{S^+_{R^-}\}_{sc}$ is for consistency with the finite element procedure. The dependence $e^{i\omega t}$ will be suppressed in the following formulation.

Similarly, the displacements vectors: $\{q^-_{R^+}\}_{sc}$ and $\{q^-_{R^-}\}_{sc}$; and the stresses vectors: $\{S^-_{R^+}\}_{sc}$ and $\{S^-_{R^-}\}_{sc}$ represented by J modes wave functions expansion of the waves travelling in the negative $\theta-$direction at the boundaries R^+ and R^-, respectively, are in the forms of:

$$\begin{aligned}
\{q^-_{R^+}\}_{sc} &= \sum_{j=1}^{J} A^-_j \{q^-_j\} e^{-im_j(2\pi-\theta^+)}, \\
\{q^-_{R^-}\}_{sc} &= \sum_{j=1}^{J} A^-_j \{q^-_j\} e^{-im_j\theta^-}, \\
\{S^-_{R^+}\}_{sc} &= -\sum_{j=1}^{J} A^-_j \{S^-_j\} e^{-im_j(2\pi-\theta^+)}, \\
\{S^-_{R^-}\}_{sc} &= \sum_{j=1}^{J} A^-_j \{S^-_j\} e^{-im_j\theta^-},
\end{aligned} \tag{4.27}$$

where

$$\begin{aligned}
\{q^-_j\} &= \left\langle u^+_{1j} \quad -v^+_{1j} \quad \dots \quad u^+_{lj} \quad -v^+_{lj} \quad \dots \quad u^+_{(NP)j} \quad -v^+_{(NP)j} \right\rangle, \\
\{S^-_j\} &= \left\langle \sigma^+_{r\theta 1j} \quad -\sigma^+_{\theta\theta 1j} \quad \dots \quad \sigma^+_{r\theta lj} \quad \sigma^+_{\theta\theta lj} \quad \dots \quad \sigma^+_{r\theta (NP)j} \quad \sigma^+_{\theta\theta (NP)j} \right\rangle.
\end{aligned} \tag{4.28}$$

After some algebraic manipulations, the scattered field at the boundaries R^+ and R^- represented by J modes wave functions expansion of the waves travelling in both positive and negative $\theta-$directions can be written as:

$$\begin{aligned}
\{q_{R^+}\}_{sc} &= \sum_{j=1}^{J} A^+_j \{q^+_j\} e^{-im_j\theta^+} + \sum_{j=1}^{J} A^-_j \{q^-_j\} e^{-im_j\theta^-} EM_j, \\
\{q_{R^-}\}_{sc} &= \sum_{j=1}^{J} A^+_j \{q^+_j\} e^{-im_j\theta^+} EM_j + \sum_{j=1}^{J} A^-_j \{q^-_j\} e^{-im_j\theta^-}, \\
\{S_{R^+}\}_{sc} &= \sum_{j=1}^{J} A^+_j \{S^+_j\} e^{-im_j\theta^+} - \sum_{j=1}^{J} A^-_j \{S^-_j\} e^{-im_j\theta^-} EM_j, \\
\{S_{R^-}\}_{sc} &= -\sum_{j=1}^{J} A^+_j \{S^+_j\} e^{-im_j\theta^+} EM_j + \sum_{j=1}^{J} A^-_j \{S^-_j\} e^{-im_j\theta^-}.
\end{aligned} \tag{4.29}$$

The complex amplitudes A_j^+ and A_j^- associated with the j^{th} mode of wave propagating in the positive and the negative $\theta-$ directions, respectively, are to be determined from the global solution which will be discussed in next section. EM_j in the above equations are defined as:

$$EM_j = e^{-2m_j\pi} e^{m_j(\theta^+ + \theta^-)}. \tag{4.30}$$

In constructing the nodal force vectors of the scattered field, consistent loads with quadratic stress distributions are employed. The stress at a point in the k^{th} sublayer are approximated by interpolation polynomials through the thickness of the sublayer as:

$$\sigma = \langle n_1 \quad n_2 \quad n_3 \rangle \{\sigma_N\}, \tag{4.31}$$

where

$$\{\sigma_N\}^{\mathrm{T}} = \left\langle \sigma^b \quad \sigma^m \quad \sigma^f \right\rangle, \tag{4.32}$$

and the interpolation polynomials $n_i \quad (i = 1, 2, 3)$ are defined in equation (4.19). The force vector $\{f\}$ can then be written as:

$$\{f\} = \int_{r_k}^{r_{k+1}} \sigma \, dr. \tag{4.33}$$

This, after the integration, results in the relations:

$$\{f\} = \begin{Bmatrix} f^b \\ f^m \\ f^f \end{Bmatrix} = \frac{h_k}{30} \begin{bmatrix} 4 & 2 & -1 \\ 2 & 16 & 2 \\ -1 & 2 & 4 \end{bmatrix} \begin{Bmatrix} \sigma^b \\ \sigma^m \\ \sigma^f \end{Bmatrix}. \tag{4.34}$$

Incorporation of equation (4.34) with the stresses vector in equation (4.29) yields the forces vectors $\{P_{R^+}\}_{sc}$ and $\{P_{R^-}\}_{sc}$ corresponding to the scattered fields represented by J mode wave functions expansion of the waves travelling in both the positive and the negative $\theta-$direction at the boundaries R^+ and R^-, respectively, as:

$$\begin{aligned} \{P_{R^+}\}_{sc} &= \sum_{j=1}^{J} A_j^+ \{f_j^+\} e^{-im_j\theta^+} - \sum_{j=1}^{J} A_j^- \{f_j^-\} e^{-im_j\theta^-} EM_j, \\ \{P_{R^-}\}_{sc} &= -\sum_{j=1}^{J} A_j^+ \{f_j^+\} e^{-im_j\theta^+} EM_j + \sum_{j=1}^{J} A_j^- \{f_j^-\} e^{-im_j\theta^-}. \end{aligned} \tag{4.35}$$

The first two equations of the equations (4.29) yield the displacement vector of the scattered wave field at the nodes on the boundaries R^+ and R^- as:

$$\left\{ \begin{array}{c} \{q_{R^+}\}_{sc} \\ \{q_{R^-}\}_{sc} \end{array} \right\} = \left[\begin{array}{cc} [G^+] & [GM^-] \\ [GM^+] & [G^-] \end{array} \right] \left\{ \begin{array}{c} \{D^+\} \\ \{D^-\} \end{array} \right\}, \tag{4.36}$$

where

$$\begin{aligned} [G^+] &= [\{q_1^+\} \ \{q_2^+\} \ \dots \ \{q_j^+\} \ \dots \ \{q_J^+\}], \\ [G^-] &= [\{q_1^-\} \ \{q_2^-\} \ \dots \ \{q_j^-\} \ \dots \ \{q_J^-\}], \\ [GM^+] &= [\{q_1^+ \, EM_1\} \ \{q_2^+ \, EM_2\} \ \dots \ \{q_j^+ \, EM_j\} \ \dots \ \{q_J^+ \, EM_J\}], \\ [GM^-] &= [\{q_1^- \, EM_1\} \ \{q_2^- \, EM_2\} \ \dots \ \{q_j^- \, EM_j\} \ \dots \ \{q_J^- \, EM_J\}], \end{aligned} \tag{4.37}$$

$$\begin{aligned} \{D^+\}^{\mathrm{T}} &= \left\langle D_1^+ \ \ D_2^+ \ \dots \ D_j^+ \ \dots \ D_J^+ \right\rangle, \\ \{D^-\}^{\mathrm{T}} &= \left\langle D_1^- \ \ D_2^- \ \dots \ D_j^- \ \dots \ D_J^- \right\rangle, \end{aligned} \tag{4.38}$$

$$\begin{aligned} D_j^+ &= A_j^+ e^{-im_j\theta^+}, \\ D_j^- &= A_j^- e^{-im_j\theta^-}, \end{aligned} \tag{4.39}$$

Similarly, equation (4.35) provides the force vector of the scattered wave field at the nodes on the boundaries R^+ and R^- as:

$$\left\{ \begin{array}{c} \{P_{R^+}\}_{sc} \\ \{P_{R^-}\}_{sc} \end{array} \right\} = \left[\begin{array}{cc} [F^+] & [FM^-] \\ [FM^+] & [F^-] \end{array} \right] \left\{ \begin{array}{c} \{D^+\} \\ \{D^-\} \end{array} \right\}, \tag{4.40}$$

where

$$\begin{aligned} [F^+] &= [\{f_1^+\} \ \{f_2^+\} \ \dots \ \{f_j^+\} \ \dots \ \{f_J^+\}], \\ [F^-] &= [\{f_1^-\} \ \{f_2^-\} \ \dots \ \{f_j^-\} \ \dots \ \{f_J^-\}], \\ [FM^+] &= [\{f_1^+ \, EM_1\} \ \{f_2^+ \, EM_2\} \ \dots \ \{f_j^+ \, EM_j\} \ \dots \ \{f_J^+ \, EM_J\}], \\ [FM^-] &= [\{f_1^- \, EM_1\} \ \{f_2^- \, EM_2\} \ \dots \ \{f_j^- \, EM_j\} \ \dots \ \{f_J^- \, EM_J\}], \end{aligned} \tag{4.41}$$

4.7 Determination of Amplitude Coefficients

The global solution is obtained by imposing the following continuity conditions on displacements and tractions at the boundary nodal points:

$$\begin{aligned} \{q_R\} &= \{q_R\}_{in} + \{q_R\}_{sc}, \\ \{P_R\} &= \{P_R\}_{in} + \{P_R\}_{sc}, \end{aligned} \tag{4.42}$$

where

$$\begin{aligned} \{q_R\}_{in}^{\mathrm{T}} &= \left\langle \{q_{R+}\}_{in}^{\mathrm{T}} \quad \{q_{R-}\}_{in}^{\mathrm{T}} \right\rangle, \\ \{q_R\}_{sc}^{\mathrm{T}} &= \left\langle \{q_{R+}\}_{sc}^{\mathrm{T}} \quad \{q_{R-}\}_{sc}^{\mathrm{T}} \right\rangle, \end{aligned} \tag{4.43}$$

$$\begin{aligned} \{P_R\}_{in}^{\mathrm{T}} &= \left\langle \{P_{R+}\}_{in}^{\mathrm{T}} \quad \{P_{R-}\}_{in}^{\mathrm{T}} \right\rangle, \\ \{P_R\}_{sc}^{\mathrm{T}} &= \left\langle \{P_{R+}\}_{sc}^{\mathrm{T}} \quad \{P_{R-}\}_{sc}^{\mathrm{T}} \right\rangle. \end{aligned} \tag{4.44}$$

The subscript *in* for displacement and force vectors represents those corresponding to the incident field. Note that the quantities on the left hand side of the equality in equation (4.42) are from the interior region whilst those on the right hand side correspond to the exterior region.

Substitution of equations (4.11) and (4.13) into equation (4.15) together with the incorporation of equation (4.42) results in:

$$\begin{aligned} \delta\{\bar{q}_I\}^{\mathrm{T}} & \left[[S_{II}]\{q_I\} + [S_{IR}](\{q_R\}_{sc} + \{q_R\}_{in})\right] \\ & + \delta\{\bar{q}_R\}_{sc}^{\mathrm{T}}\left[[S_{IR}]\{q_I\} + [S_{RR}](\{q_R\}_{sc} + \{q_R\}_{in})\right] \\ & - \delta\{\bar{q}_I\}^{\mathrm{T}}\{P_I\} - \delta\{\bar{q}_R\}_{sc}^{\mathrm{T}}(\{P_R\}_{sc} + \{P_R\}_{in}) = 0. \end{aligned} \tag{4.45}$$

Rewriting the above equation in view of the equations (4.36) and (4.40) yields the system of the following equations:

$$\begin{bmatrix} [S_{II}] & [S_{IR}][G] \\ [\bar{G}]^{\mathrm{T}}[S_{RI}] & [\bar{G}]^{\mathrm{T}}([S_{RR}][G] - [F]) \end{bmatrix} \begin{Bmatrix} \{q_I\} \\ \{D\} \end{Bmatrix} = \begin{Bmatrix} \{P_I\} - [S_{IR}]\{q_R\}_{in} \\ [\bar{G}]^{\mathrm{T}}\{P_R\}_{in} - [\bar{G}]^{\mathrm{T}}[S_{RR}]\{q_R\}_{in} \end{Bmatrix}, \tag{4.46}$$

where

$$[G] = \begin{bmatrix} [G^+] & [GM^-] \\ [GM^+] & [G^-] \end{bmatrix},$$
$$[F] = \begin{bmatrix} [F^+] & [FM^-] \\ [FM^+] & [F^-] \end{bmatrix}. \tag{4.47}$$

$$\{D\}^{\mathrm{T}} = \left\langle \{D^+\}^{\mathrm{T}} \quad \{D^-\}^{\mathrm{T}} \right\rangle. \tag{4.48}$$

4.7.1 Time Harmonic Line Load

Consider the interior region of the time harmonic line load bounded by the boundaries B^+ and B^- at $\theta = \beta^+$ and $\theta = 2\pi - \beta^-$, respectively. The subscripts R^+ and R^-, and the angles θ^+ and θ^- in all the above equations are replaced by B^+ and B^-, and β^+ and β^-, respectively. The displacement and the force vectors corresponding to the incident waves vanish and the equation (4.46) is reduced to:

$$\begin{bmatrix} [S_{II}] & [S_{IB}][G] \\ [\bar{G}]^{\mathrm{T}}[S_{BI}] & [\bar{G}]^{\mathrm{T}}([S_{BB}][G] - [F]) \end{bmatrix} \begin{Bmatrix} \{q_I\} \\ \{D\} \end{Bmatrix} = \begin{Bmatrix} \{P_I\} \\ \{0\} \end{Bmatrix}. \tag{4.49}$$

This results in two systems of linear equation as:

$$\{q_I\} = [S_{II}]^{-1}\{P_I\} - [S_{II}]^{-1}[S_{IB}][G]\{D\}, \tag{4.50}$$

$$[\bar{G}]^{\mathrm{T}}\Big[([S_{BB}] - [S_{BI}][S_{II}]^{-1}[S_{IB}])[G] - [F]\Big]\{D\} = -[\bar{G}]^{\mathrm{T}}[S_{IB}][S_{II}]^{-1}\{P_I\}. \tag{4.51}$$

The linear system of equations (4.51) can be solved for $\{D\}$ for the input loading $\{P_I\}$. Amplitudes A_j^+ and A_j^- are obtained from equations (4.39). The nodal displacements in the interior region $\{q_I\}$ are then calculated from equation (4.50).

4.7.2 Scattering due to Crack

Consider the interior region containing line crack bounded by the boundaries S^+ and S^- at $\theta = \theta_0 + \phi^+$ and $\theta = \theta_0 - \phi^-$, respectively. The incident fields for this problem are

in the forms of the equations (4.29) and (4.35) with (a) the replacement of θ^+ and θ^- by $\theta_0 + \phi^+$ and $2\pi - \theta_0 + \phi^-$, repectively, and (b) A_j^+ and A_j^- calculated from previous section. The problem is considered in a new coordinate system (r, θ', z) where θ' is located at $\theta = \theta_0$. With respect to this new coordinate system, the artificial boundaries S^+ and S^- are at $\theta' = \phi^+$ and $\theta' = 2\pi - \phi^-$, respectively. All of the equations derived, with the exception of those in section4.7.1, hold with the replacement of the subscripts R^+ and R^-, the angles θ^+ and θ^-, and the amplitudes A_j^+ and A_j^- by S^+ and S^-, ϕ^+ and ϕ^-, and C_j^+ and C_j^-, respectively. In this case, there is no internal force vector $\{P_I\}$ and the equation (4.46) becomes:

$$\begin{bmatrix} [S_{II}] & [S_{IS}][G] \\ [\bar{G}]^{\mathrm{T}}[S_{SI}] & [\bar{G}]^{\mathrm{T}}([S_{SS}][G] - [F]) \end{bmatrix} \begin{Bmatrix} \{q_I\} \\ \{D\} \end{Bmatrix} = \begin{Bmatrix} -[S_{IS}]\{q_S\}_{in} \\ [\bar{G}]^{\mathrm{T}}\{P_S\}_{in} - [\bar{G}]^{\mathrm{T}}[S_{SS}]\{q_S\}_{in} \end{Bmatrix}, \tag{4.52}$$

which leads to two systems of linear equation as:

$$\{q_I\} = -[S_{II}]^{-1}[S_{IS}]\{q_S\}_{in} - [S_{II}]^{-1}[S_{IS}][G]\{D\}, \tag{4.53}$$

$$\begin{aligned} [\bar{G}]^{\mathrm{T}}\Big[([S_{SS}] - [S_{SI}][S_{II}]^{-1} \quad & [S_{IS}])[G] - [F]\Big]\{D\} = \\ & [\bar{G}]^{\mathrm{T}}\Big[([S_{SI}][S_{II}]^{-1}[S_{IS}] - [S_{SS}])\{q_S\}_{in} + \{P_S\}_{in}\Big]. \end{aligned} \tag{4.54}$$

The incident fields $\{q_S\}$ and $\{P_S\}$ are obtained by employing the amplitudes calculated from equation (4.51) with appropriate angles $\theta_0 + \phi^+$ and $2\pi - \theta_0 + \phi^-$. $\{D\}$ for the scattered field is evaluated from the equation (4.54) and this leads to the calculation of the scattered amplitudes from equations (4.39). The nodal displacement vector for the interior region which contains cracks can be obtained from equation (4.53).

4.8 Numerical Results and Discussion

To validate and to assess the accuracy and the capability of the method, the numerical experimentation is performed for the Zr-Nb pressure tube. The isotropic elastic properties

of the Zr-Nb are given as (Mair and Earl 1990):

$$\begin{aligned} E &= 91GPa, \quad \rho = 6.48gm/ml, \\ \lambda &= 34GPa, \quad \mu = 74GPa. \end{aligned} \tag{4.55}$$

where E is the elastic modulus, λ and μ are the Lamè constants. The cylinder has the total thickness, H, and the inner radius r_{in} of $4.2mm$ and $51.7mm$, respectively. The frequency spectrum for this cylinder - the plot between the circumferential wavenumber and the frequency, is illustrated in Figure 4.5. In the figure, Ω is non-dimensionalized frequency and is defined as:

$$\Omega = \frac{\omega H}{v_s},$$

where v_s is the shear wave velocity calculated from:

$$v_s = \sqrt{\frac{\mu}{\rho}}.$$

The frequency spectrum in Figure 4.5 is shown only for the propagating modes. It can be noticed that the real circumferential wavenumbers need not be integer. This is because the complete circular cross section is considered as a multiply-connected body (Timoshenko and Goodier 1970), that is, a body such that some sections can be cut clear across without dividing the body into two parts. Because of the non-integer wavenumbers condition, the multi-valued solutions will be obtained. To avoid such multi-valued solutions, the condition of single-valued displacements and stresses is imposed, that is, only $0 \leq \theta < 2\pi$ is considered in all calculations.

Two loading cases are considered in this study as shown in Figure 4.6. The normalized amplitude of the each harmonic load is taken as unity. For the cracked cross section, the crack size investigated in this study is 1/10 of the total thickness of the cylinder. The location of the crack is at $\theta = 120^o$. The numerical results for each case are illustrated for $\Omega = 1.00$ which has two propagating modes. The cylinder is divided into 10 sub-layers for the wave function determination and 60 nine-noded elements are employed in the finite element modelling for the interior region. Tables 4.1 and 4.2 illustrates the numerical experimentations for vertical loading while Tables 4.3 and 4.4 show the results

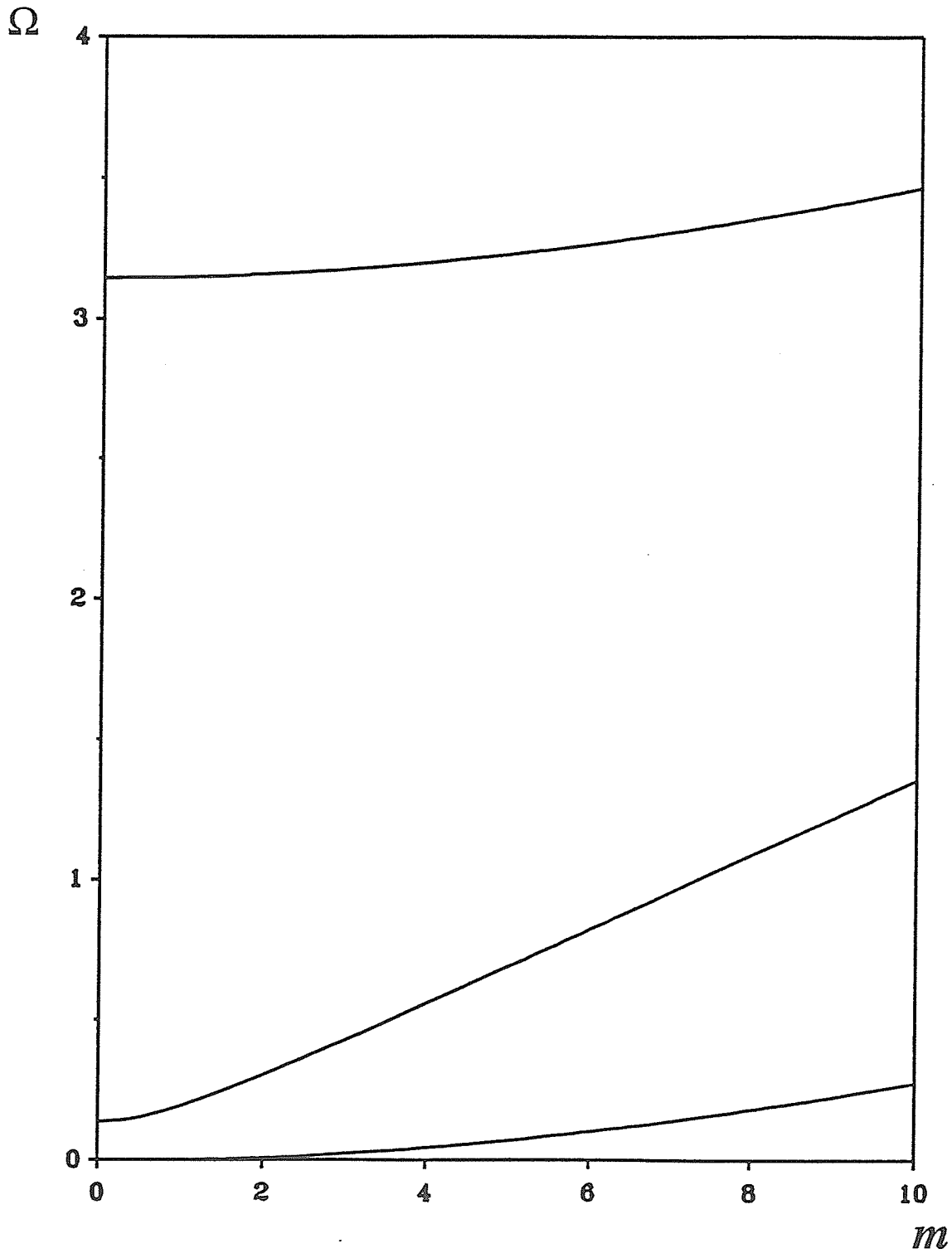

Figure 4.5: Frequency spectrum for Zr-Nb tube

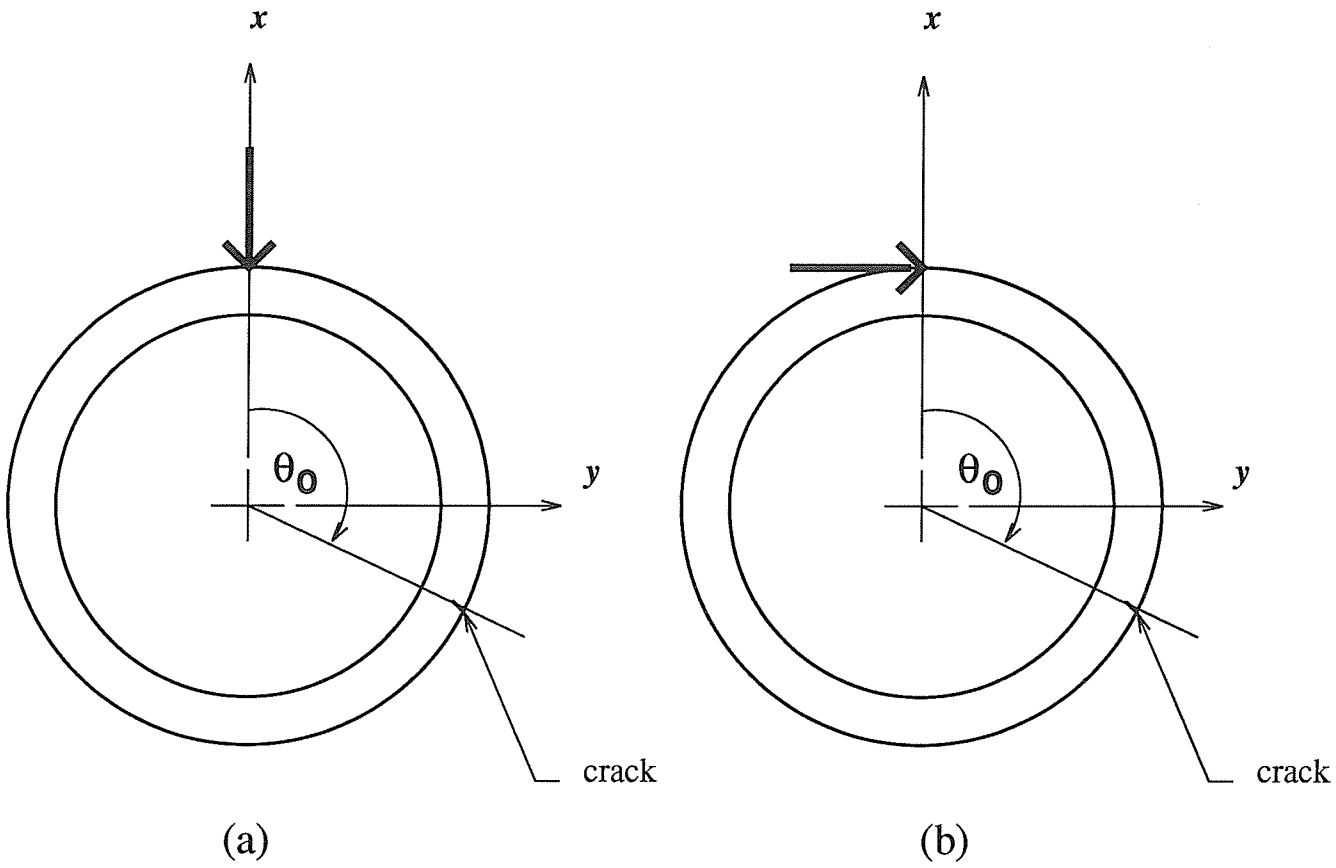

Figure 4.6: Two loading cases considered:
(a) vertical line load and (b) horizontal line load.

for horizontal loading. Three, five, and seven modes expansion (two propagating modes) are employed in the investigation. The comparison of the results shows the convergence of the results.

Tables 4.1 and 4.3 demonstrate the complex amplitudes and the normalized energy fluxes associated with the scattered fields produced by the vertical and the horizontal loads, respectively, in the uncracked cross-section. In the tables, E_{sc} and E_{in} are the energy fluxes from the scattered fields and the input load, respectively. It can be seen from Table 4.1 that the amplitudes associated with the scattered fields for the vertical load case are equal and in-phase for both boundaries of the interior region. This is expected because the problem is symmetric. For the case of horizontal loading (Table 4.3), however,

the amplitudes at one boundary are 180^o out-of-phase of those at another boundary of the interior region since the problem considered is anti-symmetric. The normalized energy fluxes from each boundary are identical and the total sum from both boundaries is unity. This demonstrates that the energy from the input load is divided into two equal parts and propagate through both boundaries of the interior region. On the other hand, the principle of energy conservation holds.

When the waves produced by the load travel along the circumferential direction and strike a flaw, scattering occur. The numerical experimentations show the amplitudes associated with the scattered fields (not reported herein) for the uncracked cross-section are negligible in comparison with those produced by the loads. With the presence of the crack, the amplitudes associated with the scattered fields are illustrated in Tables 4.2 and 4.4 for the vertical and the horizontal load cases, respectively. It is noticed that although the complex amplitudes of the propagating modes associated with the scattered fields differ in phases, the magnitudes are the same. This indicates that when the detector probe is placed either on the left or right of the crack or load with the same distance from the crack or load, the same magnitudes will always be detected. However, the phases of the two waves will be different.

4.9 Concluding Remarks

The hybrid method is employed to solve the scattering problem of time harmonic elastic plane strain waves in a cylinder. The load or crack is bounded by the interior region which is modelled by the finite element. The exterior region are represented by the wave function expansion. The hybrid method incorporates the interior region and the exterior region using the continuity at the boundaries between the two regions. Unlike the plate problem where the incident waves only propagate in one direction, the incident waves in a cylindrical cross-section travel in both directions. The numerical experimentations

mode	A^+	A^-	$\|A\|$	E^+_{sc}/E_{in}	E^-_{sc}/E_{in}
1	$(0.0113, -.0175)$	$(0.0113, -.0175)$	0.0208	0.00002	0.00002
2	$(-.8940, 1.1059)$	$(-.8940, 1.1059)$	1.4220	0.49610	0.49610
3	$(1.4030, 0.0000)$	$(1.4030, 0.0000)$	1.4030	0.00000	0.00000
4	$(0.3028, -.3137)$	$(0.3028, -.3137)$	0.4360	–	–
5	$(0.3028, 0.3137)$	$(0.3028, 0.3137)$	0.4360	–	–
6	$(0.1648, -.2434)$	$(0.1648, -.2434)$	0.2940	–	–
7	$(0.1648, 0.2434)$	$(0.1648, 0.2434)$	0.2940	–	–

Table 4.1: Amplitudes and energy for scattered fields produced by vertical load at $\Omega = 1.0$ for uncracked cross-section.

mode	A^+	A^-	$\|A\|$
1	$(1.0254 \times 10^{-2}, -1.5916 \times 10^{-2})$	$(1.0256 \times 10^{-2}, -1.5915 \times 10^{-2})$	0.0189
2	$(2.9561 \times 10^{-2}, -3.6594 \times 10^{-2})$	$(2.9585 \times 10^{-2}, -3.6575 \times 10^{-2})$	0.0470
3	$(-5.2573 \times 10^{-2}, 0.0000)$	$(-5.2592 \times 10^{-2}, 0.0000)$	–
4	$(2.3099 \times 10^{-2}, 5.8217 \times 10^{-2})$	$(2.3067 \times 10^{-2}, 5.8435 \times 10^{-2})$	–
5	$(2.3099 \times 10^{-2}, -5.8217 \times 10^{-2})$	$(2.3067 \times 10^{-2}, -5.8435 \times 10^{-2})$	–
6	$(3.0341 \times 10^{-2}, 5.1948 \times 10^{-2})$	$(3.5920 \times 10^{-2}, 5.2519 \times 10^{-2})$	–
7	$(3.0341 \times 10^{-2}, -5.1948 \times 10^{-2})$	$(3.5920 \times 10^{-2}, -5.2519 \times 10^{-2})$	–

Table 4.2: Amplitudes of scattered fields due to crack at $\theta = 120^o$ from vertical load ($\Omega = 1.0$).

mode	A^+	A^-	$\|A\|$	E^+_{sc}/E_{in}	E^-_{sc}/E_{in}
1	$(0.7084, 0.4564)$	$(-.7084, -.4564)$	0.8427	0.0905	0.0905
2	$(0.5651, 0.4568)$	$(-.5651, -.4568)$	0.5267	0.4138	0.4138
3	$(1.3438, 0.0000)$	$(-1.3438, 0.0000)$	1.3438	0.0000	0.0000
4	$(0.3300, 0.1996)$	$(-.3300, -.1996)$	0.3857	–	–
5	$(0.3300, -.1996)$	$(-.3300, 0.1996)$	0.3857	–	–
6	$(0.2385, 0.0094)$	$(-.2385, -.0094)$	0.2565	–	–
7	$(0.2385, -.0094)$	$(-.2384, 0.0094)$	0.2565	–	–

Table 4.3: Amplitudes and energy for scattered fields produced by horizontal load at $\Omega = 1.0$ for uncracked cross-section.

mode	A^+	A^-	$\|A\|$
1	$(-3.3579 \times 10^{-3}, 5.2139 \times 10^{-3})$	$(-3.3598 \times 10^{-3}, 5.2122 \times 10^{-3}$	0.0062
2	$(-9.6976 \times 10^{-3}, 1.2038 \times 10^{-2})$	$(-9.7377 \times 10^{-3}, 1.2005 \times 10^{-2})$	0.0155
3	$(-1.7281 \times 10^{-2}, 0.0000)$	$(-1.7314 \times 10^{-2}, 0.0000)$	–
4	$(-7.6097 \times 10^{-3}, -1.8910 \times 10^{-2})$	$(-7.5525 \times 10^{-3}, -1.9278 \times 10^{-2})$	–
5	$(-7.6097 \times 10^{-3}, 1.8910 \times 10^{-2})$	$(-7.5525 \times 10^{-3}, 1.9278 \times 10^{-2})$	–
6	$(-7.8997 \times 10^{-3}, -1.7395 \times 10^{-2})$	$(-1.7079 \times 10^{-2}, -1.8350 \times 10^{-2})$	–
7	$(-7.8997 \times 10^{-3}, 1.7395 \times 10^{-2})$	$(-1.7079 \times 10^{-2}, 1.8350 \times 10^{-2})$	–

Table 4.4: Amplitudes of scattered fields due to crack at $\theta = 120^o$ from horizontal load ($\Omega = 1.0$).

for the Zr-Nb pressure tube verify the accuracy and the applicability of the method. Although the results are presented for only isotropic cylinder, the method presented in this chapter can also be used for laminated composite case.

Chapter 5

Conclusions and Recommendations

5.1 General Concluding Remarks

Three models of wave propagation in cylinders are developed in Chapter 2. Systematic numerical experimentations are performed to investigate the dispersion characteristics of cylinders and the factors effecting wave propagation in cylinders. The propagator matrix method, based on three-dimensional elastic theory, can be used to obtain accurate predictions of theoretical dispersion characteristics of laminated isotropic cylinders with arbitrary number of layers. For laminated composite cylinders where the analytical formulation is not possible, the displacement based and the displacement and stress based Rayleigh-Ritz type approximations are developed. The numerical results obtained by these approximations reveal excellent agreement with the analytical method for the laminated isotropic cases. The investigation on dispersion behaviors of laminated cylinders shows that the variations in circumferential wavenumber, thickness to radius ratio, and degree of anisotropy have influences on dispersion characteristics of cylinders. It is found that rigid body motion does not exist for circumferential wavenumbers higher than zero. The effects of the change in circumferential wavenumber are localized mostly in the low

wavenumbers regime and these effects are stronger in thick cylinders. The variation in the thickness to radius ratio has an influence on cut-off frequencies and degree of coupling. When the ratio decreases, the degree of coupling increases. The anisotropy, caused by the orientation of fibres with respect to the direction of wave propagation or by the number of layers, has a strong influence on dispersion characteristics of cylinders. It is found that measurable changes in phase velocity are caused by increasing the degree of anisotropy. The numerical experimentations also reveal that it is sufficient to employ only the displacement based Rayleigh-Ritz type approximation to study wave scattering problems.

The wave functions expansion is used to investigate the reflection of guided wave at a free end of a laminated cylinder with an arbitrary number of laminae in chapter 3. The results illustrate the applicability of the displacement based Rayleigh-Ritz type approximation in the study of the free end reflection problem in laminated composite cylinders. It is found that, when the circumferential wavenumber is not zero in composite cylinders, the wavenumbers of the waves propagating in the positive axial direction differ from that of the waves travelling in the negative axial direction. This finding is very essential in the study of wave scattering problems in composite cylinders. The numerical results show that the least square technique as well as the variational method can be applied for the free end reflection of guided waves in laminated isotropic cylinders. For laminated composite cylinders, however, the least square technique demonstrates anomalous results. The least square method should then be used with caution for reflection problems.

The hybrid method, presented in Chapter 4, shows the sucessful application to study plane strain wave scattering due to a flaw in a cylindrical cross-section. Although the numerical experimentation is performed only for an isotropic cross-section, the method can be applied for a laminated cross-section with general anisotropic layers. It is found that the circumferential wavenumber can be complex. The numerical investigation reveals that the magnitudes associated with the scattered propagating waves detected at

the same distance on either side of a particular load or flaw are always the same regardless of the phase differences. It is noted, however, that the scattering problem considered in the thesis is a highly idealised one. In order that the technique be useful for practical applications, a considerable amount of experimental work and additional theoretical study is required.

5.2 Recommendations for Future Work

The following recommendations are made for futuer work.

1. The scope of this thesis is confined to the development of computationally efficient models to study wave propagation and scattering problems in laminated composite cylinders. An experimentation program should be carried out to validate the theoretical findings of the present study.

2. The numerical experimentations performed in the thesis are in low frequencies region, more numerical works should be carried out to verify the applicability and the efficacy in high frequencies regime.

3. The plane strain wave propagation in circular cross-section needs to be thoroughly investigated both in theory and in experimental work in order to improve the efficiency of the hybrid method in plane strain wave scattering problem.

4. The hybrid method should be extended to the three dimensional scattering problem in the cylinder.

References

Achenbach, J.D., Adler, L., Lewis, D.K., and McMaken, H. 1979. Diffraction of Ultrasonic Waves by Penny-shaped Cracks in Metals. *J. Acoust. Soc. Am.*, **66(6)**, 1848-1856.

Abduljabbar, Z., Datta, S.K., and Shah, A.H. 1983. Diffraction of Horizontally Polarized Shear Waves by Normal Edge Cracks in Plate. *J. Appl. Physics.*, **52(2)**, 461-472.

Armenàkas, A.E. 1965. Torsional Waves in Composite Rods. *J. Acoust. Soc. Am.*, **38**, 439-446.

Armenàkas, A.E. 1967. Propagation of Harmonic Waves in Composite Circular Cylindrical Shells. Part-I Theorectical Investigation. *AIAA Journal.*, **5**, 740-744.

Armenàkas, A.E. 1971. Propagation of Harmonic Waves in Composite Circular Cylindrical Shells. Part-II Numerical Analysis. *AIAA Journal.*, **9**, 599-605.

Armenàkas, A.E., Gazis, D.C., and Herrmann, G. 1969. Free Vibration of Circular Cylindrical Shells. *Pergamon Press.* Oxford.

Barbero, E.J., Reddy, J.N., and Teply, J.L. 1990. General Two-dimensional Theory of

Laminated Cylindrical Shells. *AIAA Journal.*, **28(3)**, 544-553.

Bond, L.J. and Punjani, M. 1984. New Multitransducer Techniques for Crack Characterisation. *Proc. 10th Annual Review of Progress in Quantitative NDE.* Thompson, D.O. and Chimenti, D.E. (Eds.), Santa Cruz, CA., U.S.A., 297-307.

Braga, A.M.B., Barbone, P.E., and Herrmann, G. 1990. Wave Propagation in Fluid-loaded Laminated Cylindrical Shells. *Appl. Mech. Reviews.*, **43(5)**, Part 2.

Broutman, L.J. and Krock, R.H. 1974. Composite Materials: Engineering Applications of Composites. *3*, Noton, B.R. (Ed.), *Academic Press, Inc.*, New York.

Coffey, J.M. and Chapman, R.K. 1983. OECD/IAEA Specialist Meeting on *Defect Detection and Sizing.* **11**, 445.

Datta, S.K. , Ledbetter, H.M., and Kritz, R. 1984. Calculated Elastic Constants of Composites Containing Anisotropic Fibers. *Int. J. Solids Struct.*, **20(5)**, 429-438.

Dietz, A.G.H. 1965. Composite Materials. 1965 Edger Marburg Lecture. *American Society for Testing and Materials*, Philadelphia, Pa.

Dolbey, M.P., 1986. Cigar an Automated Inspecction System for CANDU Reactor. *8th International Conference on NDE in the Nuclear Industry.* Sponsored by ASM, Orlando, Florida, 105-111.

Frederick, J.R. 1965. Ultrasonic Engineering. *John Wiley & Son, Inc.*, New York.

Gasiz, D.C. 1959. Three-dimensional Investigation of the Propagation of Waves in Hollow Circular Cylinders. I-Analytical Foundation. II-Numerical Results. *J. Acoust. Soc.*

Am., **31(5)**, 568-578.

Golan, S., Adler, L., Cook, K.V., Nanstad, R.K., and Boland, T.K. 1980. Ultrasonic Diffraction Technique for Characterization of Fatigue Cracks. *J. Nondestr. Eval.*, **1(1)**, 11-19.

Gregory, R.D. and Cladwell, I. 1989. Axisymmetric Waves in a Semi-infinite Elastic Rod. *J. Appl. Math.*, **42**, 327-337.

Huang, K.H. and Dong, S.B. 1984. Propagating Waves and Edge Vibrations in Anisotropic Composite Cylinders. *J. Sound. Vib.*, **96(3)**, 363-379.

Hull, D. 1981. An Introduction to Composite Materials (Cambridge Solid State Science Series). *Cambridge University Press.* Great Britain.

Hutchins, D.A. and Moles, M.D.C. 1991. A Hybrid Method for Sizing Radial Cracks in Pressure Tubes. *Nondestr. Test. Eval.*, **6**, 25-44.

IMSL Library. 1984. Fortran Subroutine for Mathematics and Statistics. Edition 9.2, *IMSL Inc.*, Texas.

Jai-Lue Lai. 1971. Propagation of Harmonic Waves in Composite Elastic Cylinder. *J. Acoust. Soc. Am.*, **49**, 220-228.

Jones, R.M. 1975. Mechanics of Composite Materials. *McGraw-Hill Book Co.*, New York.

Karunasena, W.M. 1992. Elastic Waves in Laminated Composite Plates for Application in Ultrasonic Nondestructive Evaluation. *Ph.D. Dissertation.* University of Manito-

ba, Winnipeg, Manitoba, Canada.

Karunasena, W.M., Shah, A.H., and Datta, S.K. 1991. Plane Strain Wave Scattering by Cracks in Laminated Composite Plates. *J. Engng. Mech.*, ASCE, **117(8)**, 1738-1754.

Kim, Y.Y. and Steele, C.R. 1989. End Effects and Time-harmonic Longitudinal Wave Propagation in a Semi-infinite Solid Cylinder. *ASME J. Appl. Mech.*, **56**, 334-346.

Kohl, T., Datta, S.K., Shah, A.H., and Rattanawangcharoen, N. 1992. Mode-Coupling of Waves in Laminated Tubes. *J. Comp. Mat.*, **26(5)**, 661-682.

Koshiba, M., Karakida, S., and Suzuki, M. 1984. Finite-element Analysis of Lamb Wave Scattering in an Elastic Plate Waveguide. *IEEE Trans. Sonics. Ultrason.*, **SU-31**, 18.

Mair, H.D. and Earl, C.F. 1990. Zr-25% Nb Pressure Tube Ultrasonic Data. *Ontario Hydro Research Division*, Report No. 90-247-P, Toronto, Canada.

Mason. 1968. Guided Wave Propagation in Elongated Cylinders and Plates. *Physical Acoustics*, **1**, Part A, Meeker, T.R. and Meitzler, A.H. (Eds.), 111-167.

McGonnagle, W.J. 1961. Nondestructive Testing. *Gordon and Breach, Sceince Publishers, Inc.*, New York.

McNiven, H.D. 1961. Extensional Waves in a Semi-infinite, Elastic Rod. *J. Acoust. Soc. Am.*, **33**, 23-27.

McNiven, H.D., Sackman, J.L., and Shah, A.H. 1963. Dispersion of Axially Symmetric Waves in Composite, Elastic Rods. *J. Acoust. Soc. Am.*, **35**, 1602-1609.

McNiven, H.D. and Shah, A.H. 1967. The Influence of the End Mode on the Resonant Frequencies of Finite, Hollow, Elastic Rods. *J. Sound. Vib.*, **6**, 8-19.

Mindlin, R.D. 1960. Wave and Vibrations in Isotropic, Elastic Solids. *Proc. 1st Symp. Naval Structural Mech.*, Goodier, J.N. and Hoff, N. (Eds.), Pergamon Press, 199-232.

Moore, I.D. 1990. Vibration of Elastic and Viscoelastic Tubes. I-Harmonic Response. *J. Engng. Mech.*, **116(4)**, 928-942.

Muller, D.E. 1956. A Method for Solving Algebraic Equations Using an Automatic Computer. *Mathematical Tables and Aids to Computation*, **10**, 208-215.

National Bureau of Standards. 1964. Handbook of Mathematical Functions with Formulas, Graphs, and Mathematical Tables. Abramowitz, M. and Stegun, I.A. (Eds.), *Applire Mathematics Series 55*, Washington D.C.

Nelson, R.B., Dong, S.B., and Kalra, R.D. 1971. Vibrations and Waves in Laminated Orthotropic Circular Cylinders. *J. Sound. Vib.*, **18(3)**, 429-444.

Oliver, J. 1957. Elastic Wave Dispersion in a Cylindrical Rod by a Wide-band, Short-duration Pulse Technique. *J. Acoust. Soc. Am.*, **29**, 189-194.

Onoe, M., McNiven, H.D., and Mindlin, R.D. 1962. Dispersion of Axially Symmetric Waves in Elastic Rods. *ASME J. Appl. Mech.*, **29**, 729-734.

Pochhammer, L. 1876. Ueber die fortpflanzungsgeshwindigkieten schwingungen in einem unbegrenzten isotropen kreiscylinder. *Zeitschrift fur Mathematik.*, **81**, 324-336.

Silk, M.G. 1977. Research Techniques in Nodestructive Testing: Sizing Crack-like Defects

by Ultrasonic Means. **3**, Sharp, R.S. (Ed.), *Academic Press*, NY, 51-99.

Sun, C.T. and Whitney, J.M. 1974. Axisymmetric Vibrations of Laminated Composite Cylindrical Shells. *J. Acoust. Soc. Am.*, **55(6)**, 1238-1246.

Timoshenko, S.P. and Goodier, J.N. 1970. *Theory of Elasticity.* 3rd Ed., McGraw-Hill.

Tittman, B.R. 1975. Mode Conversion and Angular Dependence for Scattering from Voids in Solids. *Trans. Sonics. Ultrason.*, **SU-23(3)**, 111.

Tsai, J. and Roy, B.N. 1971. Axisymmetric Vibration of Finite Heterogenous Cylindrical Shells. *J. Sound. Vib.*, **17(1)**, 83-94.

Walfram, S. 1988. *Mathematica, A System of Doing Mathematics by Computers.* Addison-Wesley Publishing Company, Inc., The Advanced Book Program.

Wu, C.H. and Punkett, R. 1967. On the Solutions of Plates, Strips, Rods and Cylinders Subjected to Arbitrary Dynamic Edge Load. *SIAM J. Appl. Math.*, **15**, 107-119.

Zemanek. 1972. An Experimental and Theoretical Investigation of Elastic Wave Propagation in a Cylinder. *J. Acoust. Soc. Am.*, **51(1)**, 265-283.

Zienkiewick, O.C. 1977. *The Finite Element Method.* 3rd Ed., McGraw-Hill.

Appendix A

Propagator Matrix

Defining:

$$
\begin{aligned}
C_k(1,1) &= \frac{m}{r}Z_m(\alpha r) - \alpha Z_{m+1}(\alpha r),\\
C_k(1,2) &= \xi Z_{m+1}(\beta r),\\
C_k(1,3) &= \frac{im}{r}Z_m(\beta r),\\
C_k(2,1) &= \frac{im}{r}Z_m(\alpha r),\\
C_k(2,2) &= -i\xi Z_{m+1}(\beta r),\\
C_k(2,3) &= \beta Z_{m+1}(\beta r) - \frac{m}{r}Z_m(\beta r),\\
C_k(3,1) &= -i\xi Z_m(\alpha r),\\
C_k(3,2) &= -i\beta Z_m(\beta r),\\
C_k(3,3) &= 0,\\
C_k(4,1) &= \mu\Big\{\Big(\frac{2m(m-1)}{r^2} + (\xi^2-\beta^2)\Big)Z_m(\alpha r) + \frac{2\alpha}{r}Z_{m+1}(\alpha r)\Big\}, \qquad \text{(A.1)}\\
C_k(4,2) &= 2\mu\xi\Big\{\beta Z_m(\beta r) - \frac{(m+1)}{r}Z_{m+1}(\beta r)\Big\},\\
C_k(4,3) &= \frac{2i\mu m}{r}\Big\{\frac{(m-1)}{r}Z_m(\beta r) - \beta Z_{m+1}(\beta r)\Big\},\\
C_k(5,1) &= \frac{2i\mu m}{r}\Big\{\frac{(m-1)}{r}Z_m(\alpha r) - \alpha Z_{m+1}(\alpha r)\Big\},
\end{aligned}
$$

$$
\begin{aligned}
C_k(5,2) &= i\mu\xi\Big\{\frac{2(m+1)}{r}Z_{m+1}(\beta r) - \beta Z_m(\beta r)\Big\},\\
C_k(5,3) &= \mu\Big\{\Big(\beta^2 - \frac{2m(m-1)}{r^2}\Big)Z_m(\beta r) - \frac{2\beta}{r}Z_{m+1}(\beta r)\Big\},\\
C_k(6,1) &= 2i\mu\xi\Big\{\alpha Z_{m+1}(\alpha r) - \frac{m}{r}Z_m(\alpha r)\Big\},\\
C_k(6,2) &= i\mu\Big\{\Big(\beta^2 - \xi^2\Big)Z_{m+1}(\beta r) - \frac{\beta m}{r}Z_m(\beta r)\Big\},\\
C_k(6,3) &= \frac{\mu m\xi}{r}Z_m(\beta r).
\end{aligned}
$$

The elements of matrix $[D_k]$ given in equation (2.9) are:

$$
D_k(i,j) = C_k(i,j) \qquad i = 1,\ldots,6\ ;\ j = 1,\ldots,3\ ; \tag{A.2}
$$

where Z_m and Z_{m+1} are $H_m^{(1)}$ and $H_{m+1}^{(1)}$, respectively, and $r = r_k$. The other three columns, i.e, $j = 4,\ldots,6$, can be obtained from the first three columns by replacing the Hankel functions $H_m^{(1)}$ and $H_{m+1}^{(1)}$ by $H_m^{(2)}$ and $H_{m+1}^{(2)}$, respectively.

The elements of three by three matrices $[R]$ and $[T]$ in equation (2.19) are:

$$
\begin{aligned}
R(i,j) &= C_k(i,j),\\
T(i,j) &= C_k(i+3,j), \qquad i = 1,\ldots,3\ ;\ j = 1,\ldots,3\ ;
\end{aligned} \tag{A.3}
$$

where Z_m and Z_{m+1} denote J_m and J_{m+1}, repectively, and $r = r_1$.

Appendix B

Displacement Based Rayleigh-Ritz Type Approximation

The matrices $[M]$, $[K_1]$, $[K_2]$, and $[K_3]$ in equation (2.30) are defined as:

$$\begin{aligned}
[M] &= \int_0^H \rho\,[N]^{\mathrm{T}}\,[N]\,r dr, \\
[K_1] &= \int_0^H [\,b\,]^{\mathrm{T}}\,[C]\,[\,b\,]\,r dr, \\
[K_2] &= \int_0^H \Big[[\,b\,]^{\mathrm{T}}\,[\,C\,]\,[\,a\,] - [\,\bar{a}\,]^{\mathrm{T}}\,[\,C\,]\,[\,b\,]\Big] r dr, \\
[K_3] &= \int_0^H [\,\bar{a}\,]^{\mathrm{T}}\,[\,C\,]\,[\,a\,]\,r dr,
\end{aligned} \tag{B.1}$$

The non-zero elements of 6×9 matrix $[\,a\,]$ in equation (B.1) are as follows:

$$\begin{aligned}
a(1,1) &= n_1', & a(2,5) &= im\tfrac{n_2}{r}, \\
a(1,4) &= n_2', & a(2,7) &= \tfrac{n_3}{r}, \\
a(1,7) &= n_3', & a(2,8) &= im\tfrac{n_3}{r}, \\
a(2,1) &= \tfrac{n_1}{r}, & a(4,3) &= im\tfrac{n_1}{r}, \\
a(2,2) &= im\tfrac{n_1}{r}, & a(4,6) &= im\tfrac{n_2}{r}, \\
a(2,4) &= \tfrac{n_2}{r}, & a(4,9) &= im\tfrac{n_3}{r},
\end{aligned} \tag{B.2}$$

$$
\begin{aligned}
a(5,3) &= n_1', & a(6,4) &= im\tfrac{n_2}{r}, \\
a(5,6) &= n_2', & a(6,5) &= n_2' - \tfrac{n_2}{r}, \\
a(5,9) &= n_3', & a(6,7) &= im\tfrac{n_3}{r}, \\
a(6,1) &= im\tfrac{n_1}{r}, & a(6,8) &= n_3' - \tfrac{n_3}{r}, \\
a(6,2) &= n_1' - \tfrac{n_1}{r}, &&
\end{aligned}
\tag{B.3}
$$

where prime denotes the differentiation with respect to z.

The non-zero elements of 6×9 matrix $[\, b \,]$ in equation (B.1) are as follows:

$$
\begin{aligned}
b(3,3) &= b(4,2) = b(5,1) = n_1, \\
b(3,6) &= b(4,5) = b(5,4) = n_2, \\
b(3,9) &= b(4,8) = b(5,7) = n_3.
\end{aligned}
\tag{B.4}
$$

Appendix C

Displacement and Stress Based Rayleigh-Ritz Type Approximation

The non-zero elements of 3×12 matrices $[N_1]$ and $[N_2]$ of equation (2.33) are as follows:

$$\begin{aligned} N_1(1,3) &= \tfrac{f_2 P_3}{\Delta}, & N_1(3,1) &= -f_2, \\ N_1(1,5) &= \tfrac{f_2 P_2}{\Delta}, & N_1(3,3) &= \tfrac{f_2 P_9}{\Delta}, \\ N_1(2,3) &= \tfrac{f_2 P_6}{\Delta}, & N_1(3,5) &= \tfrac{f_2 P_8}{\Delta}. \\ N_1(2,5) &= \tfrac{f_2 P_5}{\Delta}, \end{aligned} \tag{C.1}$$

$$\begin{aligned} N_2(1,1) &= f_1 + \tfrac{f_2 P_1}{\Delta r_k}, & N_2(2,4) &= \tfrac{f_2 \Delta_{33}}{\Delta}, \\ N_2(1,2) &= \tfrac{f_2 \Delta_{11}}{\Delta}, & N_2(2,5) &= im\tfrac{f_2 P_6}{\Delta r_k}, \\ N_2(1,3) &= im\tfrac{f_2 P_1}{\Delta r_{k+1}}, & N_2(2,6) &= \tfrac{f_2 \Delta_{23}}{\Delta}, \\ N_2(1,4) &= \tfrac{f_2 \Delta_{13}}{\Delta}, & N_2(3,1) &= \tfrac{f_2 P_7}{\Delta r_k}, \\ N_2(1,5) &= im\tfrac{f_2 P_3}{\Delta r_k}, & N_2(3,2) &= \tfrac{f_2 \Delta_{12}}{\Delta}, \\ N_2(1,6) &= \tfrac{f_2 \Delta_{12}}{\Delta}, & N_2(3,3) &= im\tfrac{f_2 P_7}{\Delta r_k}, \\ N_2(2,1) &= \tfrac{f_2 P_4}{\Delta r_k} - im\tfrac{f_2}{r_k}, & N_2(3,4) &= \tfrac{f_2 \Delta_{23}}{\Delta}, \\ N_2(2,2) &= \tfrac{f_2 \Delta_{13}}{\Delta}, & N_2(3,5) &= f_1 + im\tfrac{f_2 P_9}{\Delta r_k}, \\ N_2(2,3) &= f_1 + \tfrac{f_2}{r_k} + im\tfrac{f_2 P_4}{\Delta r_k}, & N_2(3,6) &= \tfrac{f_2 \Delta_{22}}{\Delta}. \end{aligned} \tag{C.2}$$

The parameters P_l are given by:

For $l = 1, 2, 3;\ j = l + 1$:

$$P_l = -\begin{vmatrix} C_{1j} & C_{15} & C_{16} \\ C_{5j} & C_{55} & C_{56} \\ C_{6j} & C_{65} & C_{66} \end{vmatrix},$$

For $l = 4, 5, 6;\ j = l - 2$:

$$P_l = \begin{vmatrix} C_{11} & C_{1j} & C_{15} \\ C_{51} & C_{5j} & C_{55} \\ C_{61} & C_{6j} & C_{65} \end{vmatrix},$$

For $l = 7, ..., 10;\ j = l - 5$:

(C.3)

$$P_l = -\begin{vmatrix} C_{11} & C_{1j} & C_{16} \\ C_{51} & C_{5j} & C_{56} \\ C_{61} & C_{6j} & C_{66} \end{vmatrix},$$

$$\Delta = P_{10}. \tag{C.4}$$

Δ_{pq} is the cofactor of element C_{pq} of matrix Δ. Functions f_n $(n = 1, 2, 3, 4)$ are cubic polynomials given by:

$$\begin{aligned} f_1 &= \tfrac{1}{4}(2 - 3\eta + \eta^3), & f_2 &= \tfrac{1}{4}(2 + 3\eta - \eta^3), \\ f_3 &= \tfrac{h_k}{8}(1 - \eta - \eta^2 + \eta^3), & f_4 &= \tfrac{h_k}{8}(-1 - \eta + \eta^2 + \eta^3), \end{aligned} \tag{C.5}$$

where

$$\begin{aligned} \eta &= \frac{1}{h_k}\big(2r - r_{k+1} - r_k\big), \\ h_k &= r_{k+1} - r_k. \end{aligned}$$

The matrices $[C_1]$, $[C_2]$, $[M_1]$, $[K_4]$, $[K_5]$, and $[E_1]$ through $[E_3]$ in equation (2.35) are given by:

$$\begin{aligned} [C_1] &= \int_0^H \rho\,[N_1]^{\mathrm{T}}\,[N_1]\,r\,dr, \\ [C_2] &= \int_0^H \rho\Big[[N_1]^{\mathrm{T}}\,[N_2] - [\bar{N}_2]^{\mathrm{T}}\,[N_1]\Big]r\,dr, \end{aligned}$$

$$
\begin{aligned}
[M_1] &= \int_0^H \rho[\bar{N}_2]^{\mathrm{T}}[N_2]\,r dr, \\
[K_4] &= \int_0^H [\,d\,]^{\mathrm{T}}[\,C\,][\,d\,]\,r dr, \\
[K_5] &= \int_0^H [\,d\,]^{\mathrm{T}}[\,C\,][\,b\,]\,r dr, \\
[E_1] &= \int_0^H \Big[[\,d\,]^{\mathrm{T}}[\,C\,][\,a\,] - [\,\bar{b}\,]^{\mathrm{T}}[\,C\,][\,b\,] + [\,\bar{a}\,]^{\mathrm{T}}[\,C\,][\,d\,]\Big] r dr, \\
[E_2] &= \int_0^H \Big[[\,\bar{a}\,]^{\mathrm{T}}[\,C\,][\,b\,] - [\,\bar{b}\,]^{\mathrm{T}}[\,C\,][\,a\,]\Big] r dr, \\
[E_3] &= \int_0^H [\,\bar{a}\,]^{\mathrm{T}}[\,C\,][\,a\,]\,r dr,
\end{aligned}
\tag{C.6}
$$

The non-zero elements of 6×12 matrix $[\,a\,]$ in equation (C.6) are as follows:

$$
\begin{aligned}
a(1,1) &= f_{1,r} + \tfrac{f_{2,r}P_1}{\Delta r_k}, & a(4,1) &= im\tfrac{f_2P_7}{\Delta r_k r}, \\
a(1,2) &= \tfrac{f_{2,r}\Delta_{11}}{\Delta}, & a(4,2) &= im\tfrac{f_2\Delta_{12}}{\Delta r}, \\
a(1,3) &= im\tfrac{f_{2,r}P_1}{\Delta r_k}, & a(4,3) &= -\tfrac{m^2 f_2 P_7}{\Delta r_k r}, \\
a(1,4) &= \tfrac{f_{2,r}\Delta_{13}}{\Delta}, & a(4,4) &= im\tfrac{f_2\Delta_{23}}{\Delta r}, \\
a(1,5) &= im\tfrac{f_{2,r}P_3}{\Delta r_k}, & a(4,5) &= -\tfrac{m^2 f_2 P_9}{\Delta r_k r} + im\tfrac{f_1}{r}, \\
a(1,6) &= \tfrac{f_{2,r}\Delta_{12}}{\Delta}, & a(4,6) &= im\tfrac{f_2\Delta_{22}}{\Delta r}, \\
a(2,1) &= \tfrac{f_1}{r} + \tfrac{m^2 f_2}{r_k r} + \tfrac{f_2P_1}{\Delta r_k r} & a(5,1) &= \tfrac{f_{2,r}P_7}{\Delta r_k}, \\
&\quad + im\tfrac{f_2P_4}{\Delta r_k r}, & a(5,2) &= \tfrac{f_{2,r}\Delta_{12}}{\Delta}, \\
a(2,2) &= \tfrac{f_2\Delta_{11}}{\Delta r} + im\tfrac{f_2\Delta_{13}}{\Delta r}, & a(5,3) &= im\tfrac{f_{2,r}P_7}{\Delta r_k}, \\
a(2,3) &= -\tfrac{m^2 f_2 P_4}{\Delta r_k r} + \tfrac{im}{r}(f_1 + \tfrac{f_2}{r_k} & a(5,4) &= \tfrac{f_{2,r}\Delta_{23}}{\Delta}, \\
&\quad + \tfrac{f_2P_1}{\Delta r_k}), & a(5,5) &= f_{1,r} + im\tfrac{f_{2,r}P_9}{\Delta r_k}, \\
a(2,4) &= \tfrac{f_2\Delta_{13}}{\Delta r} + im\tfrac{f_2\Delta_{33}}{\Delta r}, & a(5,6) &= \tfrac{f_{2,r}\Delta_{22}}{\Delta}, \\
a(2,5) &= -\tfrac{m^2 f_2 P_6}{\Delta r_k r} + im\tfrac{f_2P_3}{\Delta r_k r}, & a(6,1) &= \tfrac{P_4}{\Delta r_k}(f_{2,r} - \tfrac{f_2}{r}) + im(\tfrac{f_1}{r} + \tfrac{f_2P_1}{\Delta r_k r} \\
a(2,6) &= \tfrac{f_2\Delta_{12}}{\Delta r} + im\tfrac{f_2\Delta_{23}}{\Delta r}, & &\quad + \tfrac{f_2}{r_k r} - \tfrac{f_{2,r}}{r_k}),
\end{aligned}
\tag{C.7}
$$

$$
\begin{aligned}
a(6,2) &= \tfrac{\Delta_{13}}{\Delta}(f_{2,r} - \tfrac{f_2}{r}) + im\tfrac{f_2\Delta_{11}}{\Delta r}, & a(6,4) &= \tfrac{\Delta_{33}}{\Delta}(f_{2,r} - \tfrac{f_2}{r}) + im\tfrac{f_2\Delta_{13}}{\Delta r}, \\
a(6,3) &= f_{1,r} + \tfrac{f_{2,r}}{r_k} - \tfrac{f_1}{r} - \tfrac{f_2}{r_k r} & a(6,5) &= -\tfrac{m^2 f_2 P_3}{\Delta r_k r} + im\tfrac{P_6}{\Delta r_k}(f_{2,r} - \tfrac{f_2}{r}), \\
&\quad - \tfrac{m^2 f_2 P_1}{\Delta r_k r} + im\tfrac{P_4}{\Delta r_k r}(f_{2,r} - \tfrac{f_2}{r}), & a(6,6) &= \tfrac{\Delta_{23}}{\Delta}(f_{2,r} - \tfrac{f_2}{r}) + im\tfrac{f_2\Delta_{12}}{\Delta r},
\end{aligned}
\tag{C.8}
$$

where the $f_{n,r}$ represents $\frac{\partial f_n}{\partial r}$.

The non-zero elements of 6×12 matrix [b] in equation (C.6) are as follows:

$$
\begin{aligned}
b(1,3) &= \tfrac{f_{2,r}P_3}{\Delta}, & b(4,3) &= f_1 + \tfrac{f_2}{r_k} + im\tfrac{f_2}{\Delta}(\tfrac{P_4}{r_k} + \tfrac{P_9}{r}),\\
b(1,5) &= \tfrac{f_{2,r}P_2}{\Delta}, & b(4,4) &= \tfrac{f_2\Delta_{33}}{\Delta},\\
b(2,3) &= \tfrac{f_2P_3}{\Delta r} + im\tfrac{f_2P_6}{\Delta r}, & b(4,5) &= im\tfrac{f_2}{\Delta}(\tfrac{P_6}{r_k} + \tfrac{P_8}{r}),\\
b(2,5) &= \tfrac{f_2P_2}{\Delta r} + im\tfrac{f_2P_5}{\Delta r}, & b(4,6) &= \tfrac{f_2\Delta_{23}}{\Delta},\\
b(3,1) &= \tfrac{f_2P_7}{\Delta r_k}, & b(5,1) &= f_1 + f_{2,r} + \tfrac{f_2P_1}{\Delta r_k},\\
b(3,2) &= \tfrac{f_2\Delta_{12}}{\Delta}, & b(5,2) &= \tfrac{f_2\Delta_{11}}{\Delta},\\
b(3,3) &= im\tfrac{f_2P_7}{\Delta r_k}, & b(5,3) &= \tfrac{f_{2,r}P_9}{\Delta} + im\tfrac{f_2P_1}{\Delta r_k},\\
b(3,4) &= \tfrac{f_2\Delta_{23}}{\Delta}, & b(5,4) &= \tfrac{f_2\Delta_{13}}{\Delta},\\
b(3,5) &= f_1 + im\tfrac{f_2P_9}{\Delta r_k}, & b(5,5) &= \tfrac{f_{2,r}P_8}{\Delta} + im\tfrac{f_2P_3}{\Delta r_k},\\
b(3,6) &= \tfrac{f_2\Delta_{22}}{\Delta}, & b(5,6) &= \tfrac{f_2\Delta_{12}}{\Delta},\\
b(4,1) &= \tfrac{f_2P_4}{\Delta r_k} - imf_2(\tfrac{1}{r_k} + \tfrac{1}{r}), & b(6,3) &= \tfrac{P_6}{\Delta}(f_{2,r} - \tfrac{f_2}{r}) + im\tfrac{f_2P_3}{\Delta r},\\
b(4,2) &= \tfrac{f_2\Delta_{13}}{\Delta}, & b(6,5) &= \tfrac{P_5}{\Delta}(f_{2,r} - \tfrac{f_2}{r}) + im\tfrac{f_2P_2}{\Delta r}.
\end{aligned}
\tag{C.9}
$$

The 6×12 matrix [d] in equation (C.6) has non-zero elements as follows:

$$
\begin{aligned}
d(3,1) &= -f_2, & d(4,3) &= \tfrac{f_2P_6}{\Delta},\\
d(3,3) &= \tfrac{f_2P_9}{\Delta}, & d(4,5) &= \tfrac{f_2P_5}{\Delta},\\
d(3,5) &= \tfrac{f_2P_8}{\Delta}, & d(5,3) &= \tfrac{f_2P_3}{\Delta},\\
& & d(5,5) &= \tfrac{f_2P_2}{\Delta},
\end{aligned}
\tag{C.10}
$$

where the remaining 6 columns of matrices $[N_1]$, $[N_2]$, [a], [b], and [d] can be obtained from the first 6 columns by replacing f_1 by f_3, f_2 by f_4, and r_k by r_{k+1}.

Appendix D

Asymptotic Expansions of Hankel Functions

The functions $E(m,\zeta r)$ and $F(m,\zeta r)$ in the asymptotic expansion forms of the Hankel functions $H_m^{(1)}(\zeta r)$ and $H_m^{(2)}(\zeta r)$ for the large argument in equation(2.41) are defined as:

$$\begin{aligned} E(m,\zeta r) &\sim \sum_{n=0}^{\infty} \frac{(m,2n)}{(2\zeta r)^{2n}}, \\ &= 1 - \frac{(\wp-1)(\wp-9)}{2!(8\zeta r)^2} + \frac{(\wp-1)(\wp-9)(\wp-25)(\wp-49)}{4!(8\zeta r)^4} - \dots \quad , \text{(D.1)} \\ F(m,\zeta r) &\sim \sum_{n=0}^{\infty} (-1)^n \frac{(m,2n+1)}{(2\zeta r)^{2n+1}}, \\ &= \frac{(\wp-1)}{(8\zeta r)^1} - \frac{(\wp-1)(\wp-9)(\wp-25)}{3!(8\zeta r)^3} + \dots \quad , \end{aligned}$$

where $\wp = 4m^2$.

Appendix E

Polynomial Interpolations for Stress Components

The elements of 3×9 matrix $[N_3]$ in equation (3.8) are defined as:

$$\begin{aligned}
N_3(1,i) &= C_{15}n_j' + (\tfrac{C_{25}}{r} - i\xi C_{55} + \tfrac{im}{r}C_{56})n_j, \\
N_3(1,i+1) &= (\tfrac{im}{r}C_{25} - i\xi C_{45} - \tfrac{C_{56}}{r})n_j + C_{56}n_j', \\
N_3(1,i+2) &= (-i\xi C_{35} + \tfrac{im}{r}C_{45})n_j + C_{55}n_j', \\
N_3(2,i) &= C_{14}n_j' + (\tfrac{C_{24}}{r} - i\xi C_{45} + \tfrac{im}{r}C_{46})n_j, \\
N_3(2,i+1) &= (\tfrac{im}{r}C_{24} - i\xi C_{44} - \tfrac{C_{46}}{r})n_j + C_{46}n_j', \\
N_3(2,i+2) &= (-i\xi C_{34} + \tfrac{im}{r}C_{44})n_j + C_{45}n_j', \\
N_3(3,i) &= C_{13}n_j' + (\tfrac{C_{23}}{r} - i\xi C_{35} + \tfrac{im}{r}C_{36})n_j, \\
N_3(3,i+1) &= (\tfrac{im}{r}C_{23} - i\xi C_{34} - \tfrac{C_{36}}{r})n_j + C_{36}n_j', \\
N_3(3,i+2) &= (-i\xi C_{33} + \tfrac{im}{r}C_{34})n_j + C_{35}n_j',
\end{aligned} \tag{E.1}$$

where $i = 1, 4, 7$ and $j = 1, 2, 3$, respectively. Prime denotes the differentiation with respect to r.